Normal fault growth and fault zone architecture of normal faults exposed in the Corinth Canal, central Greece

Stine Hemnes Sletten

Master thesis in

Petroleum Geoscience

Department of Earth Science

University of Bergen

August 2016

Abstract

The Corinth Canal in central Greece consists of an excellent natural transect across a population of normal faults. This study presents a structural analysis of 23 exposed faults, focusing on fault geometry, fault zone architecture and the structural evolution of the Corinth Canal. The canal is located on the Corinth Isthmus in the eastern part of the Corinth Rift, which is one of the most active continental rifts on Earth. Main structural elements exposed within the canal section are a central horst block, several fault blocks and the Isthmia Graben. The study integrates traditional field data with LiDAR-based digital outcrop data. The quantitative fault analyses conducted include fault orientations, throw-depth plots, expansion indices and cumulative plots of fault frequency, throw and heave. A detailed stratigraphic framework is provided in order to determine the relative timing and growth history of the studied faults. The stratigraphy of the Corinth Canal is divided into six tectonostratigraphic units based on the identification of major erosional surfaces, major shifts in facies and thickness trends that can be related to tectonic events. Tectonostratigraphic Units 1, 2 and 3 are composed of lacustrine deposits, whereas Tectonostratigraphic Units 4, 5 and 6 are composed of marine deposits. The faults exhibit planar, listric or vertically and laterally segmented geometries. The vertically segmented geometries include contractional overlaps, contractional and extensional bends, hard linked structures and lenses. Damage zones are commonly narrow and contain splay faults and smaller scale faults. The distribution of faults, throw and heave within the Corinth Canal is moderately heterogeneous with localization of strain onto several larger faults and in the half graben SE of the central horst. Most of the strain is accommodated by the horst-bounding faults. The exposed faults are interpreted to represent the up-dip tip of deep-seated faults that have nucleated at depth. Their growth history is characterized by blind fault propagation before breaching the surface and becoming syn-sedimentary growth faults. Burial and inactivity also characterize the history of several faults; some of which show signs of polycyclic growth. An age model for the key stratal surfaces that bound the marine tectonostratigraphic units is proposed based on previously dated *Acropora* corals within the canal section and the chronostratigraphy of the Corinth Gulf. This allowed to constrain the activity of the N- and S-dipping faults between 620 ka to 340 ka, which is consistent with observations from the offshore Corinth Gulf; thereby linking the structural evolution of the Corinth Canal with the regional evolution of the Corinth Rift.

II

Acknowledgments

This thesis is a part of a master's degree in Petroleum Geoscience at the Department of Earth Science at the University of Bergen, and I owe gratitude to this institution for funding my fieldwork.

First and foremost, I want to express my sincere gratitude to my supervisor Rob Gawthorpe, my co-supervisor Martin Muravchik and Casey Nixon for their guidance, motivation and inspirational discussions related to this thesis. A special thanks to Martin for taking the time to meet on a weekly basis and for acquiring and processing the LiDAR data utilized in this study. Additionally, I would like to thank Rob Gawthorpe, Martin Muravchik, Casey Nixon, Gijs Allard Henstra and fellow students Marte, Kari and Ine for proofreading and commenting on different sections in this thesis.

I would also like to thank Rob Gawthorpe, Martin Muravchik, Gijs Allard Henstra, Haralambos Kranis, Manolis Skourtsos, Sturla Vatne Meling, Marthe Førland and Olav Aleksander Naurstad for their contribution during fieldwork in Greece. Thank you for sharing your observations, ideas and knowledge in the field and for great conversations and laughs at "five brothers" in the evenings. Sturla is also thanked for great collaboration in the field and while working with the LiDAR data back at the university. Furthermore, I would like to express my gratitude to the canal company, A. E. ΔI. K., for allowing me to wander along the Corinth Canal and for providing a free boat trip through the spectacular canal. I am also thankful to the Segas family at Hotel Segas in Greece for their hospitality, kindness and great service during both my stays.

I thank my fellow geology students at the University of Bergen for five unforgettable years. A special thanks to the wonderful people at "Midtrommet" and at the seismic lab!

Last but not least, I am very grateful to my mother, Gail, and my boyfriend, Daniel, for their everlasting love, support, encouragement and help.

Stine Hemnes Sletten   Bergen, 21th of August 2016

Table of Contents

1 Introduction

1.1 Background and rationale

2.1.1 Study area

The Corinth Canal is located on the Corinth Isthmus at the eastern end of the Corinth Gulf in central Greece (Fig. 1.1). The Isthmus represents an intrabasinal high that separates the Lechaion Gulf, a southern sub-basin in the eastern part of the Gulf of Corinth (e.g. Turner et al., 2010) and the Saronic Gulf. The length of the canal is 6.4 km, with widths ranging between 21.3 m at sea level and a maximum of approximately 100 m at the top (A. E. ΔI. K., 2009). The excavation of the canal resulted in two adjacent outcrops, with a maximum height of about 80 m, excellently exposing coastal facies and structural intrabasinal features (Collier, 1990). The Corinth Canal therefore represents a unique location for studying the structural and sedimentary evolution of rift intrabasinal highs. This MSc thesis focuses on the analysis of the extensional structures exposed in the canal section.

The Corinth Rift is one of the most active continental rifts on Earth and a large amount of studies have been conducted in this area both onshore (e.g. Ori, 1989, Collier & Dart, 1991, Rohais et al., 2007, Ford et al., 2013) and offshore (e.g. Bell et al., 2008, Bell et al., 2009, Taylor et al., 2011, Charalampakis et al., 2014, Nixon et al., 2016). However, most studies are related to the central and western parts and relatively little is known of the Corinth Canal sector to the east. The structural evolution of the canal has not been studied previously. Thus, this study will provide new knowledge to the structural evolution the Corinth Canal sector. The overall structural style of the canal includes a central horst block, faults that form fault blocks NW and SE of the central horst and a graben, the Isthmia Graben, towards the southeastern end of the canal (Collier, 1990). The faults strike at an average of 077° and dip in contrasting directions at either side of the central horst. The fault blocks to the NW of the central horst are mainly bound by N-dipping faults, while to the SE of the central horst the faults dip predominantly towards the S. Due to the NW-SE orientation of the Corinth Canal the faults are obliquely exposed along its margins.
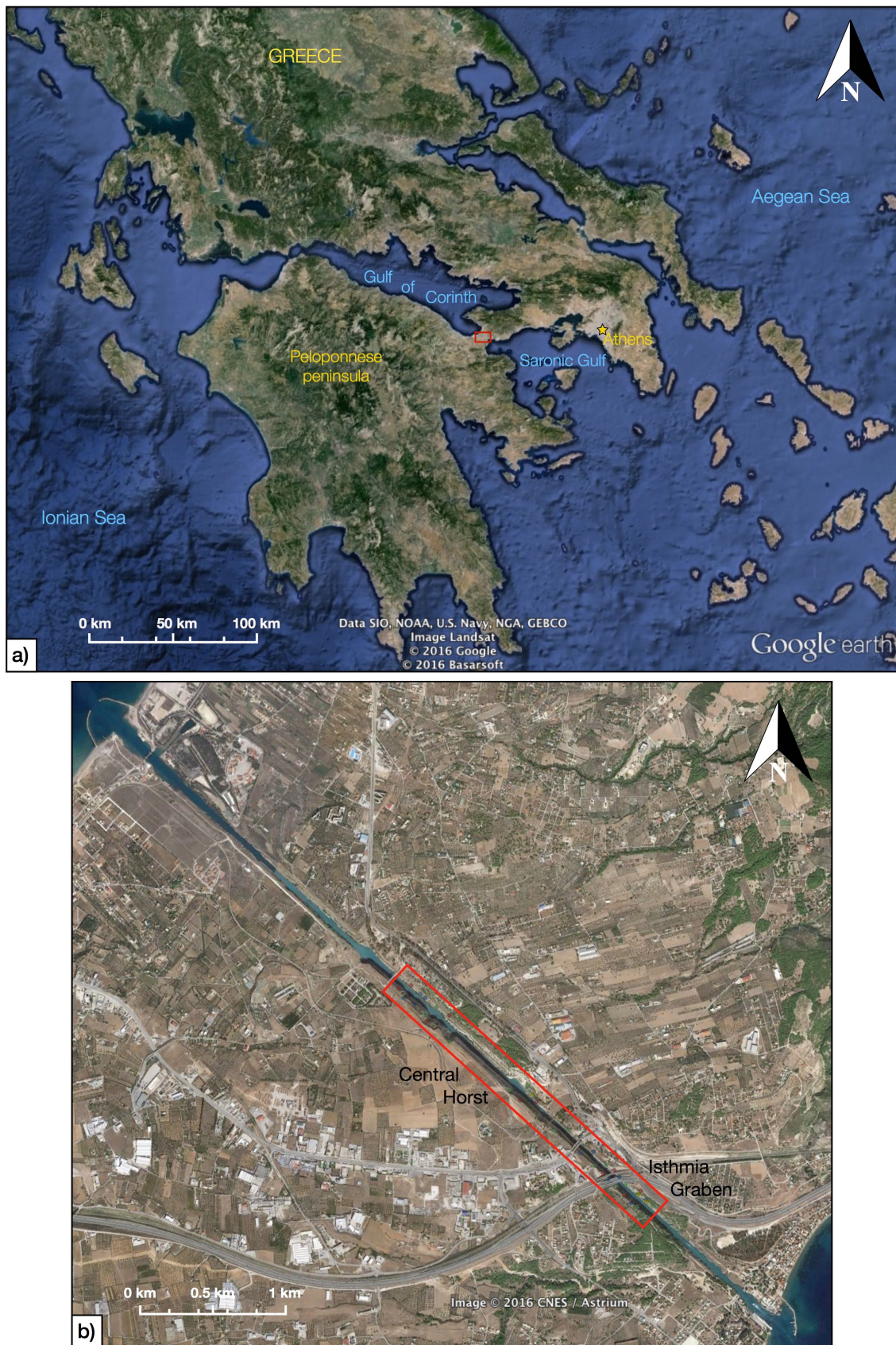
Figure 1.1 – Location of the Corinth Canal in central Greece (a) and a close-up of the canal indicating the central horst block and the Isthmia Graben (b). The red boxes indicate the canal (a) and the study area within the canal (b). Modified from Google Earth.

1.1.2 Previous studies and knowledge gaps

Faults usually have a segmented nature, both in map view and in cross section (e.g. Larsen, 1988, Peacock & Sanderson, 1991, 1994, Childs et al., 1996, Walsh et al., 2003). This indicates that faults also are segmented in 3D, which has been demonstrated from seismic studies (e.g. Childs et al., 1995, Mansfield & Cartwright, 1996). The fault segments can nucleate and grow as kinematically independent elements (e.g. Walsh & Watterson, 1988, Trudgill & Cartwright, 1994, Cartwright et al., 1995, Dawers & Anders, 1995) or as kinematically related elements in a fault array (e.g. Childs et al., 1995, Walsh et al., 2002, Walsh et al., 2003). The interaction and linkage between fault segments develop fault zone geometries and architecture, which can range between simple or highly complex.

Fault zone architecture includes a fault core, a damage zone and a protolith (Caine et al., 1996). The damage zone bound the fault core and consists of subsidiary structures, which can be located both in the hanging wall and the footwall. In the Corinth Canal such structures are primarily minor faults or splay faults. Studies of splay faults are mostly conducted on strike-slip faults in map view (e.g. Granier, 1985, Kim et al., 2003, Kim et al., 2004), and usually focus on fault tip splays (Granier, 1985, McGrath & Davison, 1995, Perrin et al., 2015). Hence, the exposures in the canal section provide an opportunity to study splay faults occurring at different locations around normal faults in a vertical section, and how these structures link to the main fault planes.

Studies of fault geometries and fault zone architecture are important due to the major control that faults have on fluid flow in the upper crustal regime, where they might act as barriers, conduits or combined conduit-barriers (Caine et al., 1996). Since the geometry and the fault zone architecture usually is below the resolution of seismic imaging, outcrop analogues are very important for understanding subsurface reservoirs (e.g. Ferrill & Morris, 2008, Rotevatn et al., 2009).

1.2 Aim and objectives

The aim of this MSc study is to conduct a structural analysis focusing on fault geometry, fault zone architecture and the structural evolution of the normal fault population exposed within the Corinth Canal in central Greece. This will be achieved by integrating LiDAR-based digital outcrop data and traditional field data collected during two field seasons in 2015. The specific objectives of this study are:

i.   Describe the geometry (and associated deformation) of the normal faults, and their segmentation.
ii. Characterize the footwall and hanging wall damage zones.
iii. Determine the relative timing of fault activity and fault evolution with the aid from T-z plots and expansion indices.
iv. Analyze the distribution of deformation within the fault population from cumulative plots of fault frequency, throw and heave.

1.3 Thesis outline

After this brief introduction (chapter 1), chapter 2 presents an overview of terminology and theory utilized in this study. The focus of this chapter is propagation, interaction and linkage of normal faults, fault zone architecture and splay faults. Chapter 3 provides the geological background of the Corinth Rift and the Corinth Canal sector, with focus on the tectonic and stratigraphic framework. In chapter 4 an overview of the database and methods applied in the field and while interpreting the digital outcrop data is presented. Additionally, the different quantitative fault analyses conducted in this study are introduced. Chapter 5 presents the stratigraphy of the Corinth Canal with focus on stratal surfaces and tectonostratigraphic units. In chapter 6 the range of fault geometries exposed within the canal section is described together with characteristics of their corresponding fault zones. Further, the chapter provides description and interpretation of T-z plots and expansion indices before rounding off with the distribution of faults, throw and heave within the fault population. Chapter 7 discusses the results with respect to growth of individual faults, growth of the entire fault population and deformation around horst blocks. Lastly, the conclusions and suggestions for further work are provided in chapter 8.

2 Theoretical background

The aim of this chapter is to provide an overview of the terminology and theory utilized in this study. Section 2.1 focuses on theories related to propagation, interaction and linkage of normal faults, both in map view and cross section. A general overview of fault zone architecture is presented in section 2.2, while section 2.3 focuses on splay faults.

2.1 Propagation, interaction and linkage of normal faults

2.1.1 Single fault

In isolated normal fault models faults are represented by simple planes that have an elliptical shape (Barnett et al., 1987, Walsh & Watterson, 1987). The outer boundary of the ellipse is termed the tip-line, where displacement is zero. The shortest axis of the ellipse is parallel to the displacement direction and displacement contours can be drawn around the point of maximum displacement, which is located in the center.

A power function can describe the growth path of a single fault by radial propagation (Fig. 2.1) (Cartwright et al., 1995). This law describes the relationship between displacement (D) and length (L) of a fault, and can be expressed as $D = cL^n$, where the factor c is a constant related to rock material properties (Cartwright et al., 1995 and references therein). Different values ranging from 1 (Cowie & Scholz, 1992) to 2 (Watterson, 1986, Walsh & Watterson, 1988) have been calculated for the exponent n. Later studies modified this function into the linear expression $D = c*L$, where $c*$ represents critical shear strain (Cowie & Scholz, 1992, Dawers et al., 1993, Scholz et al., 1993).
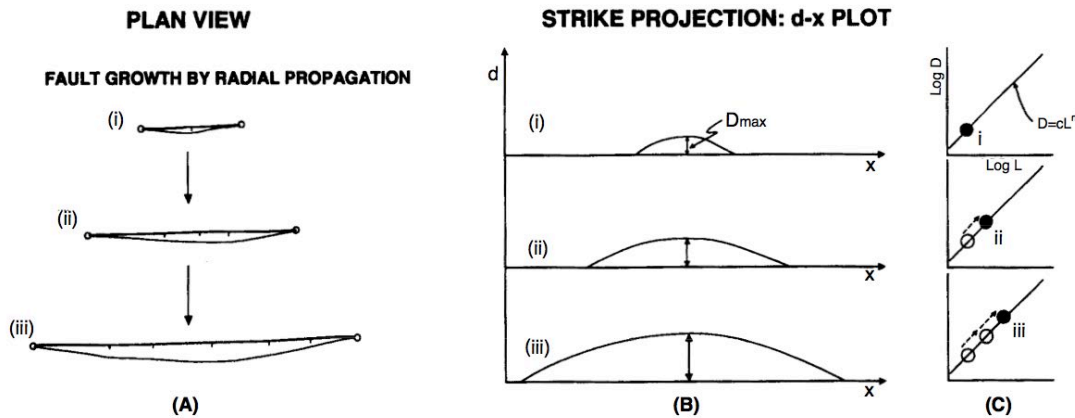
Figure 2.1 – Schematic illustrations of fault growth by radial propagation in three growth stages. (A) Plan view. (B) Plot of fault displacement (d) versus distance along strike (x). (C) Plot showing log maximum displacement (D) against log length (L). Redrawn from Cartwright et al. (1995).

2.1.2 Fault interaction

Two types of fault interaction occur: soft linkage and hard linkage (e.g. Walsh & Watterson, 1991). Soft linkage takes place when overlapping faults interact through ductile strain of the rock volume, while hard linkage occurs when fault segments become physically linked together to form a through-going fault. As a result of soft linkage a relay ramp may form (Fig. 2.2). A relay ramp is defined as a transfer zone between normal fault segments that dip in the same direction (Larsen, 1988, Peacock & Sanderson, 1991, 1994). Other common features of relay ramps are fractures or minor faults that transfer displacement between the fault segments. Eventually the relay ramp will breach and become hard linked, which results in an along-strike bend (Peacock & Sanderson, 1994).
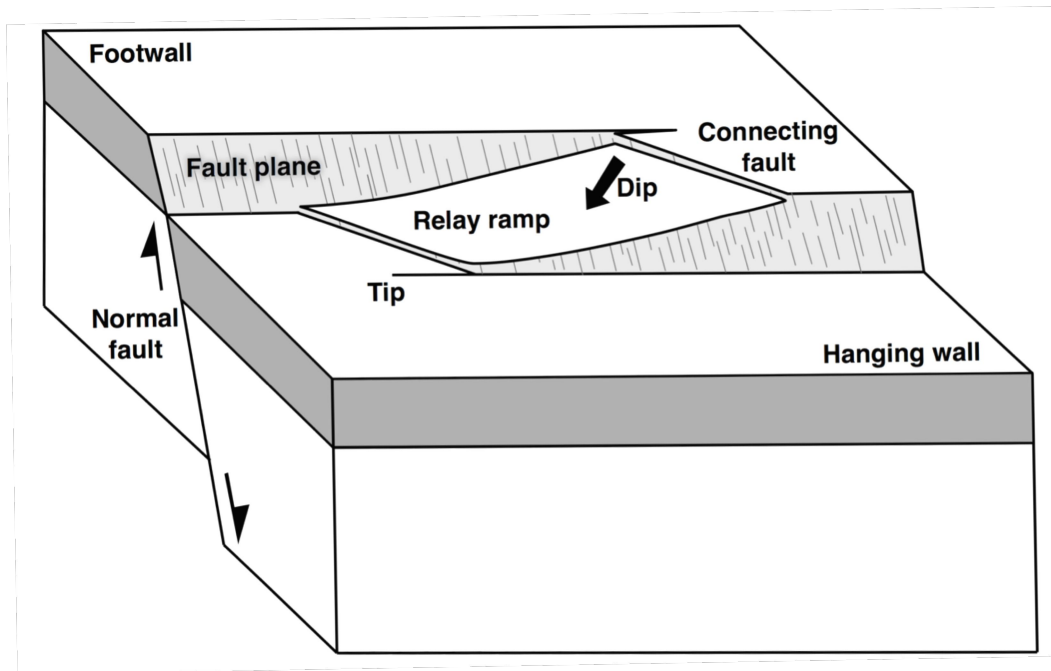
Figure 2.2 – Block diagram of relay ramp main features. Redrawn from Peacock and Sanderson (1994).

There are two end-member models for growth and linkage of normal faults (Fig. 2.3). Walsh et al. (2003) referred to these models as the 'isolated fault model' (e.g. Walsh & Watterson, 1988, Trudgill & Cartwright, 1994, Cartwright et al., 1995, Dawers & Anders, 1995, Cowie, 1998, Cowie et al., 2000) and the 'coherent fault model' (e.g. Childs et al., 1995, Walsh et al., 2002, Giba et al., 2012). In the isolated fault model fault segments are kinematically unrelated to the fault array during nucleation and propagation (e.g. Trudgill & Cartwright, 1994). The fault segments grow as a result of gradual increase in both maximum displacement and length and their growth history is characterized by radial propagation of tip-lines, interaction and linkage. Relay zones form as incidental overlap and interaction by soft linkage between fault segments occur. Continued growth cause breaching of the relay structure and the fault segments become hard linked.

The coherent fault model is characterized by individual fault segments, which are kinematically related to the fault array at their initiation and during growth (e.g. Walsh et al., 2003). This model suggests that fault lengths are established at an early stage, and that growth is mainly a result of increase in displacement and not radial tip-line propagation. In contrast to the isolated fault model, the formation of relays are not incidental and they are a result of either hard linkage due to fault surface bifurcation (i.e. splaying) or soft linkage formed by 3D segmentation processes.

7

The main difference between the two end-member models is the status of the individual fault segments during their nucleation, i.e. if the fault segments are kinematically independent or kinematically related components of a fault array during nucleation (Walsh et al., 2003). As a result of this difference the displacement distribution will be different in each model (Fig. 2.3). In the coherent model the displacement distribution of the multiple fault segments in a fault array will show a regular distribution similar to a single isolated fault. In contrast, in the isolated model multiple local maxima related to each fault segment is observed.
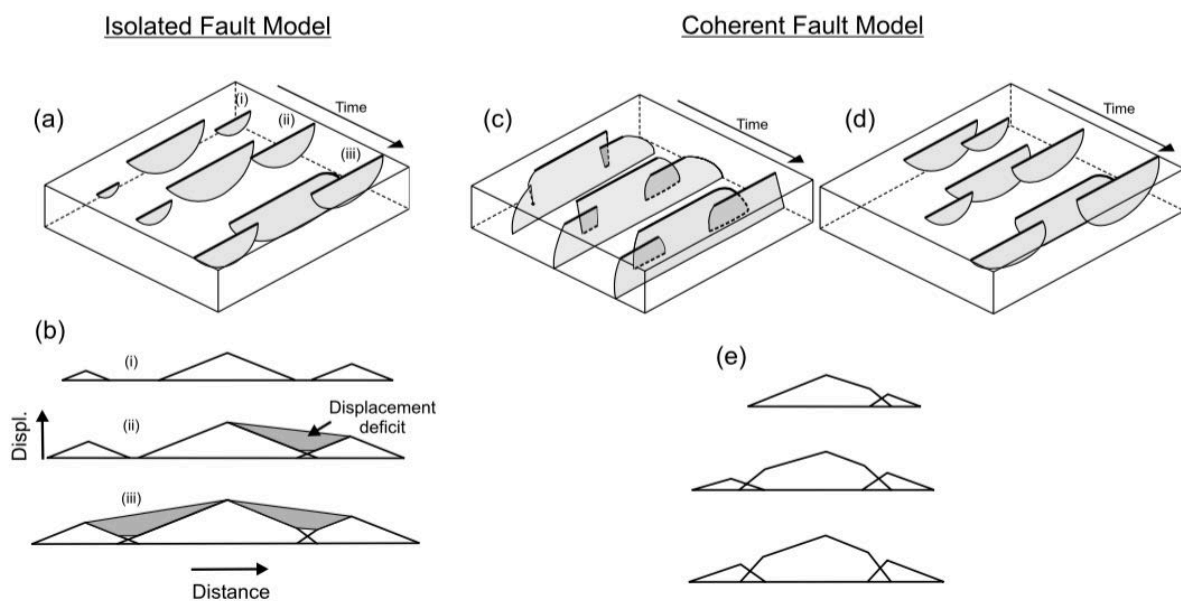
Figure 2.3 – Schematic illustrations of the two end-member models for growth and linkage of normal faults shown as block diagrams (a, c, and d) and displacement-distance plots (b and e) during three growth stages (i – iii). From Walsh et al. (2003).

Studies have shown that normal faults are usually segmented both laterally and vertically (e.g. Childs et al., 1996, Jackson & Rotevatn, 2013, Tvedt et al., 2013). Similar to laterally segmented normal faults, vertically segmented normal faults are also characterized by steps, overlaps and bends (Fig. 2.4) (Childs et al., 1996). In a vertical section these features have two end-members, contractional and extensional, but can also be mixed. The two end-members have many different terms in the literature. Contractional is synonymous of restraining, closing and convergent, whereas extensional is synonymous of releasing, opening and divergent (e.g. Crowell, 1974, Biddle & Christie-Blick, 1985). As shown in fig. 2.4 contractional steps and overlaps occur where the lower fault step/overlap in the hanging wall of the upper fault, while

the opposite is the case for extensional steps and overlaps, where the lower fault step/overlap in the footwall of the upper fault. Contractional bends occur in places where the dip of the fault decreases, whereas extensional bends result from an increase in fault dip.
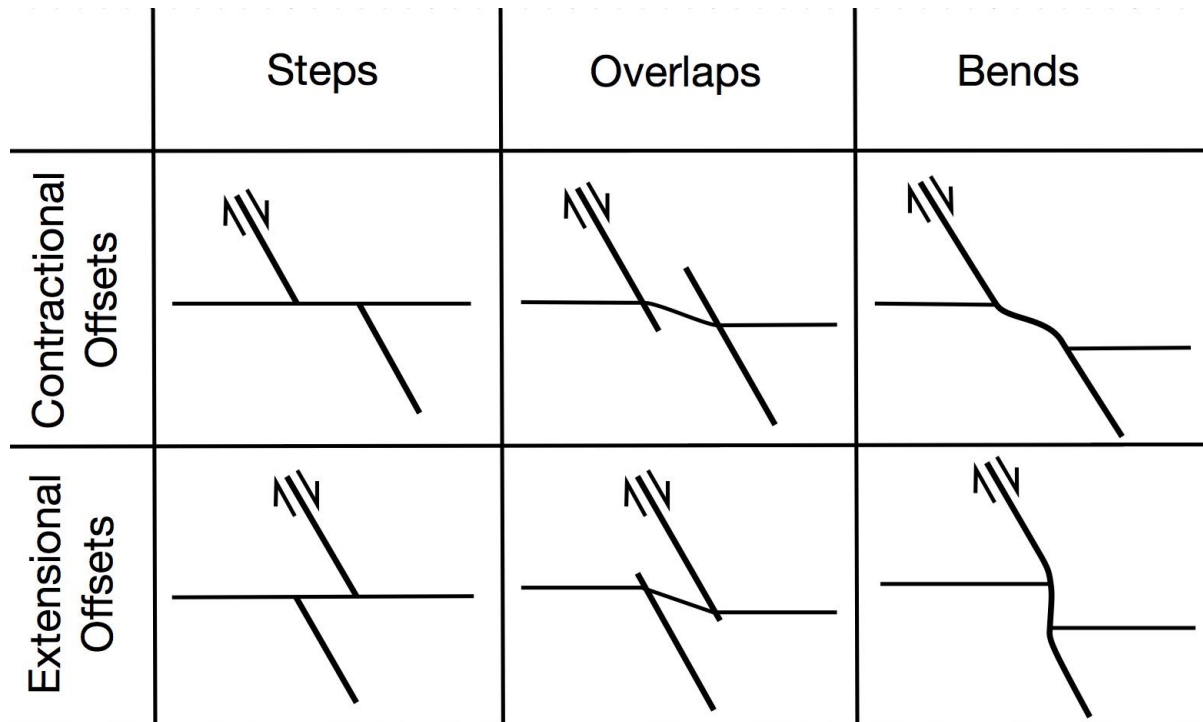
Figure 2.4 – Schematic illustration of contractional and extensional steps, overlaps and bends. Redrawn from Childs et al. (1996).

Steps usually have low displacements, while overlaps and bends are characterized by larger displacements (Peacock & Xing, 1994, Childs et al., 1996). This implies that fault offsets generally nucleate as steps and are replaced by overlaps and bends once they accrue larger displacements. Minor structures comprising minor faults, brecciation, folds, compaction and pressure solution might also occur at overlaps and bends (Peacock & Xing, 1994).

Faults that overlap in 2D (i.e. in map view or cross-section) can be either unconnected or linked by a branch-point or a branch-line in 3D (Childs et al., 1995). Branch-lines are the intersection line between two fault planes (e.g. Peacock et al., 2000), and is interpreted to form as a result of breaching of relay zones (Walsh et al., 1999).

2.2 Fault zone architecture

Brittle fault zones are located in the upper crust and represent discontinuities that are lithologically heterogeneous and structurally anisotropic (e.g. Caine et al., 1996, Faulkner et al., 2010). According to Caine et al. (1996) fault zone architecture comprise a fault core, a damage zone and a protolith. The fault core represents a high–strain zone that takes up most of the displacement of a fault and may include slip surfaces, fault gouge, breccias, cataclasites, lenses of fault rock or protolith, shale smear, fractures and deformation bands (e.g. Chester & Logan, 1987, Caine et al., 1996, Bastesen & Braathen, 2010). Fault cores are usually discontinuous with thickness variations occurring both along the strike and along the dip direction of the fault. The damage zone is defined as the volume of deformed rocks around the fault core (McGrath & Davison, 1995, Caine et al., 1996). Structural elements found in the damage zone might be small faults, fractures, deformation bands, veins, cleavage and folds (e.g. Caine et al., 1996, Bastesen & Braathen, 2010). A geometrical classification of damage zones was suggested by Kim et al. (2004) and include the terms tip damage zone (or process zone, sensu Cowie & Shipton, 1998), wall damage zone and linking damage zone, indicating their location relative to the faults (Fig. 2.5).
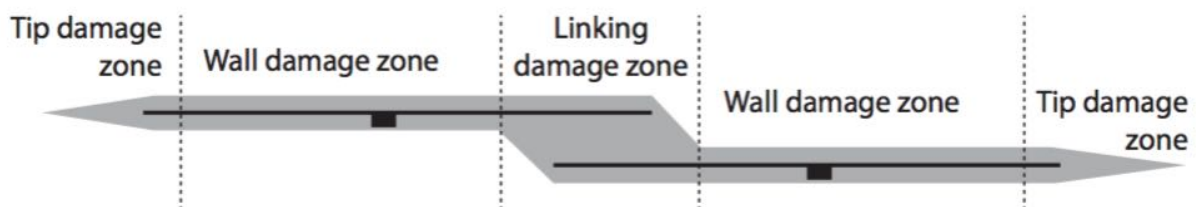
Figure 2.5 – Damage zone terminology suggested by Kim et al. (2004), including terms as tip damage zone, wall damage zone and linking damage zone. From Rotevatn and Bastesen (2014).

Childs et al. (2009) define fault zones differently from Caine et al. (1996) and includes components such as fault rock, relay zones, damage zones and fault zones. The classification by Childs et al. (2009) was proposed due to problems when trying to measure the outcrop thicknesses of fault zones, damage zone and fault rocks. Since this study does not focus on measuring the thicknesses of different architectural elements, the terminology presented by Caine et al. (1996) is utilized to describe the fault zones within the study area.

2.3 Splay faults

Splay faults are subsidiary faults branching off the main fault with acute angles (e.g. Granier, 1985, McGrath & Davison, 1995, Davatzes & Aydin, 2003, Perrin et al., 2015). Due to this general definition splay faults are referred to under various terms in the literature such as horsetails (Granier, 1985, McGrath & Davison, 1995), wing cracks (Willemse & Pollard, 1998), branch faults (Kim et al., 2004), bifurcating faults (Walsh et al., 2003), etc.

Most studies on splay faults are related to strike-slip faults in map view (e.g. Granier, 1985, Kim et al., 2003, Kim et al., 2004) and seem to be focusing on fault tip splays (e.g. Granier, 1985, McGrath & Davison, 1995, Perrin et al., 2015). Fault tip splays form a fan shaped widening adjacent to the tip of propagating faults and indicate the direction of long-term propagation of the main fault (McGrath & Davison, 1995, Perrin et al., 2015). Splay faults can develop in any slip mode (normal, revers and strike-slip). In relation to normal faults, splays are usually found in the hanging wall of the main fault, with a few exceptions found in the footwall or both the hanging wall and the footwall (Perrin et al., 2015). Splay faults are a part of the damage zone of the main fault (McGrath & Davison, 1995, Kim et al., 2004, Perrin et al., 2015). Furthermore, splays located along the fault trace are interpreted to represent paleo-tip lines (McGrath & Davison, 1995).

3 Geological setting

The aim of this chapter is give an overview of the geological setting of the study area. The chapter is divided into three sections and includes a short introduction (section 3.1) and further focusing into the tectonic and stratigraphic framework (sections 3.2 and 3.3). The tectonic framework starts on a large scale with the overall tectonics of the Aegean region before focusing on the Corinth Rift and the Corinth-Nemea basin. The focus of the stratigraphic framework is pre- and syn-rift stratigraphy. A similar approach is followed for the stratigraphic framework, starting with introducing the overall stratigraphy of the Corinth Rift before focusing onto the Corinth-Nemea basin.

3.1 Introduction

The study area is constituted by the exposures at either margin of the Corinth Canal at the Corinth Isthmus, linking the Corinth Gulf and the Saronic Gulf (Fig. 3.1). Both these gulfs integrate the present day Corinth Rift, which is one of the most active continental rifts on Earth (e.g. Bell et al., 2009). Its extension rate ranges from 4 mm/yr in the eastern part to 11-16 mm/yr in the central and western parts (e.g. Clarke et al., 1997, Avallone et al., 2004, Bernard et al., 2006). The Corinth Rift originated in the Pliocene approximately 5 Ma and is characterized by a N-S extension direction (Ori, 1989, Roberts & Jackson, 1991). The Gulf of Corinth is 105 km long, 0.5 km wide at its narrowest point to the west and 30 km wide at its broadest point to the east (Ford et al., 2013). As fault displacement migrated towards the north, the earliest rift fault blocks are found on the northern Peloponnese, while the active faults are located offshore in the Gulf of Corinth (Leeder et al., 2008, Bell et al., 2009). The western Saronic Gulf is active and characterized by normal faults trending WNW-ESE, whereas the eastern part is regarded as relatively inactive (Papanikolaou et al., 1988, Nomikou et al., 2013).
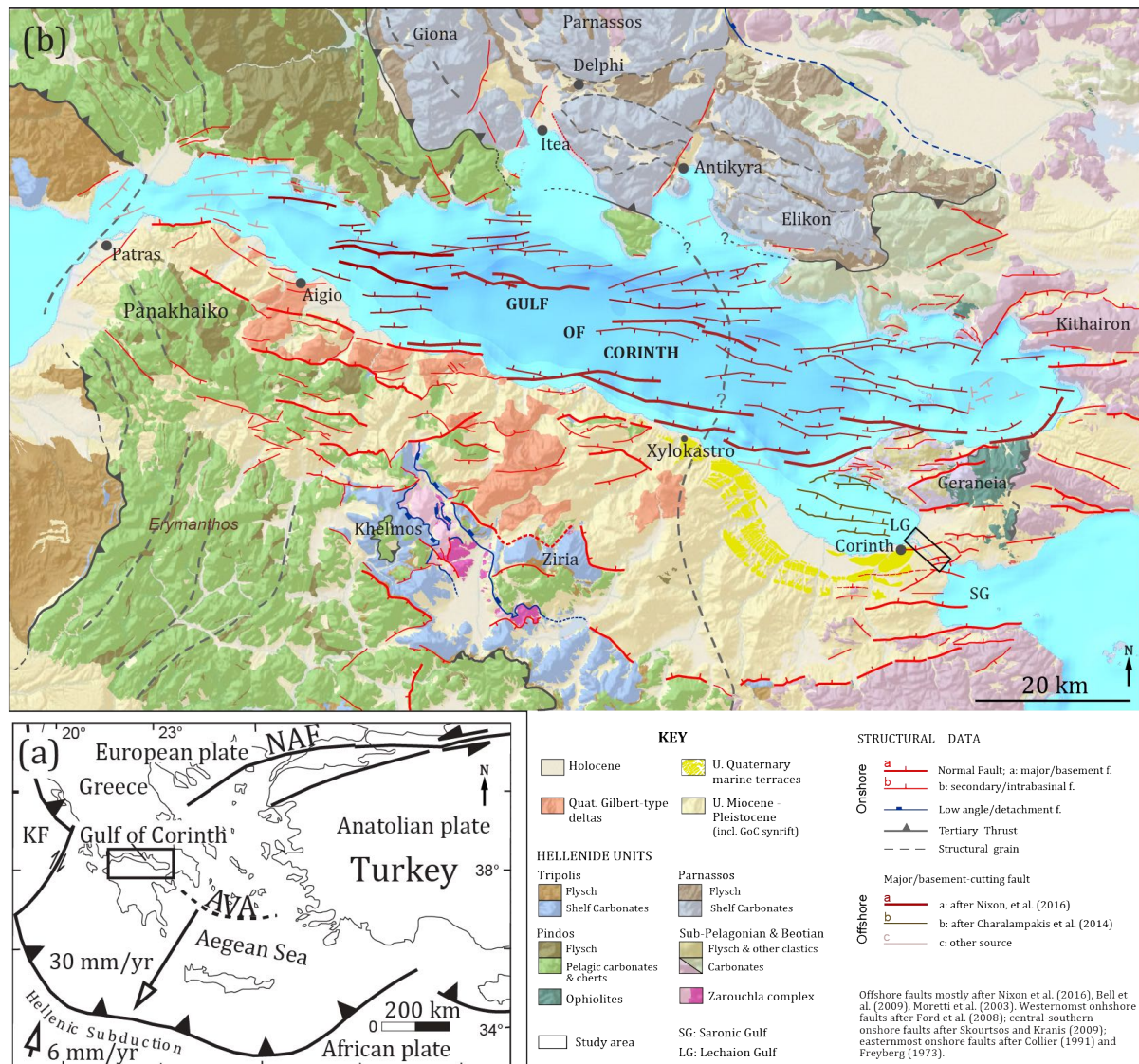
Figure 3.1 – (a) Tectonic map of the Aegean region. (b) Geological map of the Corinth Rift showing onshore deposits, Mesozoic nappe units and main offshore and onshore faults. Abbreviations: NAF – North Anatolian fault, KF – Kefalonia fault, AVA – Aegean volcanic arc. (a) Modified from Ford et al. (2013). (b) Modified from Kranis et al. (2015).

3.2 Tectonic framework

3.2.1 The Aegean region

The interaction between the Eurasian, African and Arabian plates and the Anatolian and Aegean microplates results in different tectonic processes such as extensional deformation, subduction and strike-slip faulting in the Aegean region (Fig. 3.2) (e.g. McKenzie, 1970, McKenzie, 1972, 1978, Dewey & Sengor, 1979). Extensional deformation occurs in central Greece, the Peloponnese and at the plate boundary between the Anatolian and Aegean microplates in western Turkey (Armijo et al., 1996).

The Hellenic arc and trench system originated due to the subduction of the African plate beneath the Aegean microplate (McKenzie, 1970). Strike-slip faulting is mainly related to the dextral North Anatolian fault and the sinistral East Anatolian and Dead Sea faults, which form the plate boundaries between Eurasia and Anatolia, Arabia and Anatolia and Arabia and Africa, respectively (Armijo et al., 1996, Armijo et al., 1999, McClusky et al., 2000).
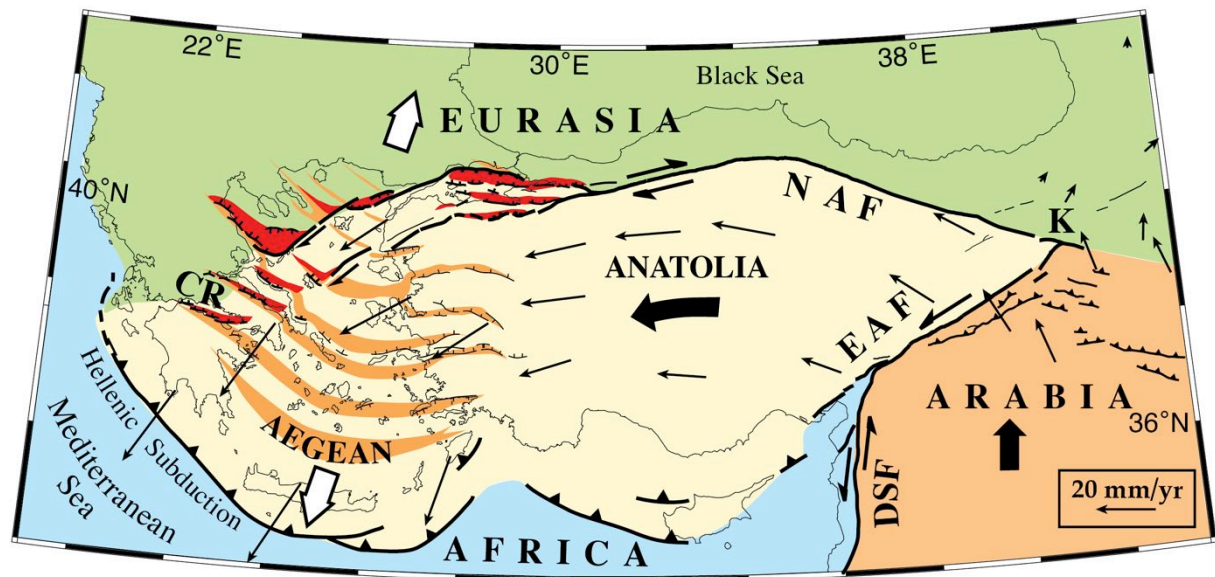
Figure 3.2 – Tectonic map of the Aegean region showing main plates, their boundaries and their relative movement. Red and orange stripes represent extensional deformation. Abbreviations: NAF – North Anatolian fault, EAF – East Anatolian fault, DSF – Dead Sea fault, K – Karliova triple junction, CR – Corinth Rift. Modified from Armijo et al. (1999).

The extensional deformation in central Greece is interpreted as the result of back-arc extension, gravitational collapse of over-thickened crust and the propagation of the dextral North Anatolian fault in a westward direction (e.g. Rohais et al., 2007, Bell et al., 2008, Ford et al., 2013). The extension at the back-arc region on the Aegean plate originated at the Late Eocene to Early Oligocene and is caused by the rollback of the African slab (Le Pichon & Angelier, 1979, Jolivet et al., 2013). The thickening of the crust during the emplacement of the Hellenic thrust sheets led to gravitational collapse, contributing to the extensional regime in the area (Jolivet et al., 1994, Jolivet, 2001). The propagation of the North Anatolian fault developed due to the collision between Arabia and Eurasia in the Miocene (Dewey & Sengor, 1979). The westward motion of Anatolia can be described by both a broken slats model (Taymaz et al., 1991) and extrusion

tectonics (Armijo et al., 1996, Armijo et al., 1999). In both models the North Anatolian fault propagated into the Aegean region (at 5 Ma sensu Armijo et al., 1996), where it splayed into a northern and a southern branch. The process zone of the southern branch reached the Corinth Rift at 1 Ma, which caused reactivation of the rift (Armijo et al., 1996, Armijo et al., 1999).

3.2.2 The Corinth Rift and the Corinth-Nemea basin

The N-S directed extension of the Corinth Rift has resulted in a series of N-dipping en echelon normal fault segments with an E-W to WNW-ESE orientation along the southern margin (Fig. 3.1) (e.g. Roberts & Jackson, 1991, Armijo et al., 1996). In contrast, the northern margin is characterized by several minor S-dipping antithetic faults. There are two main fault systems present at the study area (Goldsworthy & Jackson, 2001). One is located at the Perachora Peninsula and in the surrounding offshore regions, while the other one is found south of the Corinth Isthmus (Fig. 3.3).
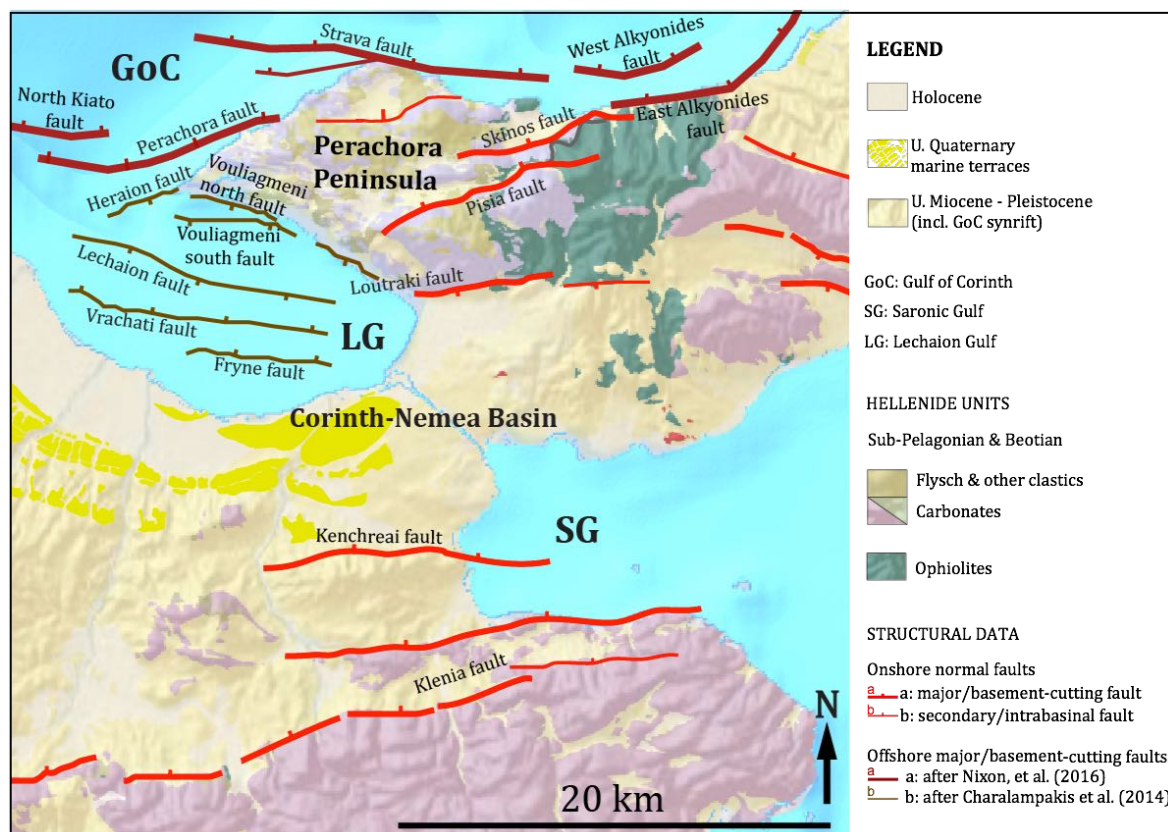

Figure 3.3 – (b) Geological map of the eastern Corinth Rift showing the two main fault systems present around the study area: The Perachora Peninsula fault system and the Kenchreai/Klenia fault system, located north and south of the Corinth Canal, respectively. Onshore deposits and Mesozoic nappe units are also indicated. Modified from Kranis et al. (2015).

Faults related to the Perachora Peninsula fault system can be grouped into: 1) offshore faults that are paralleling the coast and dips towards the N, 2) onshore faults and 3) faults that are dipping towards the S (Fig. 3.3) (Duffy et al., 2015). The Perachora, Strava, West Alkyonides and East Alkyonides faults represent the offshore, N-dipping, coast-parallel faults, and are located along the western and northern margins of the Perachora Peninsula. Several onshore faults are mapped on the Perachora Peninsula, but the largest and Holocene active are the N-dipping Pisia and Skinos faults. These faults produced significant surface faulting during a series of three earthquakes in 1981 (e.g. Jackson et al., 1982). The S-dipping faults are located offshore in the Lechaion Gulf and along the southern coastline of the Perachora Peninsula. These faults include the offshore Heraion fault, the offshore north and south Vouliagmeni faults and the Loutraki fault, which has an offshore and an onshore segment (Charalampakis et al., 2014). The Heraion fault has a length of ca. 4 km and the north and south Vouliagmeni faults have lengths of 5 km. The offshore segment of the Loutraki fault is 3 km long (Charalampakis et al., 2014), whereas the onshore segment has a length of 10.1 km and a throw of 800 m (Zygouri et al., 2008).

The fault system located south of the Corinth Isthmus constitutes two N-dipping faults: the Kenchreai fault and the Klenia fault (Fig. 3.3) (Goldsworthy & Jackson, 2001, Charalampakis et al., 2014). The northernmost one, the Kenchreai fault, has a length of 7.8 km and a throw of 300 m, whereas the southernmost one, the Klenia fault, has a length of 13.5 km and a throw of 300 m (Zygouri et al., 2008). It is thought that these faults extend into the Saronic Gulf, but due to the lack of published data from the Saronic Gulf the possible extensions are not a part of the given length values.

Several studies discuss whether the Kenchreai and Klenia faults represent ancestors to the currently active Skinos and Pisia faults located on the Perachora Peninsula (Fig. 3.3) (e.g. Goldsworthy & Jackson, 2001, Leeder et al., 2008). If that is the case, then the northward rift migration observed in the western part of the Corinth Rift has also occurred in the eastern part (e.g. Ori, 1989, Goldsworthy & Jackson, 2001, Rohais et al., 2007). It has been suggested that the fault migration in the eastern part of the Corinth Rift happened in a single step of 15 km (Bell et al., 2009). However, the recognition of two offshore N-dipping faults within the Lechaion Gulf, the Fryne and Vrachati faults,

indicate that the migration has occurred in steps of 7 km, which is consistent with steps of 5 km observed to the west (Charalampakis et al., 2014).

The Corinth-Nemea basin, which constitutes the Lechaion Gulf and its southern coast, the Corinth Isthmus and the Saronic Gulf, represent an asymmetric graben bound to the north and south by the Loutraki and Lechaion faults and the Kenchreai and Klenia faults, respectively (Fig. 3.3) (Collier & Dart, 1991, Charalampakis et al., 2014). The few studies conducted onshore on the Corinth Isthmus have recognized structural elements such as horst blocks, rotated fault blocks and grabens (Collier, 1990, Collier & Dart, 1991). The faults are both N- and S-dipping and E-W directed strikes are dominant. The faults in the NE part of the Corinth Isthmus are described as having varying geometries, including listric, planar and slightly curved (Collier & Dart, 1991). The deposits exposed in this area are mainly of Late Pliocene age and most of the faults are regarded as post-depositional. However, syn-depositional faults are also present, including a syn-depositional fault complex, which is characterized by listric normal faults trending E-W and bounding 40-100 m wide horst and grabens. Evidence for syn-depositional faulting are also observed by Collier (1990) in the Late Pleistocene to Holocene exposures of the Corinth Canal. As a result of concentration of syn-depositional fault movement on specific structures, a 1 km wide intrabasinal graben, the Isthmia Graben, was generated in the southeastern end of the canal.

Subsidence and uplift is affecting the Corinth-Nemea basin, with subsidence occurring in the Lechaion and Saronic Gulfs and uplift affecting the southern and northern margins of the Lechaion Gulf and the Corinth Isthmus (Fig. 3.3) (e.g. Collier & Dart, 1991, Collier et al., 1992, Leeder et al., 2003, Turner et al., 2010, Charalampakis et al., 2014). Maximum subsidence in the Lechaion Gulf is located towards north, in proximity to the Heraion and Vouliagmeni faults (Charalampakis et al., 2014). The uplift of the southern margin of the Corinth-Nemea basin is recorded by several marine terraces (e.g. Keraudren & Sorel, 1987). Various uplift models are proposed and these include footwall uplift of active faults and isostatic uplift related to the subduction of the African plate (e.g. Jackson et al., 1982, Collier et al., 1992, Armijo et al., 1996, Leeder et al., 2003, Turner et al., 2010). According to Leeder et al. (2003) the region is affected by uniform isostatic uplift with an uplift rate of 0.3 mm/yr since late Quaternary (Collier, 1990, Collier et al., 1992).

Alternatively Turner et al. (2010) argue for a non-uniform isostatic uplift of the southern margin of the Lechaion Gulf and the Corinth Isthmus, with uplift rates of 0.19 ± 0.05 mm/yr at the Corinth Canal increasing to 0.31 ± 0.05 mm/yr further towards the SW, during the same time interval. Charalampakis et al. (2014) state that the uplift of the region is even more complex and that the Vrachati fault is responsible for the uplift of the southern margin of the Lechaion Gulf.

3.3 Stratigraphic framework

3.3.1 Pre-rift

The pre-rift basement of the Corinth Rift is composed of Hellenic nappes of Mesozoic age (e.g. Le Pourhiet et al., 2003, Rohais et al., 2007, Skourtsos & Kranis, 2009, Taylor et al., 2011, Ford et al., 2013). The pile of nappes is divided into several units, and five of these units are exposed in the area surrounding the Gulf of Corinth; the Zarouchla Complex, the Tripolis Unit, the Pindos Unit, the Parnassos Unit and the Sub-Pelagonian and Beotian Unit (Fig. 3.1). Nevertheless, none of these units are exposed in the study area. However, by analyzing the composition of the syn-rift deposits exposed within the study area the pre-rift units can be utilized to determine possible sources for the syn-rift sedimentary rocks. Within the Corinth Canal the syn-rift deposits are composed of sediments sourced from the Sub-Pelagonian and Beotian Unit, which is made up of limestones and cherts, in addition to the Geraneia ophiolite emplaced in Palaeogene (Collier, 1990).

3.3.2 Syn-rift

The onshore syn-rift deposits of the Corinth Rift are mainly described based on studies conducted on the Gulf of Corinth southern coast in the western and central parts of the rift (e.g. Ori, 1989, Rohais et al., 2007, Ford et al., 2013). These deposits can reach a maximum thickness of 2800 m and its stratigraphy has been divided up into a Lower-, Middle- and Upper Group. The Lower Group comprises Pliocene to Earliest Pleistocene alluvial to lacustrine deposits (<5 to 1.8-1.5 Ma, Ford et al., 2013). The Middle Group is constituted by Early- to Middle Pleistocene Gilbert-type fan deltas that propagated northwards (1.8-1.5 to 0.7-0.5 Ma, Ford et al., 2013). The Upper Group was deposited from Middle Pleistocene (0.7-0.5 Ma, Ford et al., 2013) to present, and contain deposits

related to uplifted terraces, breccias and small Gilbert-type deltas. The offshore syn-rift deposits of the Corinth Rift can reach a maximum thickness of ca. 2500 m and are divided up into two seismic units, Seismic Unit 1 (SU1) and Seismic Unit 2 (SU2) (Nixon et al., 2016). These seismic units are separated by a basin-wide unconformity and represent equivalents to the onshore syn-rift deposits of the Middle- and Upper Group, respectively.

Only a few studies are conducted on the onshore syn-rift deposits exposed in the Corinth Canal and the Corinth-Nemea basin (Collier, 1990, Collier & Dart, 1991, Collier & Thompson, 1991). The syn-rift deposits exposed in the NE part of the Corinth Isthmus are the basis for the three-fold stratigraphic division of the Corinth-Nemea basin fill (Collier & Dart, 1991): 1) Lower Pliocene Group, 2) Trapeza-Isthmos Group and 3) fan-delta of Holocene age. The Lower Pliocene Group represents the oldest deposits. It is overlain by andesites that have been dated to 3.5-4.5 Ma and the Lower Pliocene Group is therefore time equivalent with the Lower Group to the west. These deposits are more than 800 m thick and consist of marls, siltstones, sandstones and conglomerates, which were sourced from alluvial fans and fan-deltas from the northern and southern margins and from an axial system sourced from the west and deposited in alluvial, lacustrine and marine environments. The observation of serpentinite and peridotite clasts suggests a northern source due to the unroofing of the Paleogene-emplaced Geraneia ophiolite located there. The Lower Pliocene Group also contains sands with more than 90 % serpentinite that was sourced from a western, now eroded, ophiolite.

The Late Pleistocene Trapeza-Isthmos Group is exposed in the Corinth Canal and based on U/Th dating of in situ *Acropora* corals (>350 ka to 205 ka; Collier, 1990) it is interpreted to be time equivalent to the Upper Group towards the west. The deposits of the canal section are composed of offshore marls and beachface/alluvial sandstones and conglomerates (Collier, 1990). Six marine transgressive cycles are identified in the northwestern part of the canal and these are all capped by unconformities. Each transgressive cycle represents a Late-Quaternary glacio-eustatic highstand, which occurs approximately every 100 kyr. This conclusion was drawn based on the dated corals in the canal section.

The Late Pleistocene marine and coastal deposits exposed in the central and the southern parts of the Corinth-Nemea basin were also dated by U/Th techniques on corals (232 ka to 177.1 ka; Collier & Thompson, 1991). Even though these share a similar age with the deposits at the northern part of the basin they differ in character. Only small amounts of clastic material are present together with oolitic calcareous sandstones in the central and southern Corinth-Nemea basin. This difference can be explained by the existence of a narrow seaway, which connected the Saronic Gulf with the Gulf of Corinth during the Marine Isotope Stage 7 (MIS 7). The seaway was formed due to the subsidence of the Isthmia Graben, and resulted in funneling of tidal currents, which incised the deposits and stopped the progradation of clastics from the northern margin. The funneling effect also resulted in the formation of the transverse and linear dunes observed in the southern part of the basin.

4 Database and Methods

The study is both field- and LiDAR-based and the aim of this chapter is to provide an overview of the database (section 4.1) and methods applied during fieldwork (section 4.2) and interpretation of the digital outcrop data (sections 4.3 and 4.4). Additionally, section 4.3 gives a short introduction to the application and advantages of terrestrial laser scanning in geoscience and the software utilized in this study. An overview of the quantitative fault analyses conducted in this study is addressed in section 4.4, while section 4.5 considers the limitations related to the study.

4.1 Database

The study area covers both walls of the Corinth Canal over a stretch of approximately 2.1 km. Faults with maximum throw larger than 1 m are included in the structural analysis. The database consists of orientation data for a total of 26 surfaces and 23 faults (Fig. 4.1). Measurements of throw and heave were collected for one stratigraphic interval on the western canal wall. Additionally, most faults, except faults FS8, FS9, FS9.1 and FS11, have throw and heave measurements from at least five stratigraphic intervals, making it possible to create throw-depth plots. Throw and heave measurements are from both canal walls except for the faults that do not link over the canal (FN1.1 and FS1.1). True stratigraphic thickness was measured in the immediate foot- and hanging wall of faults at the same stratigraphic intervals as the throw measurements. These measurements were used to calculate expansion indices. Furthermore, the database comprises the length and amplitudes of folds.
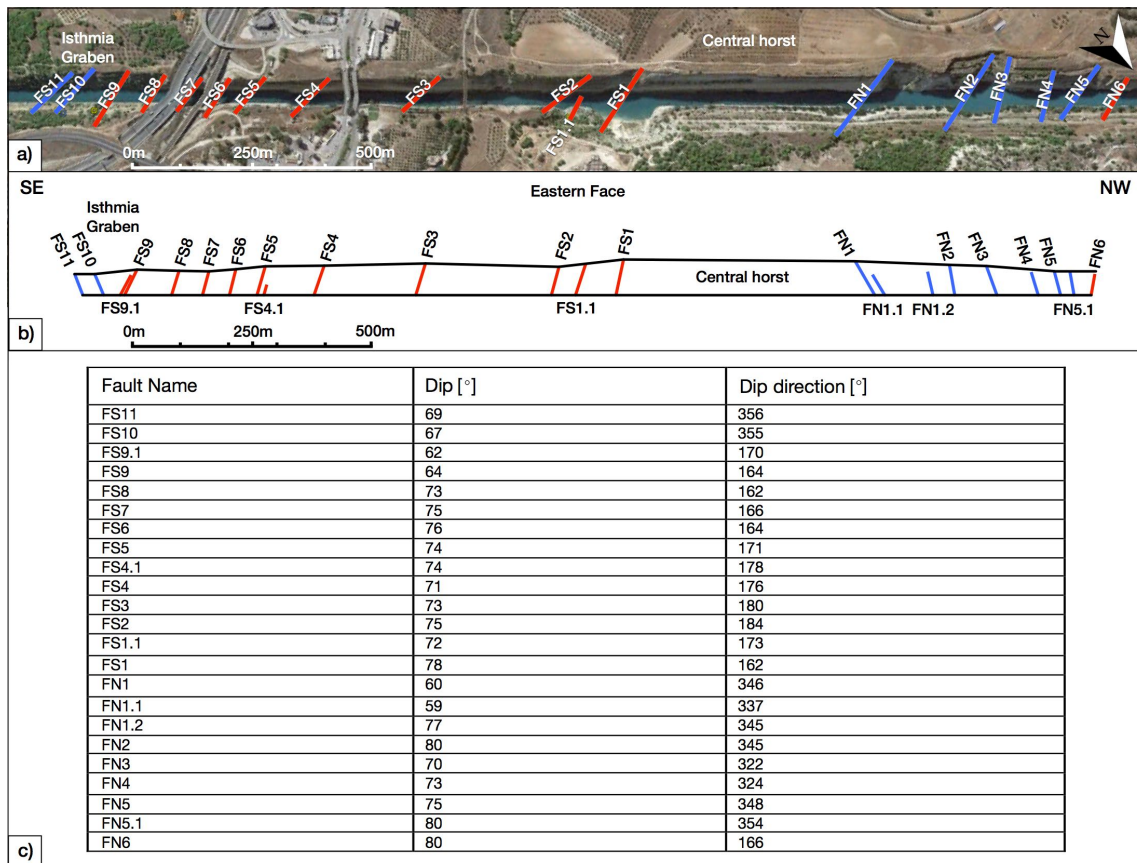
Fig. 4.1 – (a) Fault map that shows the location of faults that cut across all exposed stratigraphy. (b) Cross-section of the eastern canal wall indicating the location of all faults within the study area. The color of the faults represents their dip direction. Blue faults dip to N-NW while red faults dip to S-SSE. (c) Table of the 23 faults with their dip and dip direction.

4.2 Fieldwork

Fieldwork was conducted during two field seasons, each lasting approximately three weeks. The first season was from 18th of March to 4th of April 2015, while the second one was from 24th of September to 15th of October 2015. Most of the fieldwork was carried out independently or together with a fellow student, Sturla Vatne Meling. Additionally, my supervisor Rob Gawthorpe, my co-supervisor Martin Muravchik, researcher Gijs Allard Henstra and Haralambos Kranis and Manolis Skourtsos from the University of Athens came with us to the field for a few days, offering guidance and instructions.

Standard field equipment, in addition to a digital camera, binoculars, a laser rangefinder (TruPulse 360 series) and a GPS was utilized in the field. The purpose of the fieldwork was to determine the overall stratigraphy of the Corinth Canal and to map, measure and describe the different faults exposed in the canal section.

4.2.1 Sedimentary logging and photo panel interpretations

Most of the rocks and faults in the canal section are inaccessible, and have to be observed from the opposite side of the canal through binoculars. However, there is a manmade ramp on the eastern wall, extending from the horst and towards NW, which makes it possible to have a closer look at the rocks and faults located in this area. In collaboration with fellow student Sturla Vatne Meling, a composite log was generated for the deposits exposed in the central horst. This log represents the foundation of the canal stratigraphy. Stratal surfaces and sediment packages recognized while logging were correlated along the canal with the aid of photo panels and binoculars.

A total of 26 surfaces were mapped within the study area (Table 4.1). These surfaces were defined based on the following characteristics: angular unconformities, erosional truncations, onlap, downlap, basinward shifts in facies, landward shifts in facies, calcretisation/karstification, paleo-cliffs, presence of conglomerate lag and changes in lithology across the surface (Fig. 4.2). The surfaces frequency shows several characteristics when tracing it along the canal section. Key stratal surfaces in the study area are surfaces S2, S3, S4, S5 and S8, since these bound tectonostratigraphic units.

4.2.2 Structural analysis and photo panel interpretations

The location of mapped faults was documented by GPS-positions and on topographic maps of the canal. Every fault was sketched and described with emphasis on geometry and fault zone architecture and transferred over to photo panels. A range finder was utilized to measure the throw of the faults and the thicknesses of sediment packages across the faults. The mapped stratal surfaces and additional markers were used in this work. Throughout this thesis additional markers are called M1, M2, etc. These markers are independent from one another and are commonly not the same for faults that link over the canal. More detailed descriptions in addition to strike and dip measurements were collected for the faults exposed along the manmade ramp on the eastern canal wall.

Table 4.1 – Surfaces within the study area were mapped based on their different characteristics: angular unconformities, erosional truncations, onlap terminations, downlap terminations, basinward shift in facies, landward shift in facies, calcretisation/karstification, paleo-cliffs, conglomerate lag and lithology boundary. The table summarizes the 26 surfaces mapped in the canal section and their characteristics. The colored surfaces represent key stratal surfaces: surface S2 (light green), surface S3 (purple), surface S4 (blue), surface S5 (yellow) and surface S8 (dark green). The table is arranged by relative age of the surfaces with the oldest surface, S1, at the base of the table and the youngest surface, S13, at the top of the table.

Surface	Angular unconformity	Erosional truncation	Onlap	Downlap	Basinward shift in facies	Landward shift in facies	Calcrete/karst	Paleo-cliff	Conglomerate lag	Lithology boundary
S13						X				X
S12		X	X	X	X			X		X
S11						X				X
S10.2				X						X
S10.1				X						
S10		X	X	X	X			X		X
S9			X			X				X
S8.2				X	X					X
S8.1				X	X					X
S8	X	X	X	X	X	X	X	X		X
S7					X	X				X
S6.1						X				X
S6		X	X	X	X				X	X
S5.3									X	X
S5.2						X				X
S5.1		X	X		X					X
S5	X	X	X	X	X				X	X
S4.3				X						
S4.2						X				X
S4.1					X					X
S4	X	X				X				X

Figure 4.2 – View of the digital outcrop model for the western wall of the Corinth Canal in the area of fault FN1 (see Fig. 4.1 for location). Different types of stratal relations are recognized within the study area. Stratal terminations (onlap, downlap and erosional truncation) are indicated with arrows. The colors of the surfaces are the same as in table 5.1 with light green representing surface S2, purple representing surface S3, blue representing surface S4 and dark green representing surface S8.

4.3 LiDAR-based digital outcrop data

By combining traditional fieldwork and terrestrial laser scanning (LiDAR), geoscientists now have the opportunity to capture large amounts of geological outcrop data with high accuracy and resolution during a relatively short period of time (e.g. Bellian et al., 2005, Buckley et al., 2008, Rotevatn et al., 2009). LiDAR (Light Detection And Ranging) is applied both in a stratigraphic and a structural context, where structures at a scale of centimeters to kilometers can be mapped and investigated (e.g. McCaffrey et al., 2005, Enge et al., 2007, Rotevatn et al., 2009, Wilson et al., 2009, Buckley et al., 2010).

In this study LiDAR data was used to extract stratigraphic and structural data to supplement field observations and to obtain data from areas that were inaccessible in the Corinth Canal. My co-supervisor Martin Muravchik was responsible for acquiring and processing the LiDAR data. A RIEGL VZ-1000 scanner was utilized to collect the data. For details on data acquisition, processing techniques and the accuracy of LiDAR see Buckley et al. (2008), Hodgetts (2009) and Rarity et al. (2014).

The interpretation software utilized in this study is Virtual Reality Geological Studio (VRGS, V2.23). This software enables the user to study outcrops in 3D view and to make interpretations directly on the virtual outcrop. All interpretation was carried out on triangular meshes (TINs), which were generated from imported point clouds in VRGS. The stratigraphy was interpreted by picking polylines along sedimentary surfaces, while the faults were interpreted by adding fault sticks along fault traces (for details on workflow see Hodgetts, 2009, Rarity et al., 2014).

4.4 Quantitative Fault analyses

4.4.1 Fault orientations

Fault interpretations were imported into CloudCompare where a best fit plane was calculated. The orientation of the best fit plane represents the average orientation of the faults. For faults that do not link over the canal the orientations are the ones given in VRGS. If such a fault is composed of several fault segments, the average strikes and dips were calculated to represent the orientation of the fault.

4.4.2 Throw-depth (T-z) plots

T-z plots show the distribution of throw with depth and are utilized to determine the possible role of dip linkage (e.g. Mansfield & Cartwright, 1996, Tvedt et al., 2013). Such plots and their throw gradients can also be used to determine whether a fault was blind or breached the surface (e.g. Jackson & Rotevatn, 2013). High throw gradients represent syn-sedimentary growth faults, whereas low throw gradients may represent blind faults, but can also imply syn-sedimentary growth faults with high sediment accumulation rates (e.g. Childs et al., 2003, Jackson & Rotevatn, 2013).

Vertical throw profiles can be described and interpreted based on their overall shape (Fig. 4.3 and 4.4) (Baudon, 2007, Tvedt et al., 2013). The nucleation point of a fault frequently corresponds to maximum throw on a T-z plot (e.g. Hongxing & Anderson, 2007, Osagiede et al., 2014). An idealized isolated blind fault has a symmetrical T-z plot where maximum throw is located in the center and throw is progressively decreasing to zero at the upper and lower fault tips, creating triangular or C-shaped throw profiles (Fig. 4.3c) (e.g. Barnett et al., 1987, Baudon, 2007, Osagiede et al., 2014). However, idealized isolated blind faults do not exist in nature and Baudon (2007) showed that the T-z plots of blind faults usually have Mesa- or hybrid shapes, due to lithological differences or interaction with other structures. Asymmetric and skewed throw profiles characterize surface breaching growth faults as such faults are restricted towards the surface. If a syn-sedimentary growth fault link with a blind fault that nucleated in the overburden, the throw profile exhibit two throw maximum that is separated by a throw minimum (Fig. 4.4b) (Tvedt et al., 2013). Throw minimum is the linking point between the two faults. When a syn-sedimentary fault and a blind fault located in the overburden do not link, the result is two separate throw profiles (Fig. 4.4c).
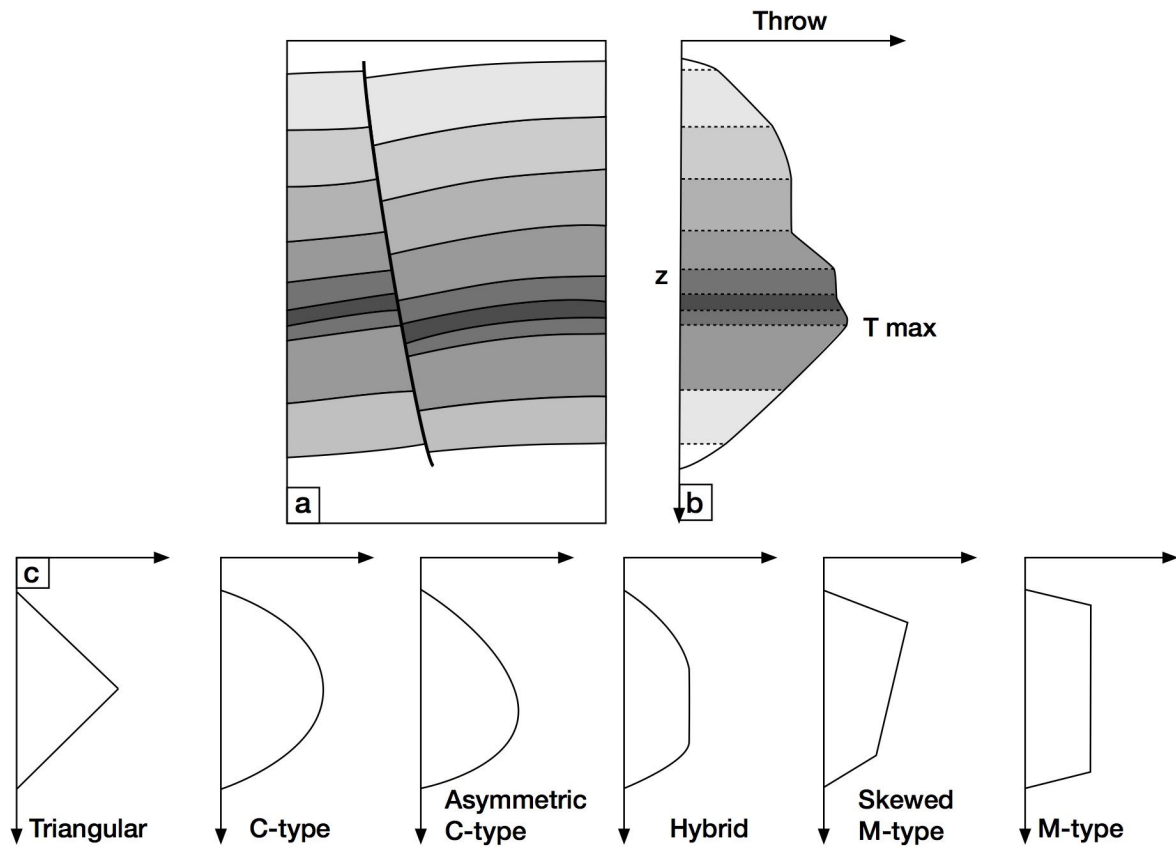
Fig. 4.3 – (a) Schematic illustration of a normal fault offsetting sedimentary layers. (b) Throw-depth (T-z) plot of the fault illustrated in (a). (c) Schematic illustration of different styles of T-z plots. Redrawn from Baudon (2007).
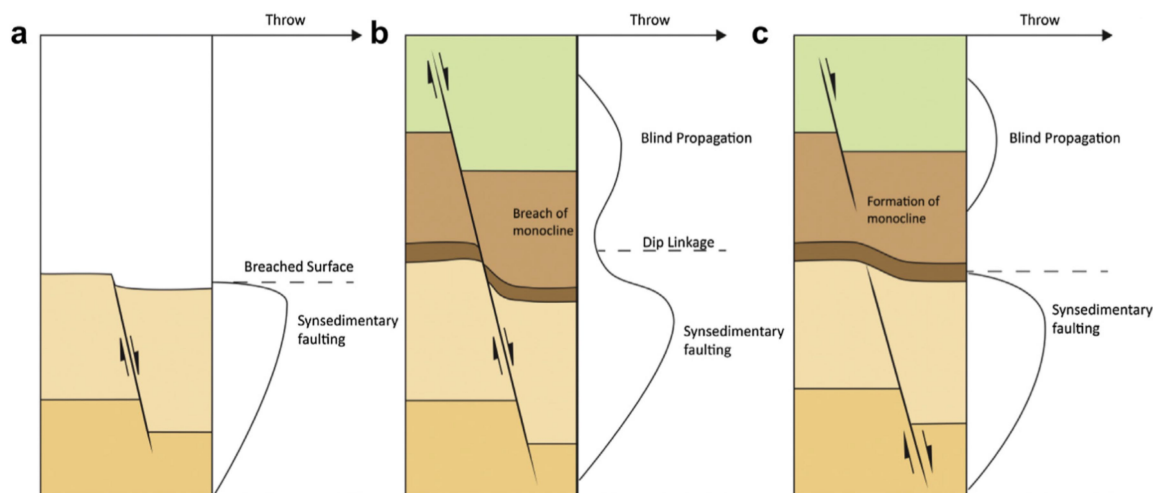

Fig. 4.4 – Schematic illustration of T-z plots for (a) a syn-sedimentary fault, (b) a syn-sedimentary fault that links with a blind fault in the overburden and (c) a syn-sedimentary fault with a blind fault in the overburden. From Tvedt et al. (2013).

28

In this study throw was plotted against meters above sea level at the midpoint between hanging wall and footwall cutoffs (Fig. 4.5). In places where local folding occurs throw was measured based on extrapolation from the unfolded part of the stratal surface to the fault plane. Faults FS8, FS9, FS9.1 and FS11 do not have T-z plots due to a combination of too few markers, bad scans and that the outcrop is covered by vegetation and brick walls.
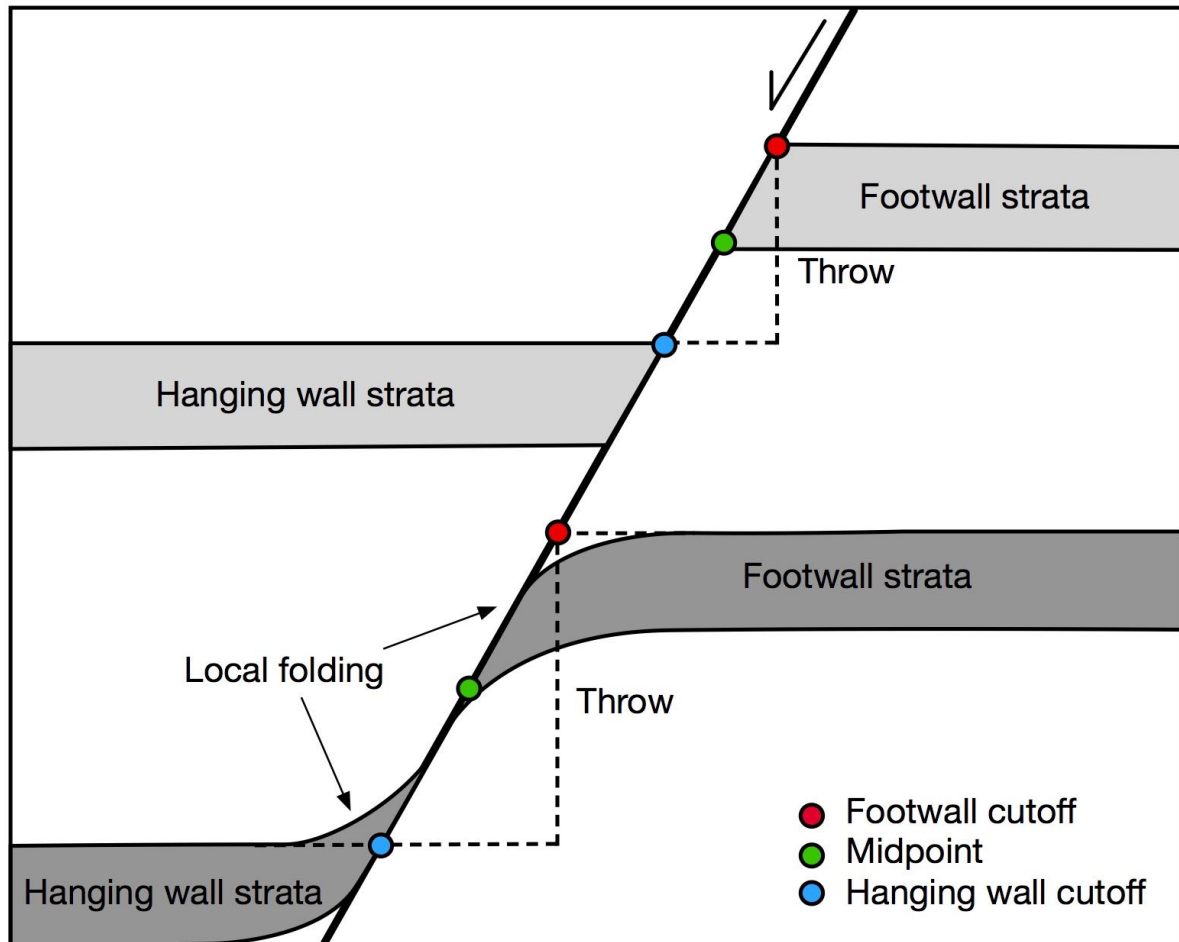

Fig. 4.5 – Schematic illustration of how throw was measured and where throw was plotted on the T-z plots. Where local folding occurred, extrapolation from the unfolded part of a stratal surface to the fault plane was conducted.

4.4.3 Expansion indices

Expansion indices, which is a dimensionless ratio of thickening across faults, can be utilized to determine the growth history of faults (e.g. Thorsen, 1963, Cartwright et al., 1998, Jackson & Rotevatn, 2013). This ratio is found by dividing the true stratigraphic thickness of a sediment package located in the hanging wall with the true stratigraphic thickness of the corresponding sediment package in the footwall. An expansion index that is larger than one implies thickening of hanging wall strata and may indicate syn-sedimentary growth faulting, while an expansion index that is less than one indicates thinning of hanging wall strata (Cartwright et al., 1998, Hongxing & Anderson, 2007). If the expansion index equals to one this implies no thickness change between hanging wall and footwall strata and indicates that the fault was buried or inactive during the deposition of the strata.

Expansion indices were measured at the same stratigraphic intervals as the corresponding T-z plot. These measurements were carried out in VRGS with the aid from contour maps generated in ArcGIS.

4.4.4 Cumulative plots

From cumulative plots of fault frequency, throw and heave, it is possible to determine the heterogeneity of the fault population. This is done by comparing the cumulative fault frequency, throw and heave against a uniform distribution (Fig. 4.6) (Putz-Perrier & Sanderson, 2008a, 2008b). A heterogeneity parameter, $V = |D^+| + |D^-|$, can be calculated from the maximum deviation above (D^+) and below (D^-) the uniform distribution. The heterogeneity parameter needs to be normalized, which is done by dividing it by the cumulative total. A V-value of zero indicates a homogeneous distribution where the faults are equally spaced and have the same amount of throw and heave. A V-value of one implies a heterogeneous distribution, where one fault takes up all throw and heave.
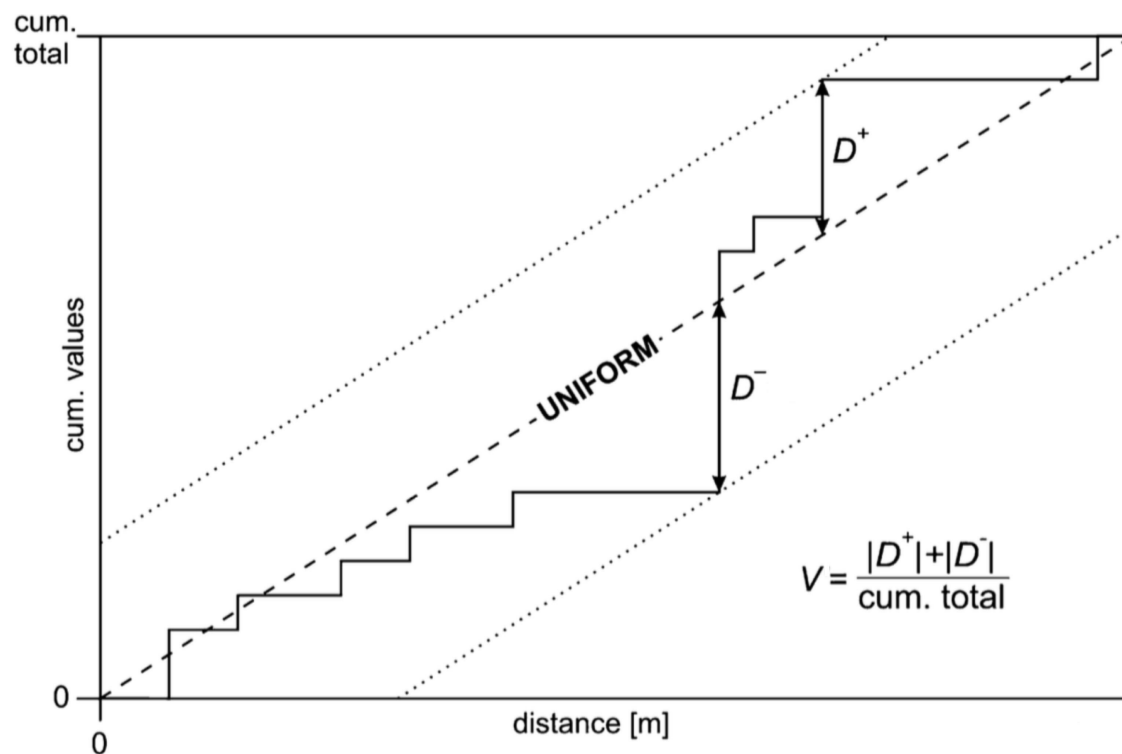
Figure 4.6 – Cumulative plot. D^+ and D^- are the maximum deviations above and below the uniform distribution (dashed line). Modified from Putz-Perrier and Sanderson (2008b).

4.5 Limitations

Both the stratigraphic framework and the structural analysis is limited by the inaccessibility to large portions of the outcrops exposed in the Corinth Canal, which make detailed observations of sediments and fault zones very difficult. The vertical extent of the outcrop is another limitation. For most faults neither the upper or lower fault tip is exposed within the canal section making it impossible to determine with certainty where the faults nucleated and their entire growth history. Second World War bomb-sites, vegetation and brick walls cover parts of the outcrop making it hard to interpret stratigraphy and faults in these areas.

5 Stratigraphic framework

In order to determine the relative timing and growth history of normal faults exposed in the study area, a detailed stratigraphic framework for the exposures in the canal had to be established. Thus, the aim of this chapter is to present the stratigraphy of the Corinth Canal. The chapter focuses on stratal surfaces (section 5.1) and the division of the canal stratigraphy into tectonostratigraphic units (section 5.2). For a more detailed description and interpretation of the sedimentology and stratigraphy see Meling (2016).

5.1 Stratal surfaces

5.1.1 Surface styles

Surfaces exposed within the study area are divided into three main surface styles and include facies shifts across surfaces, angularity between surfaces and underlying strata and erosion of underlying strata. The facies shifts are either in a basinward or a landward direction. Many of the exposed surfaces show several of these characteristics.

5.1.2 Variability and geometry

Surfaces in the central horst are generally subhorizontal, but can dip up to 7.4°. In the SE part of the central horst the surfaces are dipping towards NE and E with average dips between 0° to 3.7°. Surfaces in the NW part of the central horst are dipping towards NW and N with average dips that range between 1.9° and 7.4°. The higher dips in the NW part of the central horst are related to monocline structures observed below surface S8 towards the NW horst-bounding fault (FN1) (Fig. 4.2).

The surfaces both NW and SE of the central horst predominantly dip towards NW. To the NW of the central horst the surfaces have average dips that range between 1.2° and 7.0°, whereas the surfaces to the SE of the central horst have average dips that range between 0.7° and 13.6°. The dip of the surfaces to the SE of the central horst increases progressively from one fault block to the next one away from the horst-bounding fault (FS1) towards the SE (Fig. 4.1 for location). This trend ceases at the first N-dipping fault towards SE (FS10), which is located within the Isthmia Graben.

5.2 Stratal units and tectono-stratigraphy

The stratigraphy in the canal is divided into 14 stratal units based on major landward or basinward shifts in facies (Table 5.1). These stratal units are mapped within the central horst and towards NW and SE for 730 m and 935 m, respectively (Fig. 5.1). Within the Isthmia Graben, which is located at 1010 m SE of the central horst, the stratigraphy does not have the same resolution since rocks are poorly exposed due to the presence of brick walls and extensive vegetation. The 14 stratal units are further divided into six tectonostratigraphic units based on identification of changes in thickness trends, major shifts in facies and major erosion related to tectonic events (Fig. 5.1).

5.2.1 Tectonostratigraphic Unit 1

Observations

The upper boundary of Tectonostratigraphic Unit 1 is surface S2, while the lower boundary is located below sea level (Fig. 5.1). Surface S2 is the boundary between siltstones and overlying sandstones and truncates the underlying strata in the central horst. The entire unit is composed of siltstones and contains the gastropod *Viviparus sp.* (Collier, 1990). Parallel bedded siltstones are observed above an internal surface (surface S1), whereas NW-dipping siltstones are observed below this surface resulting in an angular unconformity between surface S1 and the underlying deposits. The unit is mainly exposed within the central horst and down faulted below sea level in the hanging wall of the horst-bounding fault towards NW (FN1). Southeast of the central horst the unit is exposed for 420 m along the lower wall section of the canal.

Interpretations

Surface S2 is the boundary between siltstones and overlying sandstones, which indicates a basinward shift in facies across the surface. The occurrence of *Viviparus sp.* suggests a lacustrine environment (Collier, 1990). Furthermore, the unit is interpreted to be deposited in a deep-water setting due to its fine grained character.

Table 5.1 – The stratigraphy within the study area is divided into 14 stratal units. The table summarizes key characteristics of these stratal units including their bounding surfaces, lithology, internal sedimentary structures, external geometry and whether the units are associated with thickening across one or several faults. The table is arranged by relative age of the stratal units with the oldest unit, SU1, at the base of the table and the youngest unit, SU13, at the top of the table. The colors of the different stratal units represent what tectonostratigraphic unit the stratal unit is a part of (same color scheme as fig. 5.1b): Tectono-strat Unit 1 (gray), Tectono-strat Unit 2 (orange), Tectono-strat Unit 3 (green), Tectono-strat Unit 4 (red), Tectono-strat Unit 5 (blue) and Tectono-strat Unit 6 (yellow).

| Unit	Lower boundary	Upper boundary	Lithology	Internal sedimentary structures	External geometry	Across-fault thickening
SU14	S13	Top of canal	Sand	Parallel bedding	Not fully exposed	Not fully exposed
SU13	S12	S13	Conglomerate	Cross-bedding	Tabular	No thickening
SU12	S11	S12	Sand	Parallel bedding	Tabular, irregular due to irregular substrate	No thickening
SU11	S10	S11	Conglomerate	Cross-bedding	Tabular, wedge deposited above irregular substrate	No thickening
SU10	S9	S10	Sand	Parallel bedding	Tabular, partially eroded in some places	FN1, FN4
SU9	S8	S9	Conglomerate and sand	Cross-bedding and parallel bedding	Tabular, wedge deposited in hanging wall of fault FS1	FN1, FN4, FS1, FS10
SU8	S7	S8	Marl, sand and conglomerate	Parallel bedding	Tabular, partially eroded in hanging wall of fault FS1	FS3, FS4, FS5, FS10
SU7	S6	S7	Marl, sand and conglomerate	Parallel bedding and cross-bedding	Tabular	FS2, FS5, FS6
SU6	S5	S6	Marl, sand and conglomerate	Parallel bedding and cross-bedding	Tabular, folded in footwall of fault FS1	FS2, FS6
SU5	S4	S5	Marl, sand and silt	Parallel bedding	Tabular, partially eroded with wedges deposited in some places	FN1, FN1.2, FN3, FN4, FN6, FS4, FS4.1
SU4	S3	S4	Sand and silt	Parallel bedding and slumping	Tabular, partially eroded and folded in some places	FN1.1
SU3	S2	S3	Sand and silt	Parallel bedding	Tabular, folded in some places	No thickening
SU2	S1	S2	Silt	Parallel bedding	Folded	Not fully exposed
SU1	Below sea level	S1	Silt	Parallel bedding	Not fully exposed	Not fully exposed
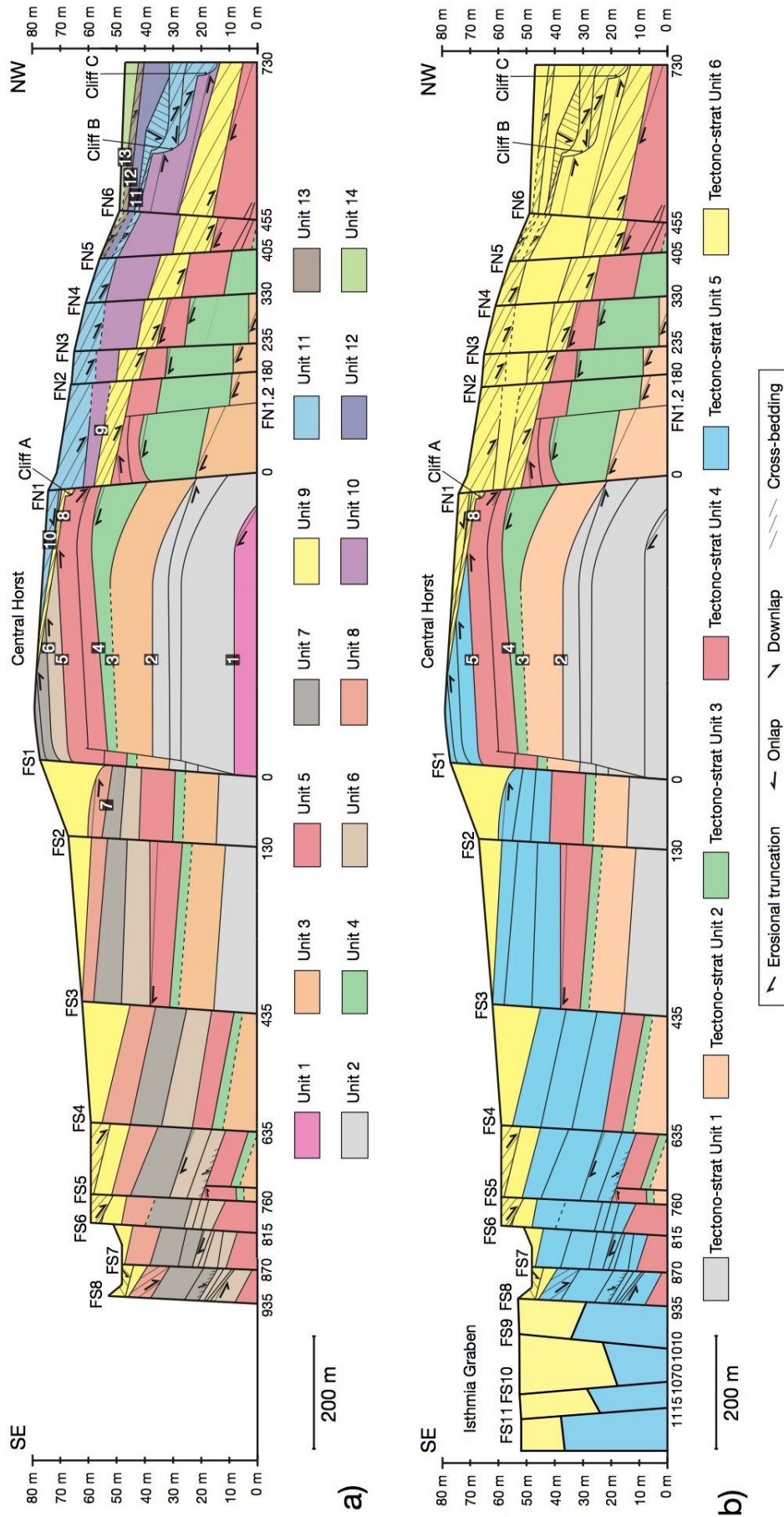
Figure 5.1 – Schematic illustration of the stratigraphy exposed on the western canal wall. (a) Division of the stratigraphy into 14 stratal units and (b) division of the stratal units into six tectonostratigraphic units. The Isthmia Graben is included in the tectonostratigraphic model. Dashed lines represent uncertain parts of the surfaces and is interpreted based on the overall chracteristics of the surface in question. The vertical axis is exaggerated by five compared to horizontal axis. Modified from Meling (2016)

5.2.2 Tectonostratigraphic Unit 2

Observations

Surface S3 represents the upper boundary of Tectonostratigraphic Unit 2 and the lower boundary is surface S2 (described in section 5.2.1) (Fig. 5.1). In the immediate hanging wall of the NW horst-bounding fault (FN1) and further towards NW, surface S3 is an angular unconformity. In this area surface S3 separates NW-dipping siltstones from overlying slumped siltstones. In the central horst and towards SE surface S3 represents a surface where parallel bedded sandstones are observed above and below the surface.

The intervals where both bounding surfaces, S2 and S3, are exposed, the thickness of the unit is more or less constant (ca. 13 m) (Fig. 5.1). The unit is composed of parallel bedded sandstones in the central horst until it disappears into the canal 760 m SE of the central horst. Northwest of the central horst the unit is exposed for 330 m and is composed of NW-dipping siltstones. The gastropod *Viviparus sp.* is observed within the unit (Collier, 1990).

Interpretations

The presence of the gastropod *Viviparus sp.* implies a lacustrine environment (Collier, 1990). Since the unit is composed of siltstones in the immediate hanging wall of fault FN1 and towards NW, this part of the unit is interpreted to be deposited in a deep-water setting due to the fine grained character of the siltstones (Fig. 5.1). However, in the central horst and towards SE the lower boundary of the unit, surface S2, represents a basinward shift in facies across the surface, with siltstones below the surface and sandstones above the surface. This shift in facies and the coarser grained character of the sandstones imply shallow-water depths. Thus, the unit is composed of both shallow-water and deep-water lacustrine deposits, with the shallow-water deposits occurring in the central horst and towards SE and the deep-water deposits occurring NW of the central horst.

5.2.3 Tectonostratigraphic Unit 3

Observations

Tectonostratigraphic Unit 3 is bounded by surface S4 at its upper boundary and by surface S3 (described in section 5.2.2) at its base (Fig. 5.1). In the central horst and NW of the central horst surface S4 truncates the underlying strata and represents an angular unconformity. The surface show variations in lithology above and below the surface when moving along the canal. Lithologies above surface S4 are parallel bedded marls or sands, whereas the lithologies below surface S4 are sands or silts that show parallel bedding or slumping. The gastropod *Viviparus sp.* occurs below surface S4 and *Cardium sp.* and other bivalves occur above surface S4 (Collier, 1990).

The unit has a constant thickness of approximately 4 m SE of the central horst and in the SE part of the central horst (Fig. 5.1). In the NW part of the central horst the unit is thickening and this trend continues further towards NW (ca. 16 m in the central horst and ca. 25 m furthest towards NW). Across-fault thickening is only occurring for one of the faults in the study area (FN1.1), which is located NW of the central horst (Fig. 4.1 for location). The unit is composed of parallel bedded sandstones in the central horst and within the exposed interval of 760 m SE of the central horst. Northwest of the central horst the unit is exposed for at least 405 m and is composed of siltstones that are slumped or have parallel bedding.

Interpretations

Surface S4 represents a landward shift in facies across the surface due to the recognition of a marine incursion where lacustrine fauna (e.g. *Viviparus sp.*) are observed below surface S4 and marine fauna (e.g. *Cardium sp.*) is observed above surface S4 (Collier, 1990). The occurrence of *Viviparus sp.* within the unit indicates a lacustrine environment. Similar to Tectonostratigraphic Unit 2 sandstones are occurring in the central horst and towards SE, indicating shallow water depths. In contrast, NW of the central horst the unit is composed of siltstones implying deeper water depths. Consequently, shallower conditions existed on the central horst and the area to the SE, with the lake deepening to the NW of the central horst.

5.2.4 Tectonostratigraphic Unit 4

Observations

The upper boundary of Tectonostratigraphic Unit 4 is surface S5 in the SE part of the central horst and towards SE and surface S8 in the NW part of the central horst and towards NW (Fig. 5.1). The lower boundary of the unit is surface S4, which is described in section 5.2.3. Surface S5 is an angular unconformity between 130 m to 435 m and 635 m to 760 m SE of the central horst. The surface frequently has the same lithologies (marls or sands) above and below the surface. However, in the interval between 635 m and 815 m SE of the central horst surface S5 represents a boundary between sandstones and overlying conglomerates. Surface S8 in the NW part of the central horst and towards NW truncates the underlying strata, which in most places have an angular relationship to surface S8. The surface is a boundary between cross-bedded conglomerates and underlying marls, sandstones or siltstones.

No large scale thickening trend is observed for Tectonostratigraphic Unit 4 (Fig. 5.1). However, the unit shows significant thickening across the NW horst-bounding fault (FN1) and most of the faults located further towards NW (FN1.2, FN3, FN4 and FN6). Southeast of the central horst across-fault thickening is observed for faults FS4 and FS4.1.

Internally the unit has lateral changes in lithology. Marls are observed in the central horst and in the immediate hanging wall of the horst-bounding faults both towards SE and NW (Fig. 5.1). These marls contain *Cardium sp.* and other bivalves (e.g. *Pecten sp.*) (Collier, 1990). From 435 m SE of the central horst and until the unit disappears below sea level at 935 m, the unit is composed of sandstones that contain shells. A similar trend is observed NW of the central horst with sandstones occurring between 180 m and 330 m and siltstones occurring from 330 m until the extent of the study area is reached. The sandstone deposits NW of the central horst contains reworked bivalves (e.g. *Pecten sp.*). Furthermore, thin packages of conglomerates occur within the unit NW of the central horst.

Interpretations

Both surfaces S5 and S8 indicate a basinward shift in facies across the surface based on the observation that conglomerates overlie marls, sandstones or siltstones. Additionally, the small packages of conglomerates that are observed within Tectonostratigraphic Unit 4 indicate small landward and basinward shifts in facies.

The observation of marine fauna within the unit (e.g. *Pecten sp.* and *Cardium sp.*) implies a marine environment (Collier, 1990). The marls in the study area are calcareous silts, which indicate deep-water conditions based on the fine grained character of these deposits. Hence, the marl deposits are interpreted to be offshore marine, which is also the case for the siltstones observed NW of the central horst. However, the sandstones have coarser grain sizes and indicate shallower water depths. Additionally, the observation of reworked bivalves indicates a setting with higher water energy, typically the shoreface. Overall, shallower shoreface conditions existed SE of the central horst, whereas the central horst and NW of the central horst was characterized by deeper offshore marine conditions.

5.2.5 Tectonostratigraphic Unit 5

Observations

Tectonostratigraphic Unit 5 is bound by surface S8 at its upper boundary and surface S5 (described in section 5.2.4) at its base (Fig. 5.1). The unit is only observed in the SE part of the central horst and towards SE. For the first 630 m SE of the central horst, surface S8 separates sandstones and marls from overlying conglomerates or sandstones with clasts. From 630 m and towards the end of the study area the surface represents a boundary where conglomerates are overlain by sandstones.

The unit shows an overall increase in thickness from the central horst (ca. 12 m) and towards SE (ca. 37 m) (Fig. 5.1). Internally Tectonostratigraphic Unit 5 is composed of three stratal units (SU6, SU7 and SU8) and across-fault thickening occurs in relation to one or two of these stratal units for most of the faults exposed before the Isthmia Graben (faults FS2, FS3, FS4, FS5 and FS6).

Tectonostratigraphic Unit 5 is composed of marls, sandstones and conglomerates. In the central horst the unit is composed entirely of parallel bedded marls. These marl deposits contain marine bivalves (Collier, 1990). In the immediate hanging wall of the SE horst-bounding fault (FS1) and for the next 435 m the unit also seems to be marly, but with more input of sand (Fig. 5.1). After 435 m and further towards SE Tectonostratigraphic Unit 5 shows much more internal variations. At the top of stratal unit SU6 (surface S6) conglomerate lag is overlying parallel bedded sandstones. Similar characteristics occurs within this stratal unit and conglomerates are observed above surface S5.1 and S5.3 with parallel bedded sandstones in between. Local truncations of underlying strata are also observed in relation to surface S6 and S5.1. At the top of stratal unit SU7 (surface S7) parallel bedded sandstones are overlain by conglomerates or sandstones with clasts and shells.

Interpretations

For the first 630 m SE of the central horst surface S8 is characterized as a surface that indicates a basinward shift in facies across the surface (Fig. 5.1). This is based on the observation that conglomerates or sandstones with clasts overlie sandstones and marls. After 630 m surface S8 indicate a landward shift in facies across the surface due to the observation of sandstones overlying conglomerates or sandstones with clasts and shells.

The presence of marine bivalves within the unit indicates a marine environment (Collier, 1990). Similar to Tectonostratigraphic Unit 4, the marls are interpreted to be offshore marine deposits, while the sandstones represent shoreface deposits. Additionally, Tectonostratigraphic Unit 5 is composed of several internal surfaces that indicate basinward shifts in facies across these surfaces (S5.1, S5.3, S6 and S7) (Fig. 5.1). These basinward shifts in facies frequently occur where conglomerate lag or conglomerates are overlying parallel bedded shoreface sandstones. The conglomerate deposits are interpreted to be foreshore deposits since the coarse grain sizes represent even shallower water depths than the underlying shoreface deposits. Consequently, the unit is composed of foreshore conglomerates and shoreface sandstones furthest towards SE and offshore marls in the area around the central horst.

5.2.6 Tectonostratigraphic Unit 6

Observations

The lower boundary of Tectonostratigraphic Unit 6 is surface S8, which is described in sections 5.2.4 and 5.2.5 (Fig. 5.1). The upper boundary is not observed due to erosion of the canal surface. The unit is thickening from the NW part of the central horst and towards NW (maximum thickness of ca. 34 m). In this part of the study area Tectonostratigraphic Unit 6 is composed of several stratal units (SU9-SU13). Stratal units 9 and 10 also show thickening trends towards NW, with maximum thicknesses of ca. 13 m and ca. 15 m, respectively. Within the entire study area across-fault thickening occurs for faults FN1, FN4, FS1 and FS10.

In the NW part of the central horst Tectonostratigraphic Unit 6 is composed of three stratal units (SU9, SU10 and SU11) (Fig. 5.1). These can be traced further towards NW and from 405 to 730 m a total of six stratal units are observed (SU9-SU13). The stratal units within Tectonostratigraphic Unit 6 occur in a cyclic manner switching between cross-bedded conglomerates and parallel bedded sandstones.

Tectonostratigraphic unit 6 is eroded in the SE part of the horst, but reappears in the immediate hanging wall of the SE horst-bounding fault (FS1) (Fig. 5.1). For the first 635 m SE of the central horst the unit is composed of conglomerates and sandstones. After 635 m the unit shows internal variations where sandstone is overlain by cross-bedded conglomerate (surfaces S8.1 and S8.2).

Interpretations

The stratal units within Tectonostratigraphic Unit 6 in the NW part of the horst and towards NW were described and interpreted by Collier (1990). Thus, the conglomerates are interpreted to represent foreshore deposits, while the sandstones are shoreface deposits. The sandstone and conglomerates SE of the central horst show similar characteristics as the ones in NW and these are also interpreted to be from shoreface and foreshore environments, respectively.

6 Structural style and evolution

The aim of this chapter is to provide a detailed description and interpretation of the fault population exposed within the Corinth Canal. A structural overview is given at the start of the chapter (section 6.1), before focusing on fault geometries and characterization of fault zones (section 6.2). Further, in section 6.3, throw profiles and expansion indices are utilized to determine the relative timing and growth history of studied faults. The distribution of faults, throw and heave within the study area is addressed in section 6.4.

6.1 Structural overview of the Corinth Canal

Within the study area the main structural elements are a central horst block, several fault blocks and the Isthmia Graben (Fig. 6.1). The central horst is approximately 540 m long and is bound by a N-dipping fault, FN1, and a S-dipping fault, FS1, towards NW and SE, respectively. Faults with a maximum throw larger than 1 m are included in the study, which make a total of 23 faults. The fault spacing ranges between a minimum of approximately 10 m and a maximum of approximately 540 m. Nine studied faults are located NW of the central horst (FN1-FN6), whereas fourteen are exposed SE of the central horst (FS1-FS11). The faults have steep dips that range between 59-80° and are dipping towards N-NW or S-SSE (Fig. 6.2). The N-dipping faults are predominantly located NW of the central horst while the S-dipping faults are mainly located SE of the central horst. Most of the faults can be linked over the canal with an exception of three faults (FN1.1, FS1.1 and FS9.1) that are only exposed on the eastern canal wall.

Among the nine faults exposed NW of the central horst, only one fault, FN6, dips S. The other faults dip N-NW, with strikes ranging between 232-254° (Fig. 6.2a). Six of the faults are block-bounding faults (FN1, FN2, FN3, FN4, FN5 and FN6) and cut through the entire canal stratigraphy. The smallest of the fault blocks is approximately 50 m long, whereas the largest has a length of approximately 180 m. The remaining three faults (FN1.1, FN1.2, and FN5.1) are located within fault blocks and tip out within the exposed stratigraphy. Fault FN1.1 tips out within the siltstones of Tectonostratigraphic Unit 3, fault FN1.2 tips out within the marls of Tectonostratigraphic Unit 4 and fault FN5.1 tips out within the sandstones of Tectonostratigraphic Unit 6.
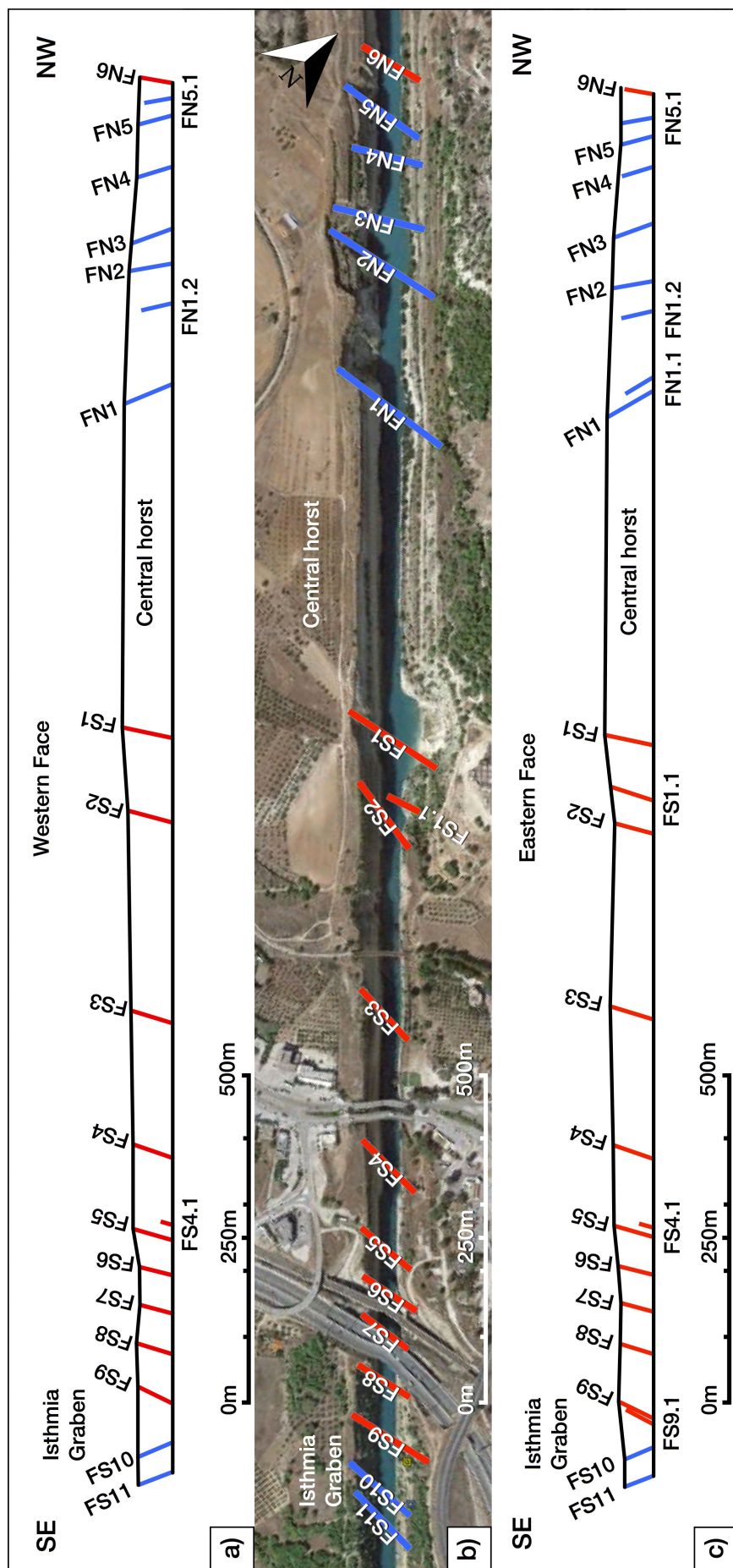
42

Figure 6.1- Cross-section of the (a) western and (c) eastern canal walls indicating the location of faults within the study area. (b) Fault map that shows faults that cut across all exposed bedding surfaces. The color of the faults represents their dip direction. Blue faults dip to N-NW while red faults dip to S-SSE. The fault names consist of two letters: FN or FS, indicating the faults position NW or SE of the central horst, respectively. Additionally, the names are differentiated by whole numbers and decimal numbers, which are increasing away from the central horst. If the fault name contains a whole number, the fault is regarded as a block-bounding fault, whereas the decimal numbers indicate a fault located within a fault block.
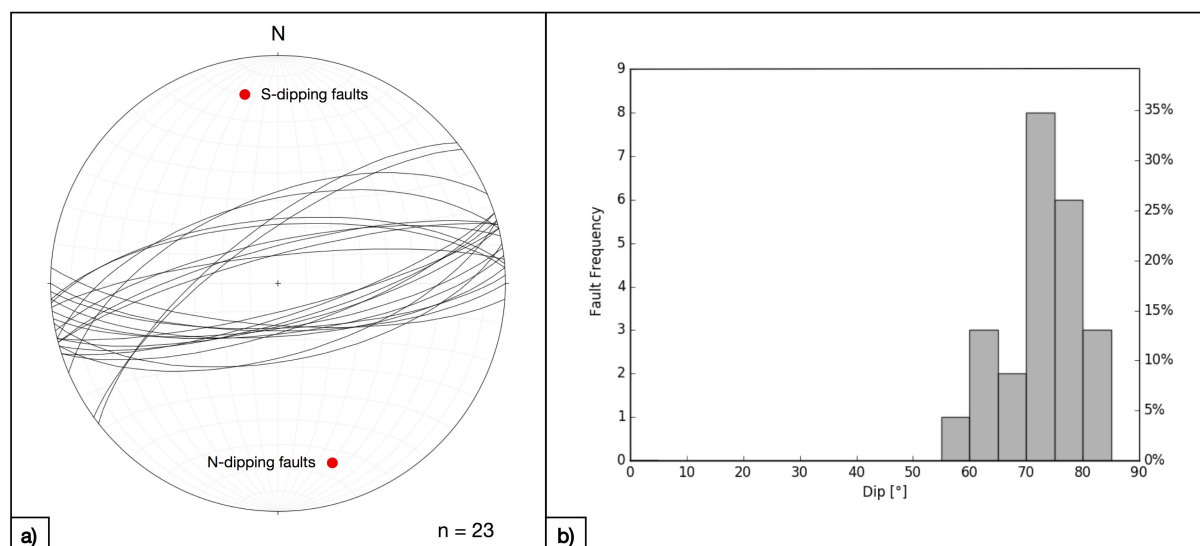
Figure 6.2 – Orientation data and dip distribution of the 23 faults exposed in the study area. (a) Stereoplot where strike and dip of each fault is indicated with great circles and the poles (red dots) indicate the average strikes and dips for the N-dipping and S-dipping faults. (b) Histogram that shows the distribution of dip. The histogram has a bin width of 5°.

Two of the fourteen faults (FS10 and FS11) located SE of the central horst dip N. The remaining faults dip towards S-SSE. Strikes range between 072-094° (Fig. 6.2a). Eleven of the faults (FS1, FS2, FS3, FS4, FS5, FS6, FS7, FS8, FS9, FS10 and FS11) are block-bounding faults and cut through all exposed stratigraphy. The smallest fault block is about 50 m long while the largest is about 300 m long. The S-dipping fault blocks are tilted in a domino fashion. Among the three faults that are located within fault blocks (FS1.1, FS4.1 and FS9.1) fault FS1.1 is the only fault that cuts through the entire canal stratigraphy. Fault FS4.1 has been eroded by surface S5.

The faults are grouped into three main groups based on their geometry: 1) planar faults, 2) listric faults and 3) vertically and laterally segmented faults. Fault group 3 is further subdivided into four subgroups based on what combination of geometries (planar, listric or vertically segmented) a fault has on the western and eastern canal wall.

Damage zones associated with the faults are generally narrow. The largest damage zone, which has a width of approximately 55 m, is observed within the Isthmia Graben in the hanging wall of fault FS10 exposed on the eastern canal wall. Splay faults and smaller scale faults are the main structural elements found in the damage zones, in addition to

local folding observed a few places. Splays are mainly located in the hanging wall of main faults, but footwall splays also occur.

6.2 Fault geometries and fault zone characterizations

Faults in the study area have planar, listric or vertically and laterally segmented geometries. Northwest of the central horst the faults that are listric or vertically and laterally segmented have a tendency to change dip at surface S8. Change in dip also occurs at surface S4. Southeast of the central horst, listric and vertically/laterally segmented faults have changes in dip at surfaces S4, S5, S6 and S7.

Damage zones in the study area frequently exhibit splay faults. Fifteen of the faults have one or more splays in their hanging wall, whereas five faults show footwall splays. Hanging wall splays have branch points at stratal surfaces or at a maximum of 4.5 m below a stratal surface, while footwall splays have branch point at or at a maximum of 4.4 m above a stratal surface. The splays are branching off the main fault at different stratigraphic levels and there is no consistency in what deposits that are found above and below the stratal surface closest to the branch point of the splays.

6.2.1 Fault groups

Planar faults

In this study a planar fault is defined as a straight fault where the dip remains constant with depth. Six of the twenty-three faults (FN1.2, FN2, FS5, FS8, FS9 and FS11) exposed in the study area have planar fault geometries on both canal walls (Fig. 6.3). Additionally, two of the faults, FN1.1 and FS9.1, which are only exposed on the eastern wall, are planar. This amounts to 35% of the studied faults having planar geometries.

Listric faults

A listric fault is defined as a curved fault where the dip decreases downwards with depth (e.g. Peacock et al., 2000). One of the twenty-three faults, FN6, exhibits a listric geometry on both canal walls (Fig. 6.3). Additionally, fault FS1.1 exposed only on the

eastern wall has a listric geometry and this also applies to the exposure of fault FS1 on the western wall. Consequently, 13% of the studied faults are listric.

Vertically and laterally segmented faults

The remaining twelve faults (FN1, FN3, FN4, FN5, FN5.1, FS2, FS3, FS4, FS4.1, FS6, FS7 and FS10), which constitute 52% of the faults, show both vertical and lateral variations in geometry (Fig. 6.3). These faults can be subdivided into four subgroups (Table 6.1): 1) faults that are planar on one wall and listric on the other wall, 2) planar on one wall and vertically segmented on the other wall, 3) listric on one wall and vertically segmented on the other wall and 4) vertically segmented on both walls, but with different amounts and orientation of segments.

Table 6.1 – Vertically and laterally segmented faults are subdivided into four subgroups. The table summarizes which faults are assigned to each subgroup and the percentage each subgroup constitutes among a total of 23 faults.

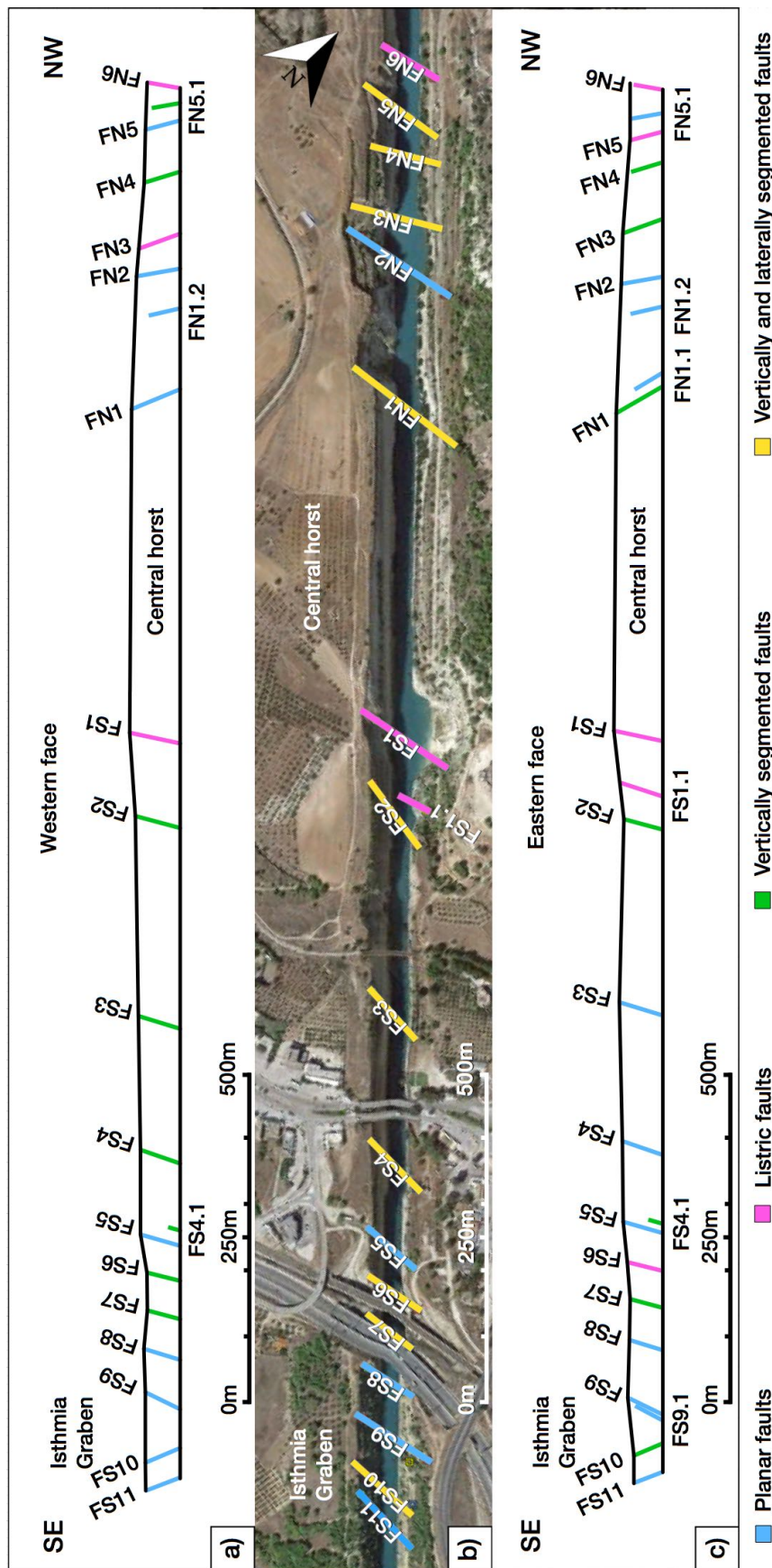| Group	Faults	Percentage
1) Planar versus listric	FN5	4%
2) Planar versus vertically segmented	FN1, FN5.1, FS3, FS4 and FS10	22%
3) Listric versus vertically segmented	FN3 and FS6	9%
4) Vertically segmented with different amounts and orientation of segments	FN4, FS2, FS4.1 and FS7	17%

Figure 6.3 – Cross-section of the (a) western and (c) eastern canal walls indicating the geometry of faults within the study area. (b) Fault map that shows fault geometry of faults that cut across all exposed bedding surfaces. The color of the faults represents their geometry. Blue faults are planar, pink faults are listric, green faults are vertically segmented and the yellow faults are vertically and laterally segmented. Note that fault FN5.1 and fault FS4.1 also are vertically and laterally segmented, but are not included in the fault map since they do not cut all exposed bedding surfaces.

6.2.2 Outcrop examples

Planar faults

The exposure of the NW horst-bounding fault, FN1, on the western canal wall is one example of a fault trace that shows a planar geometry (Fig. 6.4a). Fault FN1 has a strike of 256° and a dip of 60° towards the NNW and cuts the entire exposure from sea level to surface. The fault has a related damage zone in the form of a synthetic tip splay, which is located in its hanging wall. Additionally, strata in both the footwall and hanging wall are characterized by folding below surface S8 (Fig. 6.4c). Monocline structures are observed in the footwall and are affecting an area of approximately 200 m horizontally. Two amplitudes are recognized, one of ca. 17 m between surface S1 and S4 and another from surface S4 to S8 of ca. 4 m. In the hanging wall there is a syncline between surface S4 and S8, which has an amplitude of ca. 0.4 m and affects the hanging wall for approximately 10 m horizontally. A sedimentary wedge, which is thickening towards the fault, is also observed in the hanging wall between surface S4 and S8 (Fig. 6.4a).
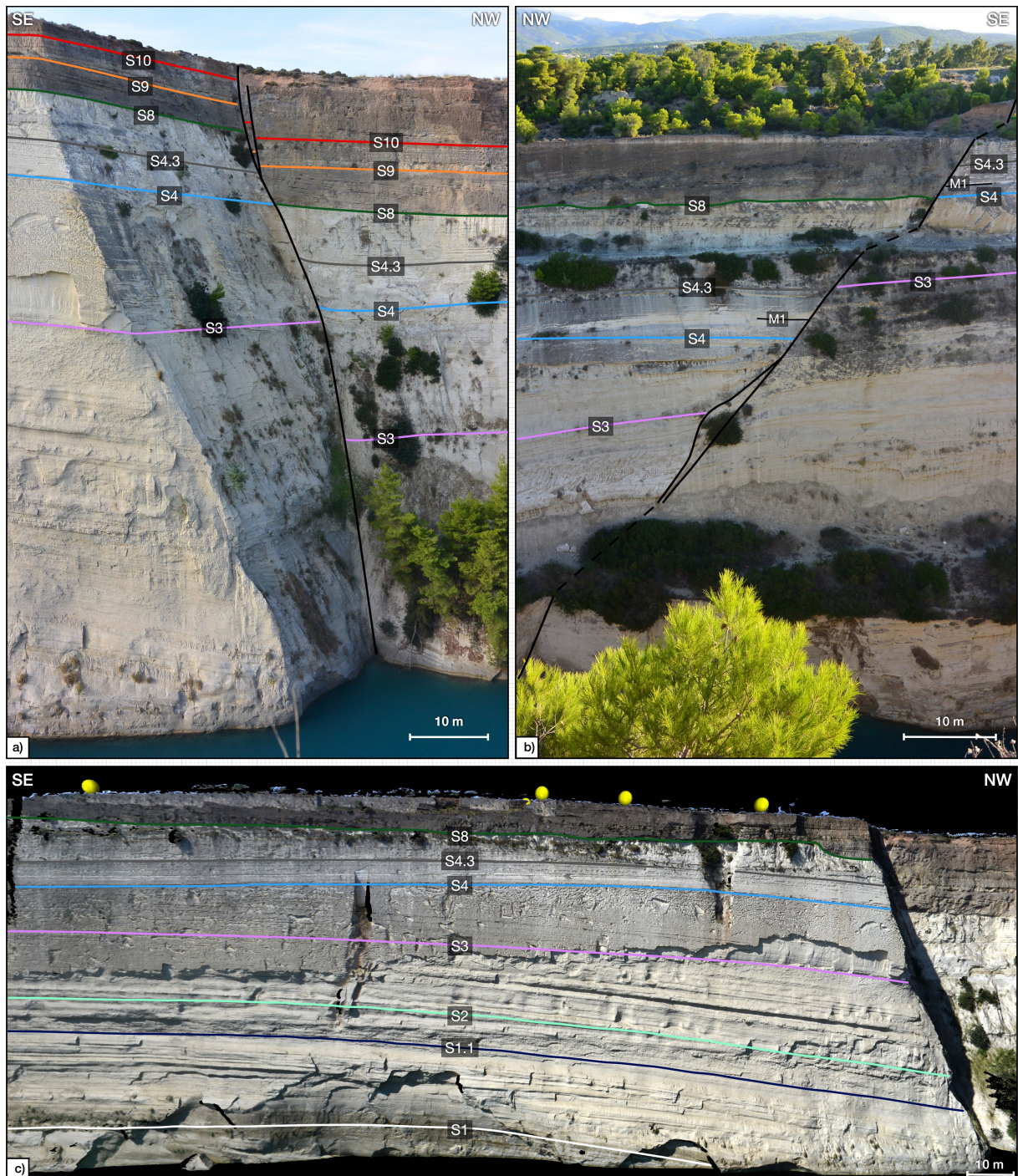
Figure 6.4 – Photo panel interpretations of fault FN1 on both the (a) western and (b) eastern canal walls indicating fault geometry and hanging wall deformation. (c) Example from the western canal wall showing the monocline structures in the central horst. The surfaces below S8 are stratal surfaces that are affected by the folding. See figure 6.3 for fault location.

Listric faults

A listric fault geometry is observed in the upper part of the SE horst-bounding fault, FS1, exposed on the western canal wall (Fig. 6.5). The lower part of this fault can be characterized as planar. Fault FS1 cuts across all exposed bedding surfaces. It has a strike at 072° and is dipping towards the SSE with a dip that decreases progressively from 88-47° in its upper listric part. The lower planar part has a dip of 78°.

Fault FS1 has associated deformation in its foot- and hanging wall (Fig. 6.5). Deformation in the footwall is characterized by a synthetic fault that tips out below surface S5, in addition to large scale folding of strata at this surface and upwards. The footwall monocline is affecting the footwall for ca. 30 m horizontally and has an amplitude of ca. 5 m. The synthetic fault located in the footwall has similar geometry as the main fault and two synthetic tip splays in its upthrown block. Deformation in the hanging wall of fault FS1 is characterized by a synthetic splay, a sedimentary wedge and large scale folding. The branch point of the splay is located at the planar lower segment of the fault and does not affect the deposits that make up the wedge. The wedge is located in the listric part of the fault; its stratigraphy exhibits thickening towards fault FS1. The hanging wall monocline stretches ca. 100 m horizontally and has the same amplitude as the footwall monocline. Additionally, the hanging wall monocline is affecting the same stratigraphic intervals as the footwall monocline.
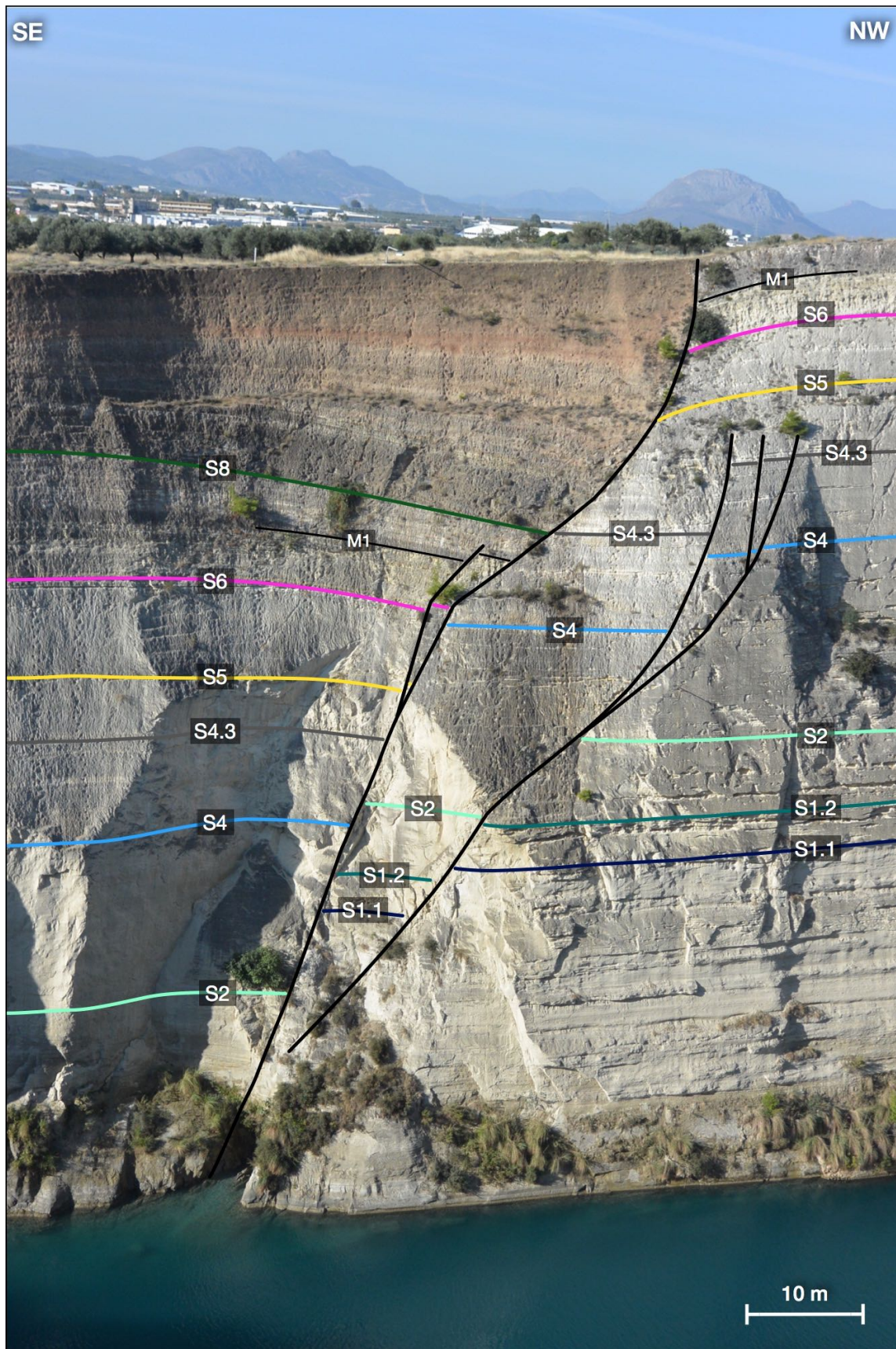
Figure 6.5 – Photo panel interpretation of fault FS1 exposed on the western canal wall. Note listric fault geometry, hanging wall and footwall deformation as well as erosion of surface S8 in the footwall. See figure 6.3 for fault location.

Vertically segmented faults

Vertically segmented faults may show a range of different geometries. In the Corinth Canal these geometries include contractional overlaps, contractional and extensional bends, hard linked structures and lenses (e.g. Childs et al., 1996, Bastesen & Braathen, 2010). The exposure of fault FS7 on the eastern wall represents an example of a contractional overlap, where the lower fault overlaps in the hanging wall of the upper fault (Fig. 6.6b). The upper fault dissects the entire stratigraphy and has an average strike of 076° and a dip of 75°. The lower fault tips out below surface S7 with a strike of 075° and a dip of 72°. Both faults are dipping towards the SSE.
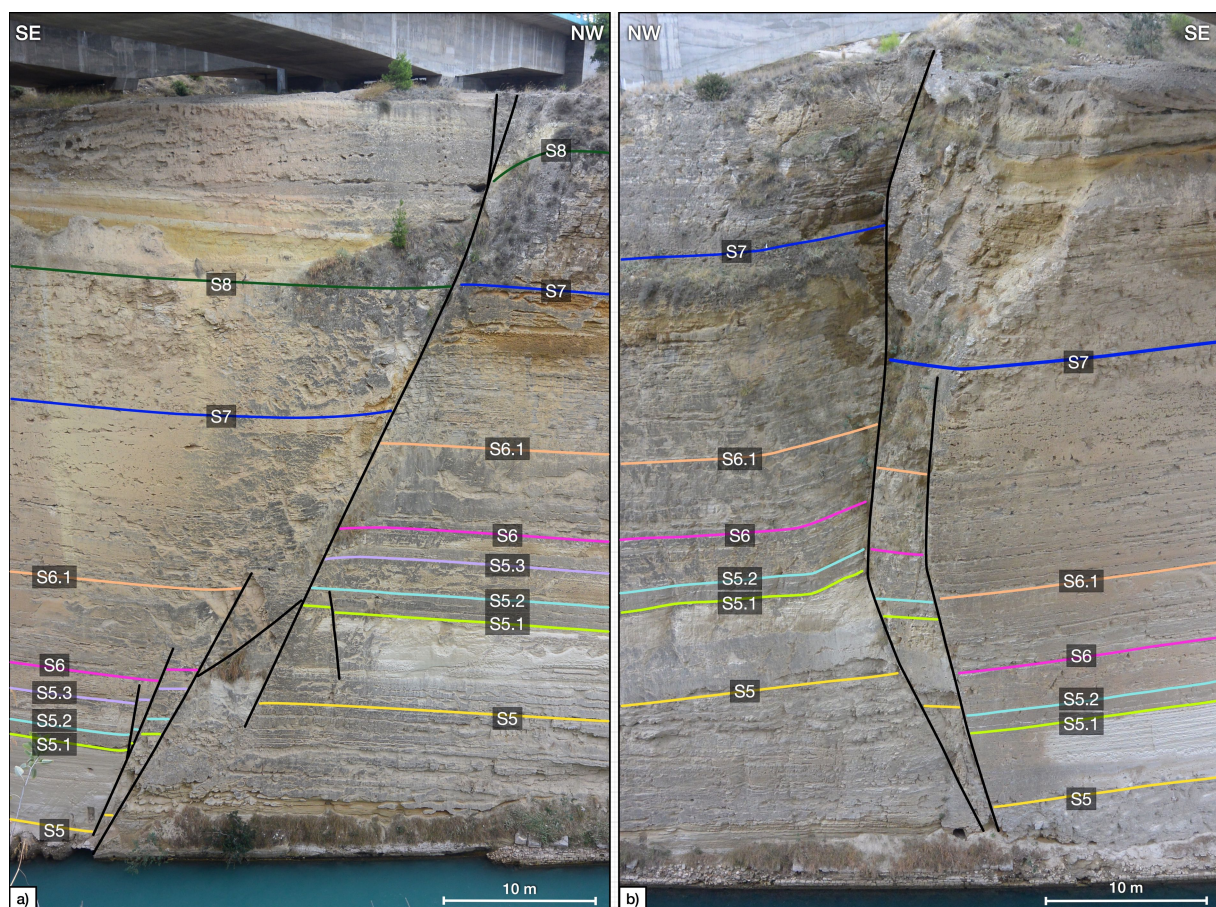

Figure 6.6 – Photo panel interpretations of fault FS7 on both the (a) western and (b) eastern canal walls indicating fault geometry, hanging wall and footwall deformation. See figure 6.3 for fault location.

The fault trace of fault FN4 exposed on the eastern wall is characterized by three contractional bends (Fig. 6.7b). This fault tips out within the sandstones above surface S9. Fault FN4 is dipping towards the NW with an average strike and dip of 234° and 73°, respectively. The footwall deformation is characterized by a synthetic fault while the deformation in the hanging wall is characterized by three synthetic splays that emerge from each of the bends, in addition to a synthetic fault.
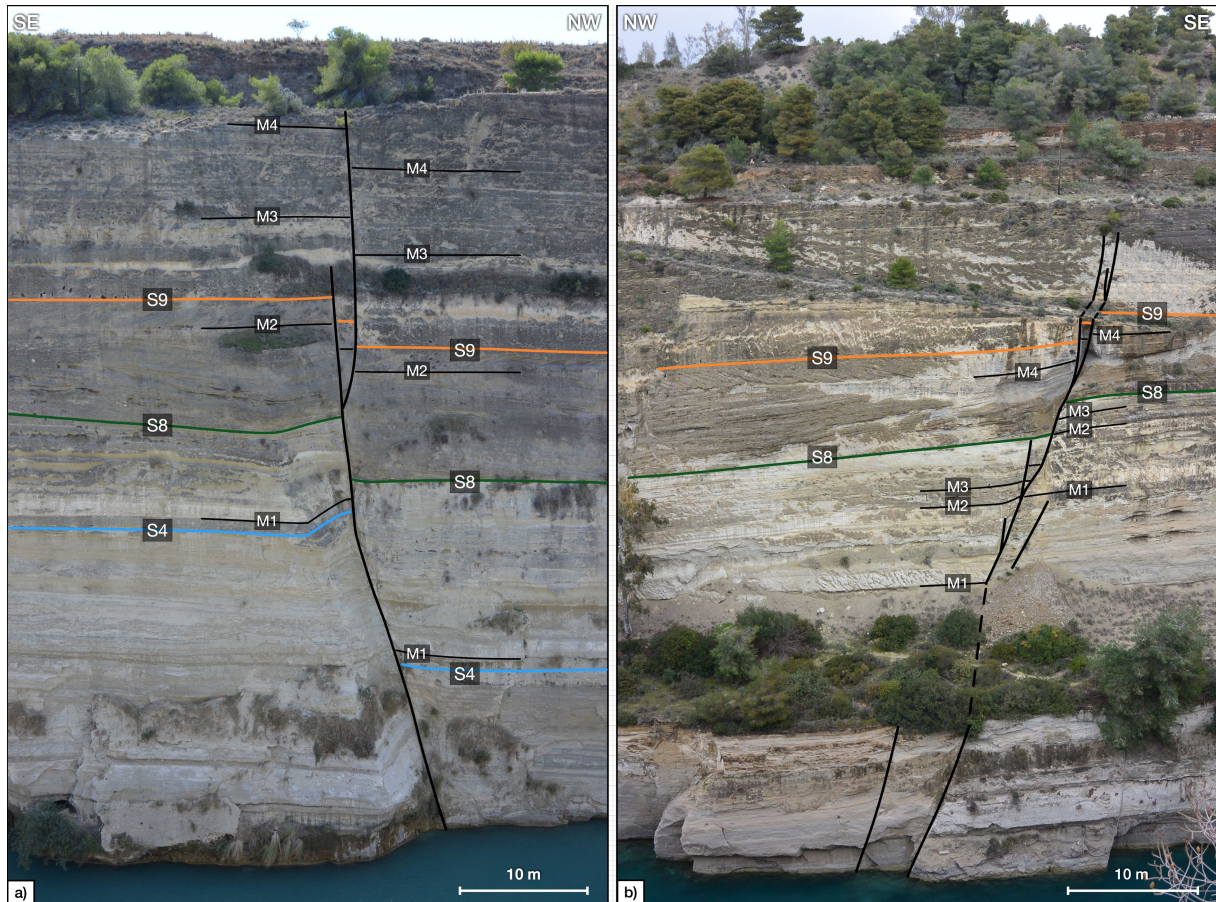

Figure 6.7 – Photo panel interpretations of fault FN4 on both the (a) western and (b) eastern canal walls indicating fault geometry, hanging wall and footwall deformation. See figure 6.3 for fault location.

An example of a fault trace that shows an extensional bend is fault FS3 on the western canal wall (Fig. 6.8a). This fault cuts across all exposed bedding surfaces and strikes at an average of 090° and dips at 73° towards the S. A damage zone is located in the hanging wall and is composed of two antithetic normal faults, one synthetic normal fault and one antithetic reverse fault. One of the antithetic normal faults exhibits one antithetic tip splay and two antithetic splays in its downthrown block.
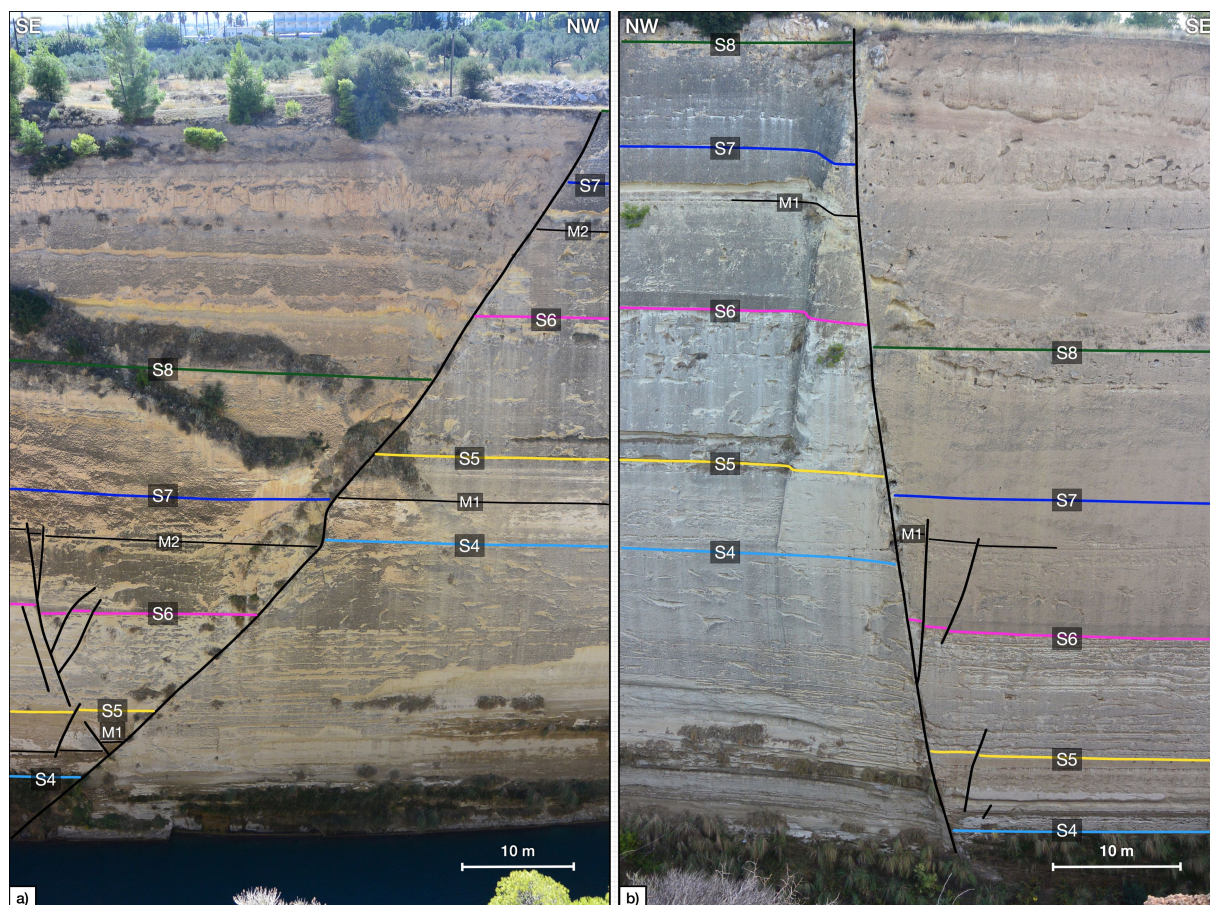

Figure 6.8 – Photo panel interpretations of fault FS3 on both the (a) western and (b) eastern canal walls indicating fault geometry and hanging wall deformation. See figure 6.3 for fault location.

The exposure of fault FN4 on the western wall is an example of a hard linked geometry (Fig. 6.7a). Two planar fault segments make up this geometry. The upper segment cuts the stratigraphy from the top of the canal and down to the conglomerates above surface S8 where it links up with the lower segment located in its footwall. The lower segment extends from the base of the outcrop and tips out within the sandstones above surface S9. Fault FS7 exposed on the western wall shows another variation of a hard linked structure (Fig. 6.6a). This fault is also composed of two planar segments, joined by a

third segment that transfers displacement between the two segments. The upper segment extends from the canal surface and tips out below surface S5, while the lower segment extends from sea level and tips out above surface S6.1. The fault has both footwall and hanging wall deformation. Footwall deformation is characterized by an antithetic fault and folding of strata at surface S8 and above (Fig. 6.6a). The footwall monocline has an amplitude of ca. 1.5 m and is affecting the footwall for approximately 6 m horizontally. Hanging wall deformation is characterized by an antithetic tip splay branching from the upper segment and a synthetic fault with a synthetic tip splay located in close proximity to the lower segment.

The fault trace of fault FN1 exposed on the eastern wall shows an example of an undeformed host rock lens (Fig. 6.4b). The lens constitutes the hanging wall damage zone. Similar to the western wall there is large scale folding of strata below surface S8 in the footwall, in addition to a sedimentary wedge between surface S4 and S8 in the hanging wall.

Conjugate faults

Conjugate faults are defined as two oppositely facing faults that cross or converge at a common intersection point or zone (e.g. Nicol et al., 1995). An example of a conjugate set is fault FN3 exposed on the western canal wall. The N-dipping fault has an average strike of 232° and a dip of 70° towards the NW, whereas the S-dipping fault is dipping towards the SSE with an average strike and dip of 077° and 73°, respectively (Fig. 6.9a). The S-dipping fault tips out within the sandstones above surface S9 and is offset by the N-dipping fault that dissects all exposed bedding surfaces. A synthetic splay and tip splay constitute the hanging wall damage zone of the N-dipping fault. The S-dipping fault has a footwall damage zone with a synthetic splay and an antithetic fault that abuts at the main fault.
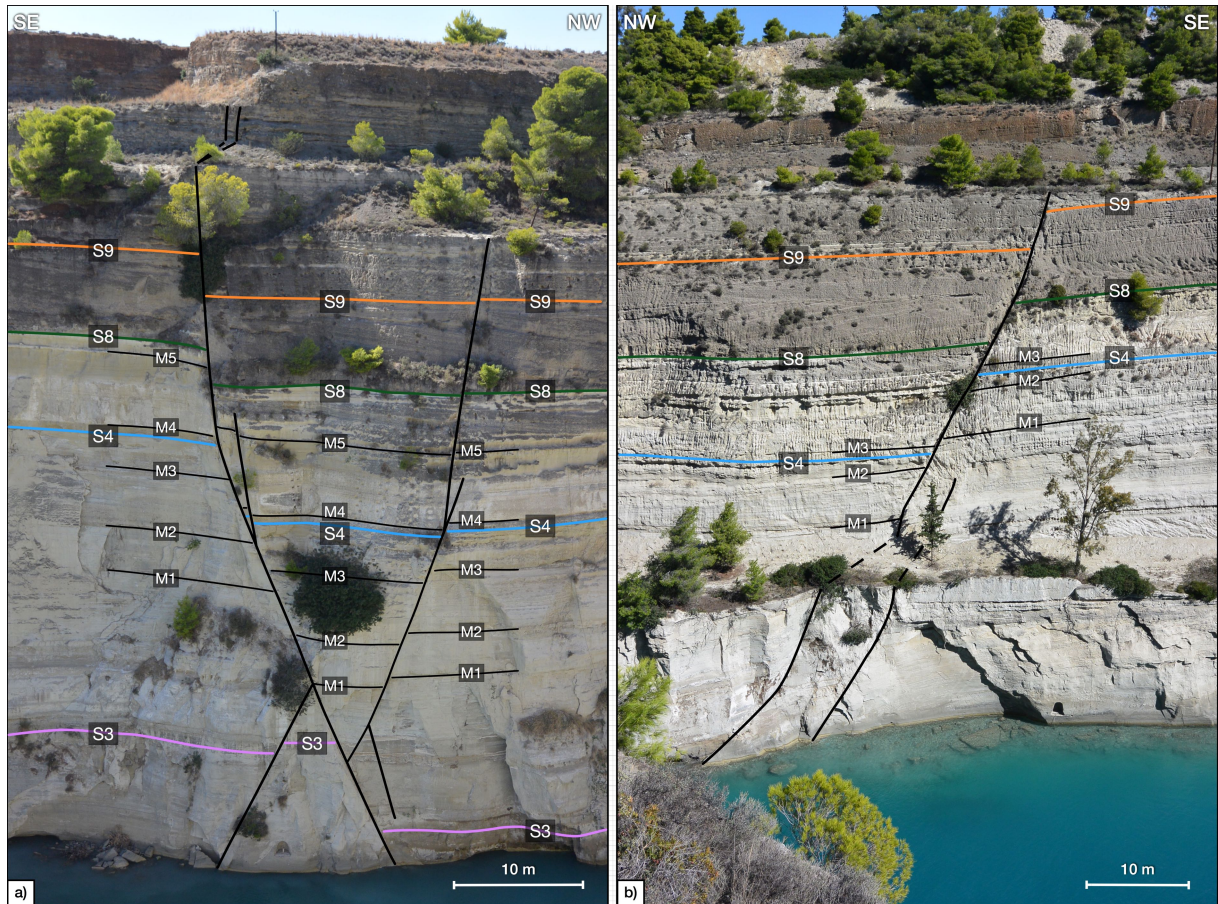
Figure 6.9 – Photo panel interpretations of fault FN3 on both the (a) western and (b) eastern canal walls indicating fault geometry, hanging wall and footwall deformation. See figure 6.3 for fault location.

6.3 Throw-depth (T-z) plots and expansion indices

The throw profiles within the study area do not show a throw distribution typical for an ideal isolated fault, which is characterized by a progressive decrease in throw from the point of maximum throw located in the center of the fault towards zero at the fault tips (e.g. Barnett et al., 1987, Baudon, 2007). The T-z plots have positive throw gradients and generally show decrease in throw upwards in the stratigraphy. The upper fault tip is exposed for some of the main faults, while the lower fault tips are not exposed for any of the main faults. These observations indicate that the throw profiles are from the up-dip tip and damage zones of the studied normal faults. The fact that most faults show an overall decrease in the throw upwards in the stratigraphy probably suggests that they all have nucleated below sea level (i.e. nucleated at depth).

Since the exposed faults are assumed to only correspond to their up-dip tips it is hard to distinguish their overall shapes based on the terminology by Baudon (2007), as one does not know how the throw is distributed below sea level (Fig. 4.3). The overall shapes of the T-z plots in this study therefore represent the up-dip tip of these normal faults and are described as either straight, convex, concave or step-like (Fig. 6.10). A straight throw profile represents a fault that has constant throw at all measured stratigraphic intervals. Convex and concave throw profiles are observed where an upwards decrease in throw occurs over several measured stratigraphic intervals in a nonlinear manner. The convex throw profiles show a large decrease in throw at lower stratigraphic intervals with smaller changes in throw up-dip, whereas the concave throw profiles have large throw changes at higher stratigraphic intervals and small changes down-dip. Step-like throw profiles are characterized by one or several intervals where up-dip decreases in throw occur in a linear manner, separated by intervals of constant throw.
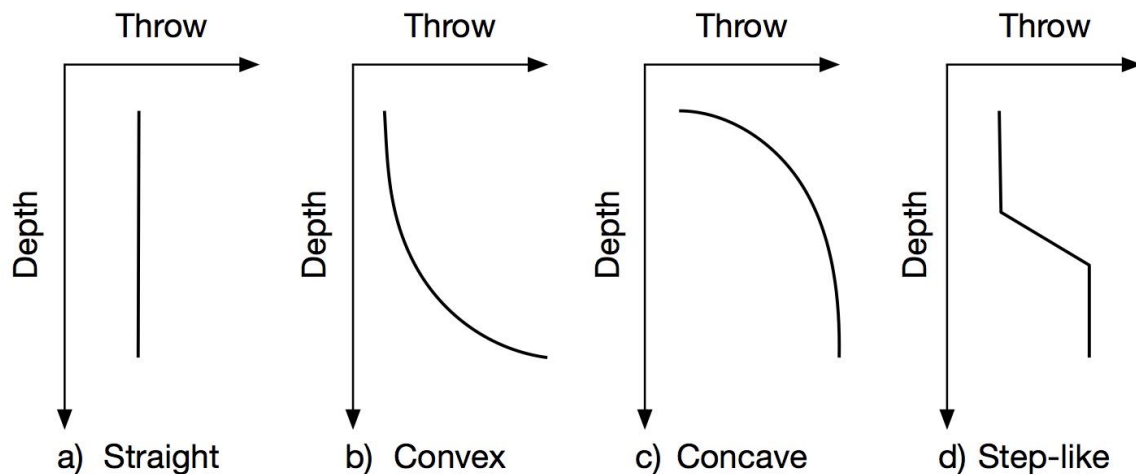
Fig. 6.10 – Schematic illustration of different styles of T-z plots and the terminology utilized in the study: (a) straight, (b) convex, (c) concave and (d) step-like.

6.3.1 Faults NW of the central horst

Observations

Northwest of the central horst the overall form of the throw profiles varies between convex, concave, straight and step-like, with throw commonly decreasing upwards in the stratigraphy (Fig. 6.11). A step-like throw profile is characteristic for most of the faults NW of the central horst (FN1.1, FN1.2, FN4, FN5.1 and FN6). These have one or several intervals where the throw is approximately constant before the throw decreases for intervals upwards in the stratigraphy. The convex (FN1) and concave (FN3) throw profiles are similar to the step-like profiles since they also show one or several intervals where throw is more or less constant and intervals where throw decreases upwards in the stratigraphy. It is within the stratigraphic intervals where throw is decreasing upwards that the throw profiles become either convex or concave. Faults FN2 and FN5 have straight T-z plots with constant throw at all stratigraphic intervals.

The throw profiles that do not have constant throw at all stratigraphic intervals show variability. However, some general characteristics are seen for faults FN1, FN3, FN4 and FN6 (Fig. 6.11b, f, h, l). From surface S4 (S4.3 for fault FN6) to S8 the throws decrease between 1.0 m to 5.6 m. The corresponding throw gradients range between 0.10 and 1.24 and the expansion indices are > 1.00 (between 1.11 and 2.50). A growth wedge, which is located in the hanging wall of fault FN1, is observed within the stratigraphic interval bound by surface S4 and S8 (Fig. 6.4). Additionally, monocline structures are

observed in the footwall of fault FN1. The monoclines below surface S4 have higher amplitudes (ca. 17 m) than the monocline above S4 (ca. 4 m).

Considerable changes in throw and expansion index above surface S8 are only observed for faults FN1 and FN4 (Fig. 6.11b, h). Both faults show decreases in throw from surface S8 to the next stratal surface (S9) or marker (M4), respectively. Within these stratigraphic intervals the throws decrease from 13.7 m to 10.4 m for fault FN1 and from 3.3 m to 2.7 m for fault FN4. The corresponding throw gradients are 0.25 and 0.08, while the expansion indices are 1.33 and 1.11, for faults FN1 and FN4, respectively. Fault FN1 has conglomerates with subparallel bedding above S8 in the footwall and cross-bedded conglomerates above S8 in the hanging wall. The throw profile of fault FN1 continues to show a decrease in throw value between surface S9 and S10. In this interval throw decreases from 8.9 m to 8.2 m with a throw gradient of 0.20 and an expansion index of 1.27. Moreover, fault FN4 has constant throw and an expansion index close to 1.00 from M4 to S9 before it terminates above S9 (throw gradient = 0.32 and expansion index = 1.37).

Faults FN1.1 and FN1.2 show progressive decrease in throw up-dip from surface S3 and S4, respectively (Fig. 6.11c, d). The throw for fault FN1.1 decreases from 3.7 m at surface S3 to 0 m at the fault tip just below S4. The corresponding throw gradients are between 0.20 and 0.29 and the expansion index is 1.27. Fault FN1.2 shows a decrease in throw from 2.3 m at S4 to 0 m where it tips out below S8. Throw gradients in this stratigraphic interval are between 0.26 and 0.30 with expansion indices of 1.29 and 1.37, for faults FN1.1 and FN1.2, respectively. Lower in the stratigraphy both faults have intervals of constant throw with expansion indices close to 1.00. Additionally, FN1.2 shows a decrease in throw with a throw gradient of 0.05 between S3 and an overlying marker (M1). The expansion index is close to 1.00 at this interval as well.

Some of the faults shown in figure 6.11 (FN1, FN3, FN4, FN5 and FN6) have throws that are distributed between the main fault and one or several splays. Most of the faults have splays that take up some of the throw, whereas for fault FN5 the throw is distributed between the main fault and the splays producing a cumulative throw profile that is approximately constant (Fig. 6.11j).
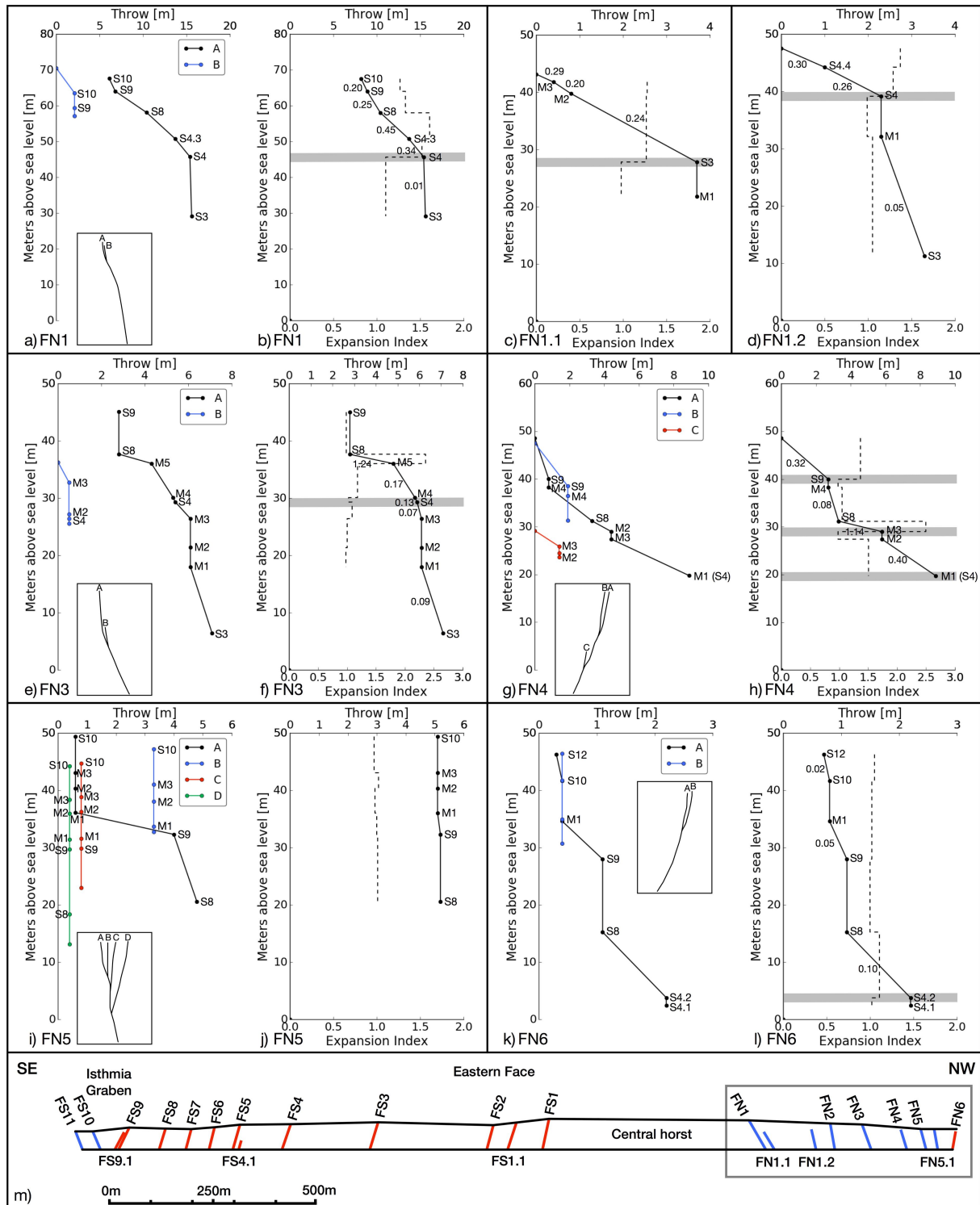
Figure 6.11 – Throw-depth (T-z) plots with throw gradients and expansion indices of faults NW of the central horst. (a, e, g, i, k) T-z plots of faults FN1, FN3, FN4, FN5 and FN6 and their splays. (b, c, d, f, h, j, l) T-z plots of total throw, including splays when present, with throw gradients and expansion indices. Expansion indices are marked by dashed lines. Gray line indicates where the faults were surface breaching. The legends and figure in a, e, g, i and k indicate the main fault (A) and splays (B, C and D). (m) Cross-section of study area indicating the location of the faults (gray box).

Interpretations

Post-sedimentary faults form after the deposition of sediments and grow by blind propagation of the fault tips (e.g. Hongxing & Anderson, 2007). Such faults are characterized by having throw profiles with constant or very small changes in throw, no or low throw gradients and no expansion (i.e. expansion indices around 1.00). Three of the faults (FN2, FN5 and FN5.1) NW of the central horst show these characteristics at all measured stratigraphic intervals (Fig. 6.11j). This implies that fault FN2 grew by blind fault propagation between surface S3 and S10, fault FN5 grew by blind fault propagation between surface S8 and S10 and fault FN5.1 grew by blind fault propagation in its latest stages of growth (between surface S4.2 until it tips out just below S10).

Syn-sedimentary growth faults intersect the free surface and are active during deposition of sediments (e.g. Thorsen, 1963, Cartwright et al., 1998). They are characterized by throw profiles that show increase in throw with depth, high throw gradients and across-fault thickening of strata (i.e. expansion indices > 1.00). Northwest of the central horst faults FN1, FN1.1, FN1.2, FN3, FN4 and FN6 show intervals with these characteristics. Hence, these faults have been surface breaching growth faults at one or several stages during their growth history (Fig. 6.11b, c, d, f, h, l). Five of these faults (FN1, FN1.1, FN1.2, FN3 and FN6) show no or low throw gradients and no considerable across-fault thickening of strata at lower stratigraphic intervals. This implies that these faults first grew by blind propagation of the fault tips before they breached the free surface and became growth faults. An additional evidence for blind fault propagation of fault FN1 are the monocline structures observed below surface S4 (Fig. 6.4) (e.g. Gawthorpe & Leeder, 2000). Fault FN1.1 breached the free surface at S3, whereas faults FN1, FN1.2 and FN3 became surface breaching at S4 and fault FN6 at S4.2. Additional evidences that fault FN1 became surface breaching at S4 are that the monocline structure that starts at surface S4 in the footwall of fault FN1 has a much lower amplitude than the underlying monoclines (ca. 4 m versus ca. 17 m) and that a syncline and a growth wedge start developing in the hanging wall of fault FN1 at S4, which becomes truncated by surface S8 (Fig. 6.4) (e.g. Gawthorpe et al., 1997).

Faults FN1, FN1.1 and FN1.2 are characterized by up-dip decreases in throw, high throw gradients and across-fault thickening of strata at all stratigraphic intervals above their

respective breach surfaces (S3 for fault FN1.1; S4 for faults FN1 and FN1.2) (Fig. 6.11b, c, d). This implies that all of these faults grew as syn-sedimentary growth faults during the stratigraphic interval constrained by the outcrop (between S4 and S10 for fault FN1) or in their most recent stages of growth. Further evidence that fault FN1 was surface breaching at S8 is the observation that conglomerates in the footwall have subparallel bedding, whereas the equivalent conglomerates in the hanging wall are cross-bedded.

Faults FN3 and FN6 become buried/inactive at surface S8 based on no or small changes in throw, low throw gradients and expansion indices close to 1.00 (Fig. 6.11f, l) (e.g. Osagiede et al., 2014). However, the intervals where fault FN6 has very low throw gradients above S8 could also represent blind fault propagation. Since the throw is small at these intervals, this might just be reflecting error ranges of the measurements.

The throw profile of fault FN4 shows three intervals with up-dip decreases in throw, high throw gradients and across-fault thickening of strata. These intervals are separated by two intervals where throw is constant and there is no expansion of hanging wall strata (Fig. 6.11h). These observations indicate polycyclic growth (e.g. Cartwright et al., 1998, Osagiede et al., 2014), implying that the fault experienced at least three periods of growth at the free surface punctuated by two periods when the fault became inactive and buried. The fault was a surface breaching growth fault in its final stages of growth.

6.3.2 Faults SE of the central horst

Observations

Convex, step-like and straight throw profiles are observed SE of the central horst (faults FS1-FS7), before the Isthmia Graben (Fig. 6.12). Throw generally increases downwards in the stratigraphy for most faults. Step-like throw profiles (FS2, FS3, FS4, FS4.1, FS5) with intervals that have approximately constant throw followed by a decrease in throw up-dip of the fault are most common. A similar form is observed for fault FS6, however, the decrease in throw occurs over two stratigraphic intervals resulting in a convex shape. The remaining three faults (FS1, FS1.1 and FS7) have T-z plots with approximately constant throw at all stratigraphic intervals.

The faults that have a step-like throw profile show one (FS2, FS3 and FS5) or two (FS4 and FS4.1) intervals where throw is decreasing upwards in the stratigraphy (Fig. 6.12c, d, f, g). Faults FS2, FS3 and FS5 have one interval where throw is decreasing up-dip and this is occurring at surfaces S5, S7 and S6, respectively. The decrease in throw is between 2 and 3 m for all three faults and the throw gradients are between 0.13 and 0.40. Decreases in throw coincides with increases in expansion indices and faults FS2, FS3 and FS5 have expansion indices of 1.10 from S5 to M3, 1.61 from S7 to S8 and 1.14 from S6 to S8, respectively. Faults FS2 and FS5 have approximately constant throw and expansion indices close to 1.00 above and below the stratigraphic interval that have decreases in throw and increases in expansion. Fault FS3 also has a similar trend, only that the throw decrease and expansion increase occurs at the top of the outcrop. Fault FS4 has two intervals where throw is decreasing, which is between surfaces S4 and S5 and between surface S7 and marker M1. The decrease in throw is approximately 4 m between S4 and S5 (throw gradient = 0.49) and approximately 2 m between S7 and M1 (throw gradient = 0.24). Increased expansion indices of 1.68 and 1.24, for S4 to S5 and S7 to M1, respectively, coincide with decreases in throw for fault FS4. The interval between S5 and S7 has an approximately constant throw with expansion indices close to 1.00, which is also the case from marker M1 and upwards.

Fault FS6 has a concave cumulative throw profile (Fig. 6.12i). There is an interval where throw is decreasing (S5.2 to S7) between intervals with constant throws and expansion indices around 1.00. From surface S5.2 to S6 throw is decreasing by approximately 3 m with a throw gradient of 0.79 and an expansion index of 1.60. Between surface S6 and S7 the throw is decreasing by approximately 2 m with a throw gradient of 0.14 and an expansion index of 1.14.

Among the faults shown in figure 6.12, faults FS1, FS4, FS6 and FS7 have throws that are distributed between the main fault and one or several splays and/or a hanging wall or a footwall fault. Faults FS4 and FS6 both have two splays that take up some of the throw. Faults FS1 and FS7 have a footwall and a hanging wall fault, respectively, and throw is distributed between them. The cumulative throw profiles of these faults become straight. Fault FS1 has a monocline structure both in the hanging wall and the footwall

from surface S5 and upwards (Fig. 6.5). Additionally, a hanging wall wedge, which is thickening towards the fault FS1, is observed from S8 and upwards.
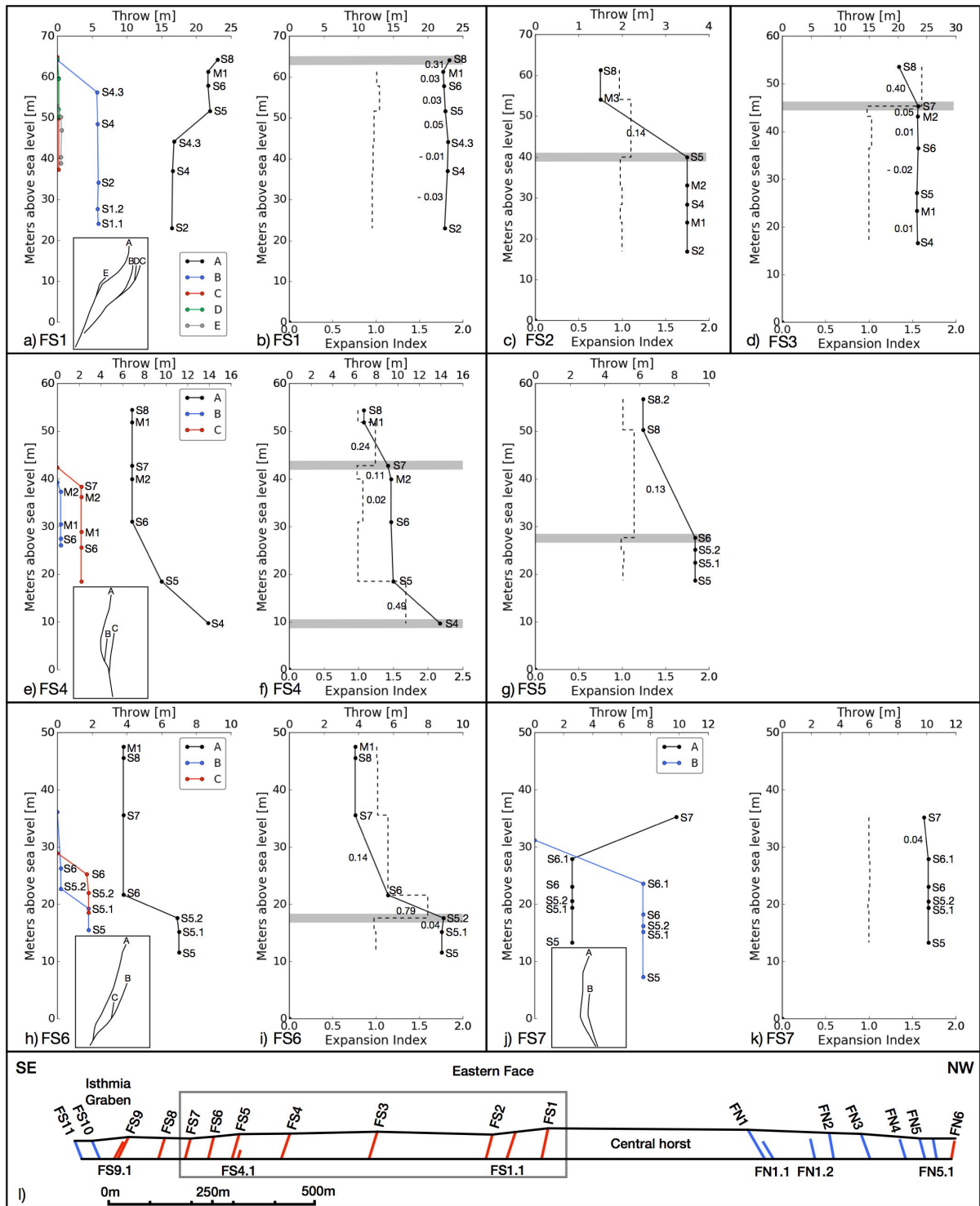

Figure 6.12 – Throw-depth (T-z) plots with throw gradients and expansion indices of faults SE of the central horst before the Isthmia Graben. (a, e, h, j) T-z plots of faults FS1, FS4, FS6 and FN7 and their splays, hanging wall fault or footwall faults. (b, c, d, f, g, i, k) T-z plots of total throw, including splays, hanging wall and footwall faults when present, with throw gradients and expansion indices. Expansion indices are marked by dashed lines. Gray line indicates where the faults were surface breaching. The

legends and figures in a, e, h and j indicate the main fault (A) and splays, hanging wall fault or footwall fault (B, C, D and E). (m) Cross-section of study area indicating the location of the faults (gray box).

Interpretations

Southeast of the central horst, before the Isthmia Graben, three faults (FS1, FS1.1 and FS7) have characteristics that match post-sedimentary blind faults with approximately constant throw, low throw gradients and expansion indices close to 1.00 at all measured stratigraphic intervals (e.g. Hongxing & Anderson, 2007) (Fig. 6.12b, k). Thus, fault FS1.1 grew as a blind fault from a marker below surface S4 to surface S5, whereas fault FS7 propagated as a blind fault from surface S5 to surface S7. In regards to fault FS7, the growth was distributed between the main fault and a hanging wall fault from surface S5 to S6.1. After stratal level S6.1 the hanging wall fault terminated and the growth of the fault was localized onto the main fault. A similar growth history characterizes fault FS1. This fault grew as a blind fault at least from surface S2 to marker M1. Additional evidence for blind fault propagation are the monocline structures observed from surface S5 to S8 both in the foot- and hanging wall of fault FS1 (Fig. 6.5) (e.g. Gawthorpe & Leeder, 2000). The growth was distributed between the main fault and the footwall fault at least from surface S2 to S4.3. After surface S4.3 the footwall fault terminated and growth was localized onto the main fault. The observation of a growth wedge that starts developing at surface S8 in the hanging wall of fault FS1 suggests the fault became a surface breaching growth fault at that time (Fig. 6.5) (e.g. Gawthorpe et al., 1997). This is not evident from the T-z plot since surface S8 becomes eroded in the footwall of FS1.

Faults FS2, FS3, FS4, FS4.1, FS5 and FS6 show one or two intervals with up-dip decrease in throw, high throw gradients and across-fault thickening of strata, implying that these faults have been surface breaching growth faults at least one or two times during their growth history (Fig. 6.12c, d, f, g, i) (e.g. Thorsen, 1963, Cartwright et al., 1998). Most of these faults (FS2, FS3, FS5 and FS6) are characterized by having constant throw and no expansion of hanging wall strata at lower stratigraphic intervals, indicating that these faults first propagated as blind faults before they breached the surface and became growth faults. Faults FS2, FS3, FS5 and FS6 all breached the surface at different times: at surface S5, S7, S6 and S52, respectively. Additionally, the throw profiles of faults FS2, FS5 and FS6 have constant throw above the stratigraphic interval(s) where up-dip

decrease in throw occurs. The corresponding expansion indices are close to 1.00, which suggests a time of inactivity and burial of the upper fault tips (e.g. Osagiede et al., 2014).

Fault FS4 shows evidence of polycyclic growth, which is based on the observation of two intervals where throw decrease upwards and across-fault thickening occurs (from surface S4 to S5 and from surface S7 to marker M1) separated by stratigraphic intervals where throw is constant and no thickening occurs (Fig. 6.12f) (e.g. Cartwright et al., 1998, Osagiede et al., 2014). The intervals with constant throw and no thickening represents times when the fault was inactive and its upper fault tip was buried.

6.3.3 Isthmia Graben

Observations

The throw profiles of faults within Isthmia Graben are either step-like or straight with throw generally decreasing upwards in the stratigraphy. Figure 6.13 shows the throw profile of fault FS10 and the throw profiles of its hanging wall splays. These throw profiles have one to three intervals where throw decreases upwards in the stratigraphy, except for splay E that has a constant throw profile. The expansion index of splay E is close to 1.00 at all stratigraphic intervals. The main fault shows a decrease in throw of about 0.6 m from I1 to S8, whereas all the splays have constant throws for the same interval. Within the interval between I1 and S8 the expansion index of the main fault is 1.23 and the expansion indices for the splays are close to 1.00. The main fault and splays B and D show decreases in throw (between 0.4 and 2 m) from surface S8 to I3, with throw gradients between 0.04 and 0.55. The expansion indices within this interval are between 1.09 and 1.75. From I3 to I4 the main fault and majority of its splays (splay B the exception) have approximately constant throws. The expansion indices in this interval are close to 1.00 for all faults, including splay B. In the interval between I4 to I5 splay C and D show decrease in throw by 0.5 m and 1 m, respectively. The corresponding throw gradients are 0.15 and 0.21 with expansion indices of 1.19 and 1.35.
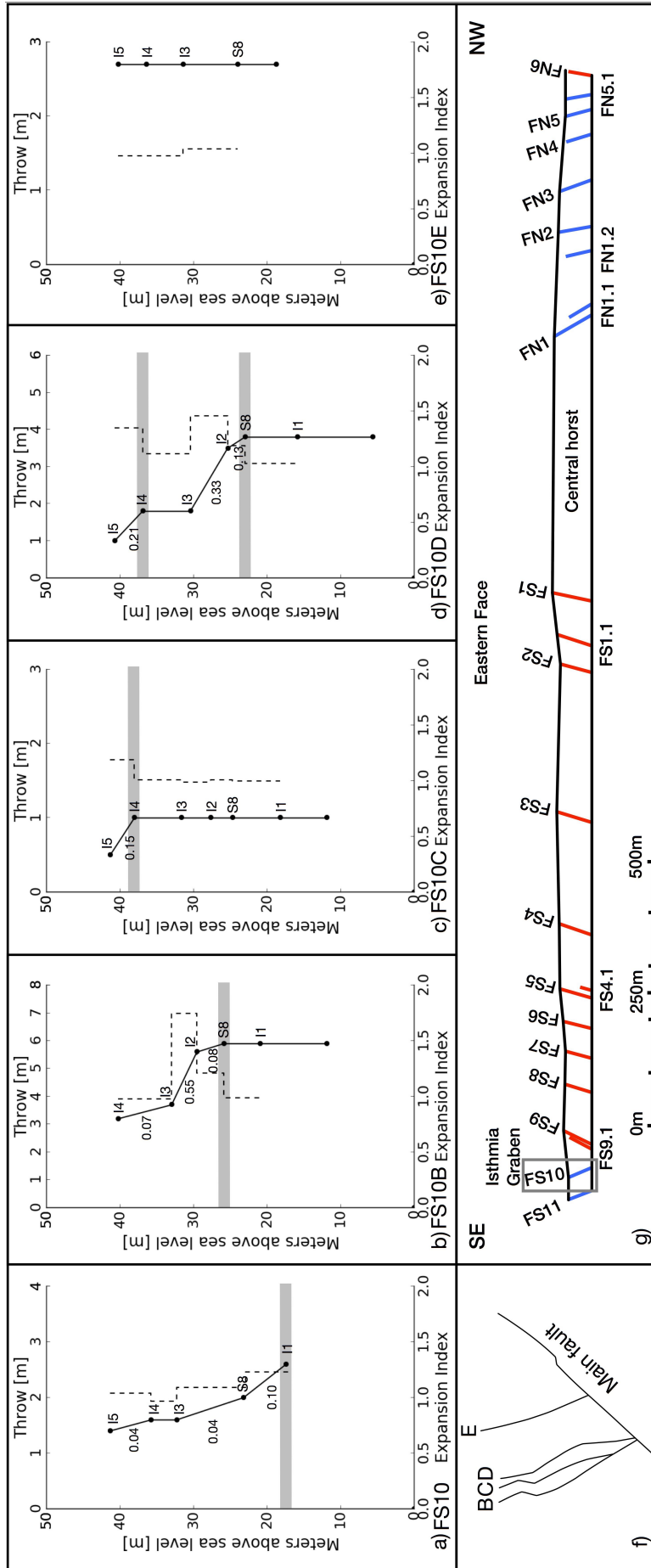
Figure 6.13 – (a-e) Throw-depth (T-z) plots with throw gradients and expansion indices of fault FS10 and its hanging wall splays located within the Isthmia Graben. Expansion indices are marked by dashed lines. Gray line indicates where the main fault and the splays were surface breaching. (f) Fault geometry of fault FS10. (g) Cross-section of study area indicating the location of fault FS10 (gray box).

Interpretations

Splay E has characteristics that match a post-sedimentary blind fault with very small changes in throw, low throw gradients and no across-fault thickening of strata (e.g. Hongxing & Anderson, 2007) (Fig. 6.13e). All the other splays show these characteristics at stratal levels below surface S8, indicating fault growth by blind propagation (Fig. 6.13b, c, d).

From I1 to S8 the throw profile of the main fault (FS10) is characterized by an up-dip decrease in throw and a high throw gradient (Fig. 6.13a). This coincides with across-fault thickening of strata and the fault can therefore be characterized as a syn-sedimentary growth fault in the interval between surface I1 and S8 (e.g. Thorsen, 1963, Cartwright et al., 1998). From S8 to I5 the main fault is characterized by two intervals (S8 to I3 and I4 to I5) that show small changes in throw and corresponding low throw gradients. No major across-fault thickening is occurring and the fault has probably grown by blind propagation within these intervals. However, between surface S8 and I3 the expansion index is still close to 1 (1.09), but due to the small throw of this fault it is hard to determine whether the fault actually grew by blind propagation or if it was a syn-sedimentary growth fault experiencing high sediment accumulation rates (Childs et al., 2003).

Splays B and D are characterized by up-dip decreases in throw, high throw gradients and across-fault thickening between S8 and I3, implying that the splays were syn-sedimentary growth faults in this interval (Fig. 6.13b, d). The main fault and the splays seem to become buried at surface I3 based on no or small changes in throw, low throw gradients and no considerable expansion of hanging wall strata in the interval between I3 and I4 (e.g. Osagiede et al., 2014). Since the main fault and splay D show constant throw in this interval they were probably inactive from I3 to I4, whereas splay B propagated as a blind fault in this interval. Splays C and D show decreases in throw from I4 to I5, have high throw gradients associated with across-fault thickening of strata, indicating that these faults were active and surface breaching in this time period (Fig. 6.13c, d).

6.4 Distribution of faults, throw and heave at surface S8

Surface S8 is the only surface that can be traced throughout the study area. Figure 6.14 shows the cumulative distributions of fault frequency, throw and heave at this stratigraphic level along a transect perpendicular to the average strike of the faults. The transect starts in SSE at fault FS11 and ends in the NNW at fault FN6 with a total length of approximately 1.7 km. Fault splays and minor faults that displace surface S8 are also included in the plots, which makes a total of 28 faults (Fig. 6.14a). Total throw and heave along the transect are 163.9 m and 51.7 m, respectively, and the extension is 3% (Fig. 6.14b, c). The plots can be used to determine the heterogeneity, V, of the data distributions based on the deviation from a uniform distribution (Putz-Perrier & Sanderson, 2008a, 2008b). The results from these plots show a V_f-value of 0.46, a V_t-value of 0.35 and a V_h-value of 0.40 implying a moderate heterogeneity.

The same cumulative distribution plots are shown in figure 6.15 only with the middle of the central horst as datum moving towards NNW or SSE. Ten faults are located NW of the central horst, whereas eighteen faults are located SE of the central horst (Fig. 6.15a, b). The distribution of faults are very similar both NW and SE of the central horst with V_f-values of 0.49 and 0.44, respectively. This indicates a moderate heterogeneity and is comparable to the overall distribution of faults within the study area (Fig. 6.14a). Total throw is 26.6 m NW of the central horst, with 25.2 m accommodated by N-dipping faults. Southeast of the central horst the total throw is 137.3 m and 112.2 m is accommodated by S-dipping faults (Fig. 6.15c, d). The V_t-values NW and SE of the central horst are 0.39 and 0.32, respectively, which indicate moderate heterogeneity. These V_t-values are similar to the overall distribution of throw in the canal section (Fig. 6.14b). Total heave accommodated NW of the central horst is 7.4 m, while the total heave accommodated SE of the central horst is 44.2 m (Fig. 6.15e, f). The corresponding V_h-values are 0.52 and 0.46, respectively, and imply moderate to high heterogeneity. The faults NW of the central horst accommodates 1% extension, whereas the faults SE of the central horst accommodates 4% extension.

The horst-bounding faults, FN1 and FS1, both accommodates most of the heave (ca. 52% and ca. 20%) NW and SE of the central horst, respectively (Fig. 6.15c, d, e, f). The V_h-values NW and SE of the central horst show no considerable difference. However, the faults NW of the central horst have slightly higher V_h-values and compared to the overall distribution of heave within the canal section the heterogeneity is higher (Fig. 6.14c). This is probably related to the fact that deformation is localized onto the NW horst-bounding fault (e.g. Nixon et al., 2014). That the faults SE of the central horst have a V_h-value that is similar to the overall distribution of heave in the study area suggest that heave is distributed between several larger faults, which can be seen from the cumulative plots (Fig. 6.14c and 6.15e).
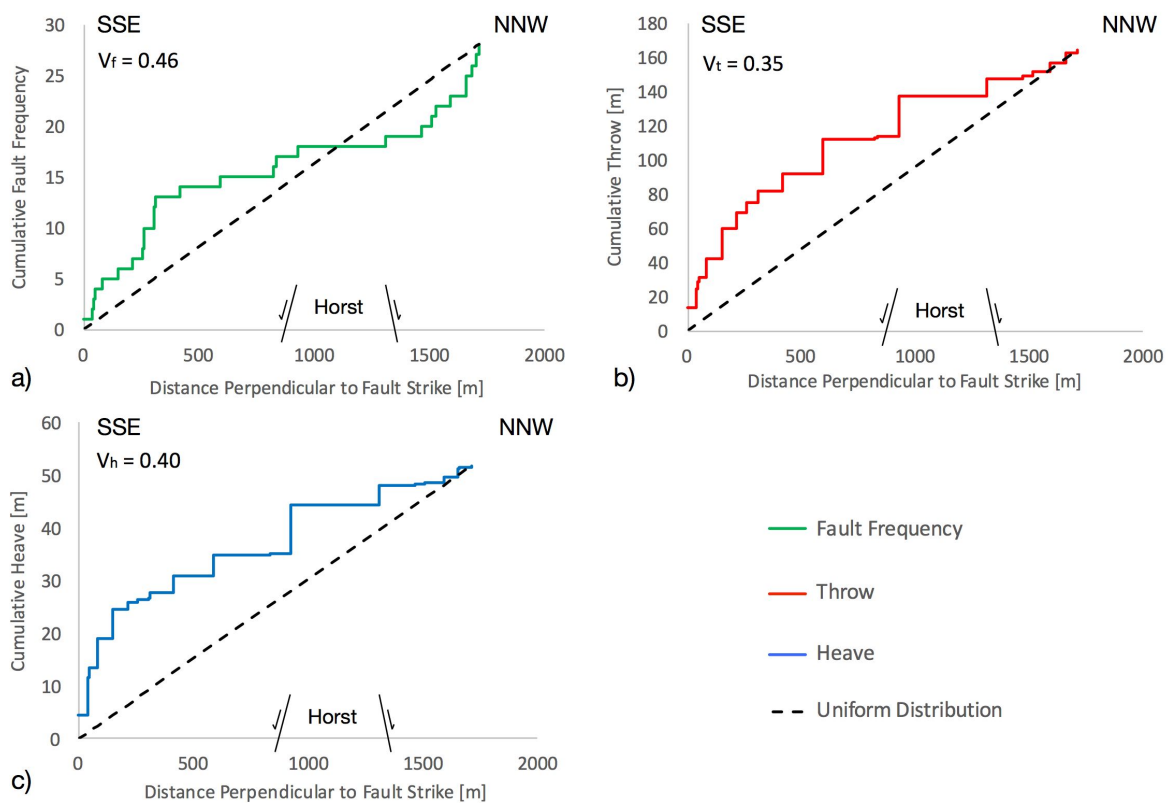

Figure 6.14 – Cumulative plots of (a) fault frequency, (b) throw and (c) heave along a transect perpendicular to the average fault strike. Throw and heave measurements are from surface S8 on the western canal wall. The datum of the transect is located in SSE at fault FS11 and extends towards NNW.
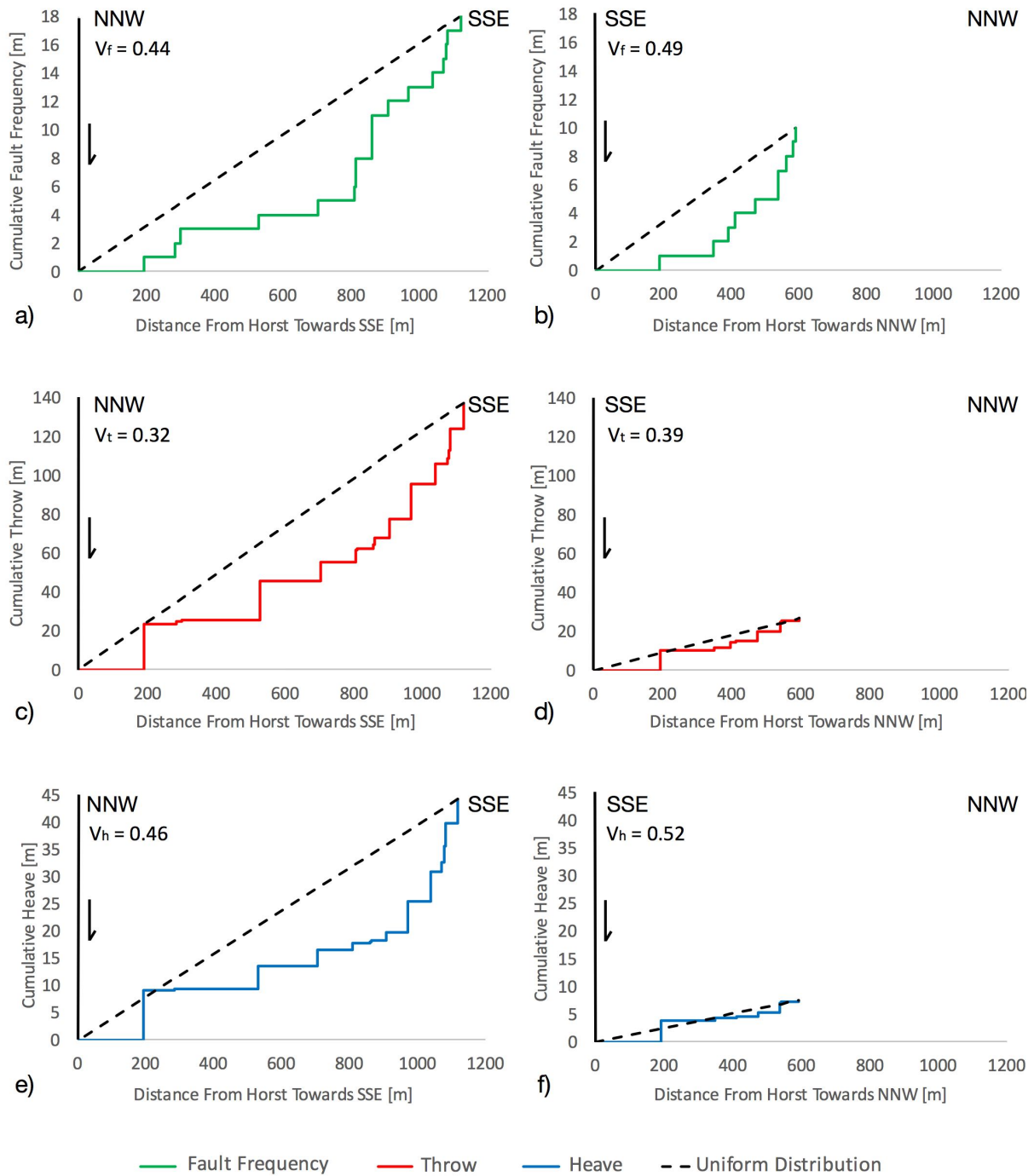
Figure 6.15 – Cumulative plots of (a, b) fault frequency, (c, d) throw and (e, f) heave along transects perpendicular to the average fault strike NW or SE of the central horst. Throw and heave measurements are from surface S8 on the western canal wall. The datum of the transects is located in the middle of the central horst and extends towards SSE (a, c, e) or NNW (b, d, f), respectively.

7 Discussion

One of the aims of this study was to determine how the normal faults exposed within the Corinth Canal grew and to determine their relative timing and fault activity. Consequently, section 7.1 will focus on the growth of individual normal faults, before discussing the evolution of the entire fault population (section 7.2) and relating it to the regional geological setting. Section 7.3 regards deformation around horst blocks and focuses on discussing the distribution of faulting, throw, heave and extension within the Corinth Canal and the implications of the study related to analogue subsurface reservoirs.

7.1 Growth of individual normal faults

Analyses of the vertical throw distributions of faults within the study area identifies two different characteristic intervals within throw profiles (Fig. 6.11, 6.12 and 6.13). Intervals that show an upwards decrease in throw with high throw gradients coincide with intervals of across-fault thickening (i.e. expansion index > 1.00). Such intervals are thus interpreted as times when faults were surface breaching syn-sedimentary growth faults (e.g. Thorsen, 1963, Cartwright et al., 1998). Intervals that are characterized by constant to very small upwards decrease in throw with no or low throw gradients, have no expansion of hanging wall strata (i.e. expansion index = 1.00). These intervals are interpreted to represent times when faults propagated as post-depositional blind faults (e.g. Hongxing & Anderson, 2007) or times when the upper fault tip became buried and inactive (e.g. Cartwright et al., 1998, Osagiede et al., 2014).

Two contrasting growth models can explain throw profiles of near constant throw or a very small upwards decrease in throw (i.e. low throw gradients) followed by a large upwards decrease in throw (i.e. high throw gradients) and across-fault thickening of strata at younger stratigraphic levels (Fig. 7.1) (e.g. Baudon & Cartwright, 2008a). One of these growth models is characterized by nucleation at the free surface as a growth fault and rapid downward propagation of the lower fault tip. The other growth model is characterized by nucleation as a blind fault that becomes a surface breaching growth fault later in its growth history.
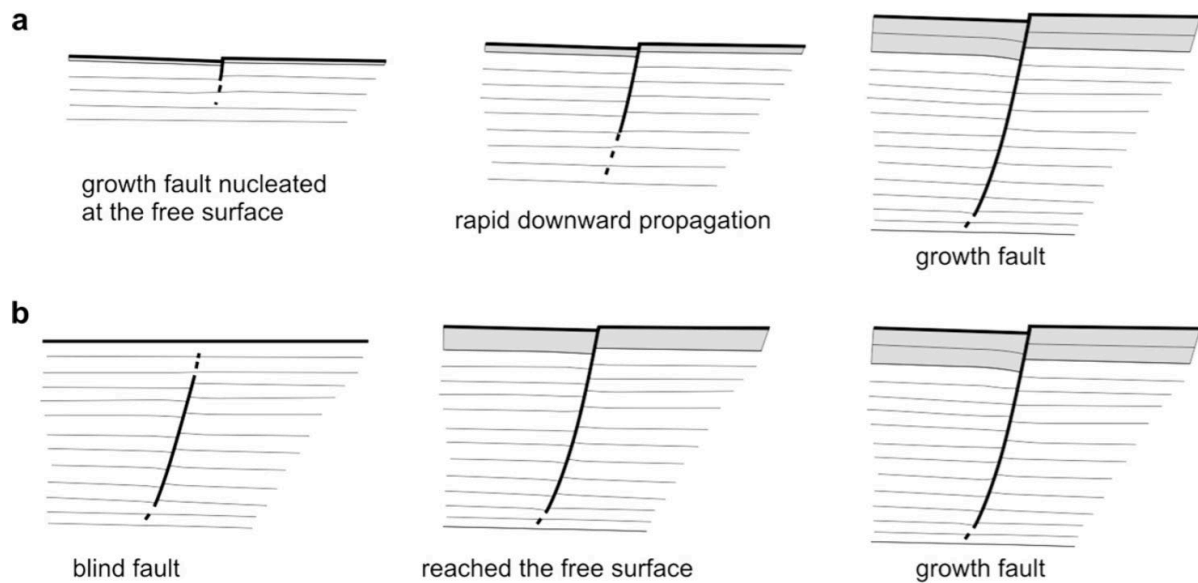
Figure 7.1 – Schematic illustration that shows two different growth models for normal faults. (a) The fault nucleated at the free surface as a growth fault and propagated rapidly downwards. (b) The fault nucleated as a blind fault and became a growth fault at a later stage in its evolution. From Baudon and Cartwright (2008a).

Some of the criteria that is utilized to recognize blind fault propagation is the presence of fault propagation folds and absence of stratigraphic evidence that a fault breached the free surface (e.g. Gawthorpe et al., 1997, Gawthorpe & Leeder, 2000, Baudon & Cartwright, 2008c). Breached monocline structures are observed in the footwall of faults FN1, FS1 and FS5 and indicate that these faults grew by blind fault propagation and created fault propagation folds early in their growth history before breaching the surface and becoming growth faults (Fig. 6.4 and 6.5). Additionally, the intervals where throw profiles show constant or very small upwards decrease in throw are not associated with any considerable stratigraphic expansion in the hanging wall. Based on these observations the faults in the canal section probably nucleated at depth and propagated to the surface as blind faults before breaching the surface (e.g. following the second growth fault model in Fig. 7.1b). Throw profiles show that after these faults interacted with the free surface, which is marked by expansion of hanging wall strata, the faults continued to grow as syn-sedimentary growth faults (Fig. 6.11, 6.12 and 6.13) (e.g. Thorsen, 1963, Cartwright et al., 1998).

Several faults are also characterized by becoming buried and inactive after a growth period, based on the observed constant throws and no across-fault thickening of strata

(Fig. 6.11, 6.12 and 6.13) (e.g. Cartwright et al., 1998, Osagiede et al., 2014). Some faults show signs of polycyclic growth with several periods of activity interrupted with periods of burial and inactivity. Renewed activity on such faults often occurs by upward propagation of the up-dip fault tip or by dip linkage with a new fault that nucleates in the overlying sediments (e.g. Baudon & Cartwright, 2008b). In the case of dip linkage, the throw profile would exhibit two throw maximum separated by a throw minimum (Fig. 4.4) (e.g. Mansfield & Cartwright, 1996, Tvedt et al., 2013). None of the throw profiles in this study show signs of dip linkage, thus renewed activity on the faults within the study area is characterized by propagation of the up-dip fault tip (Fig. 6.11, 6.12 and 6.13).

Several studies have shown that splay faults indicate the direction of fault propagation (e.g. McGrath & Davison, 1995, Perrin et al., 2015). Additionally, it has been suggested that splay faults that are located along the fault trace represent paleo-tip lines and that bends and kinks in the fault trace could also represent the paleo-tips of faults (McGrath & Davison, 1995). Hence, the splays observed for faults in the canal are further evidence that the faults grew by upwards propagation. Since none of the studied faults show signs of dip linkage in their T-z plots, changes in their geometry (e.g. bends, splays etc.) are not interpreted to be related to linking of individual fault segments as described by Childs et al. (1996). Instead the faults in the canal section probably represent surface ruptures of deep-seated faults.

7.2 Growth of normal fault populations

7.2.1 Relative fault activity

Collier (1990) dated in situ *Acropora* corals from the canal section. These corals were dated by U/Th techniques and collected from Tectonostratigraphic Units 4 and 6 (Fig. 5.1). The deposits in Tectonostratigraphic Unit 4 are dated to >350 ka, while the shoreface sandstones of stratal units SU12 and SU14 within Tectonostratigraphic Unit 6 are dated to 312 and 205 ka, respectively. The dates within Tectonostratigraphic Unit 6 are close to peaks in the global sea level curve (Marine Isotope Stages (MIS) 9 and 7) (e.g. Siddall et al., 2007). Based on this observation Collier (1990) inferred that sub-sequences, which include stratal units SU9 and SU10, SU11 and SU12, in addition to

SU13 and SU14 within Tectonostratigraphic Unit 6, correlate in age with Late-Quaternary glacio-eustatic highstands (MIS 11, MIS 9 and MIS 7, respectively) occurring approximately every 100 kyr. A similar approach has been utilized for the chronostratigraphic framework of the offshore Corinth Gulf (Fig. 7.2b, c, d) (Nixon et al., 2016). The offshore stratigraphy is divided into two seismic units, with the upper seismic unit showing alternation between high (marine) and low-amplitude (lacustrine) packages that are correlated with 100 kyr glacio-eustatic highstands. The boundary between the seismic units is a 620 kyr basin-wide unconformity, which is a boundary between lacustrine deposits and overlying marine deposits.
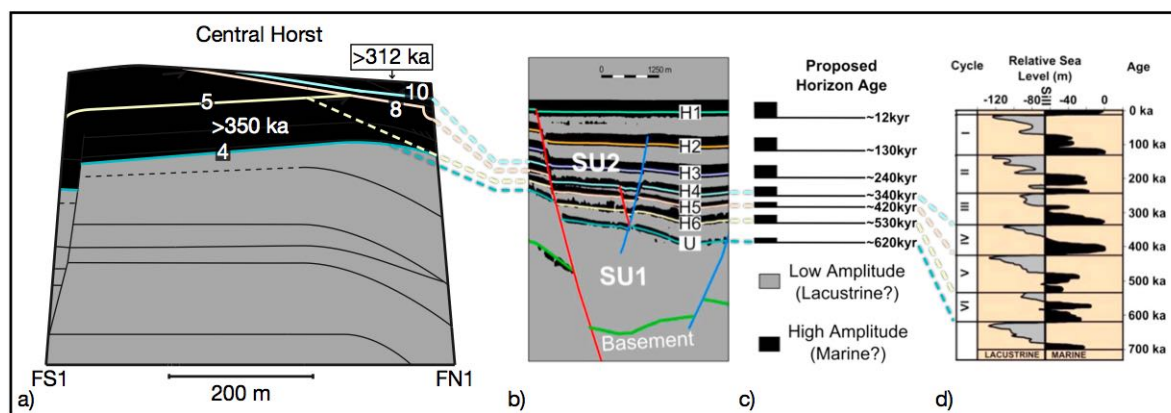

Figure 7.2 – Proposed ages for surfaces S4, S5, S8 and S10 within the canal section, correlated with the chronostratigraphic framework of the Corinth Gulf suggested by Nixon et al. (2016). (a) Schematic illustration of the central horst indicating the surfaces with assigned ages and the shift from lacustrine (gray) to marine (black) deposits. The dates from Collier (1990) are also indicated. (b) Seismic reflection profile with a volume attribute that highlights high (marine) and low (lacustrine) deposits. (c) Proposed horizon ages. (d) Sea level curve. (b, c, d) from Nixon et al. (2016).

By applying the same logic as Collier (1990) and Nixon et al. (2016) it is possible to extrapolate an age model for the key stratal surfaces (S4, S5 and S8) that bound the tectonostratigraphic units composed of marine deposits (Tectonostratigraphic Units 4, 5 and 6) (Fig. 7.2). Each surface is interpreted to represent transgressive surfaces formed prior to glacio-eustatic highstands. Both surfaces S5 and S8 represent surfaces where the deposits above the surfaces show a basinward shift in facies and one would not expect these to represent flooding surfaces. However, this can be explained by the fact that the lacustrine lowstand deposits found in the offshore regions are eroded away within the canal section. The different surfaces are assigned the ages proposed by Nixon

et al. (2016) to easily compare timing and activity of faults in the canal section and offshore in the Gulf of Corinth. Since stratal unit SU12 is dated to 312 ka, surface S10 is assigned an age of 340 ka. By following this logic downwards in the stratigraphy surfaces S8, S5 and S4 have ages of 420 ka, 530 ka and 620 ka, respectively.

Before 620 ka the faults within the study area generally grew by blind fault propagation and fault FN1 generated a fault propagation fold above the upper fault tip (Fig. 7.3a, b). Most of the faults are interpreted to have grown by blind propagation in single events. However, faults FN1.2 and FN3 show signs that these faults grew by blind propagation in a steadier manner with time. Fault FN1.1 is the only fault that breached the free surface before 620 ka (Fig. 6.11c). At or close to the 620 ka boundary (surface S4) the NW horst-bounding fault (FN1) together with most of the faults NW of the central horst (FN1.2, FN3, FN4 and FN6) breached the free surface and became syn-sedimentary growth faults (Fig. 7.3c). This also applies to faults FS4 and FS4.1 located SE of the central horst.

Most of the faults that became active around 620 ka became buried and inactive around 530 ka (surface S5) or 420 ka (surface S8). Faults FS4 and FS4.1 SE of the central horst were buried and inactive at 530 ka or earlier (Fig. 6.12f). An earlier burial is more probable, at least for fault FS4.1 as this fault is eroded by surface S5 (530 ka boundary). Northwest of the central horst, inactivity and burial seem to have occurred around 420 ka for faults FN3 and FN6, while fault FN1.2 terminated before this time (Fig. 6.11d, f, l). However, Tectonostratigraphic Unit 5 is completely removed in the NW part of the central horst and towards NW (Fig. 7.3h, i). Thus, the timing of inactivity and burial in this area is not certain as there is no preserved evidence of fault activity in the time period between 530 ka and 420 ka. Why Tectonostratigraphic Unit 5 is missing in parts of the study area can be explained by 1) subaerial erosion of Tectonostratigraphic Unit 5 (based on observation of calcretisation/karstification in the central horst), 2) erosion from the conglomerates in Tectonostratigraphic unit 6 and 3) blocking of sedimentation by surface breaching faults to the SE. A combination of these factors is probably the most reasonable assumption.
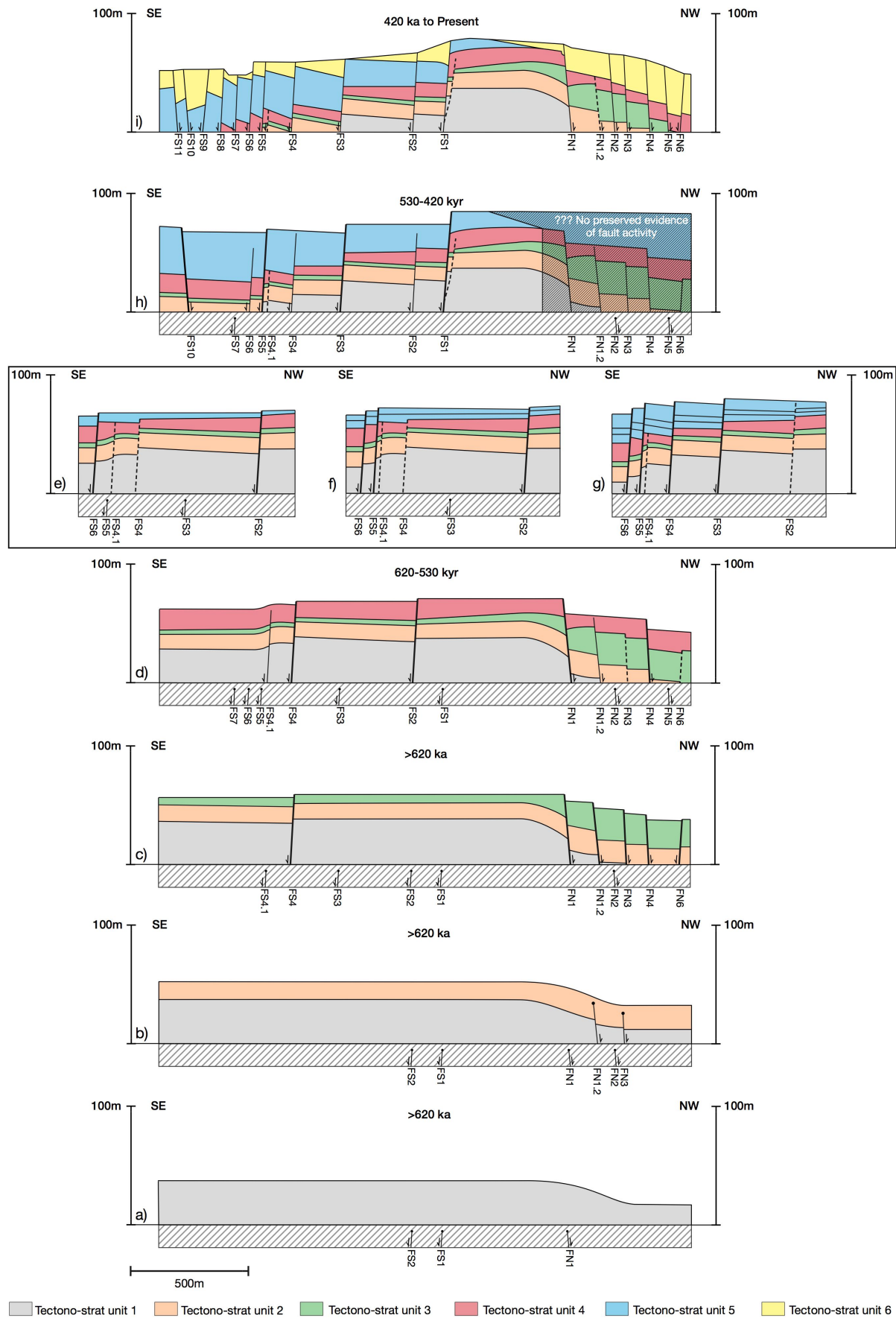
Figure 7.3 – Schematic restoration of the faults exposed on the western canal wall. (a) Blind fault propagation within Tectonostratigraphic Unit 1 and fault FN1 created a fault propagation fold. (b) Blind

fault propagation within Tectonostratigraphic 2, but faults FN1.2 and FN3 grew in a steady manner not in single events. (c) Faults FN1, FN1.2, FN3, FN4 FN6 and FS4 breached the free surface after deposition of Tectonostratigraphic Unit 3. (d) Continued activity on faults FN1, FN1.2, FN4 and FS4 during deposition of Tectonostratigraphic Unit 4. Fault FS4.1 became surface breaching within Tectonostratigraphic Unit 4, whereas fault FS2 breached the free surface after deposition of Tectonostratigraphic Unit 4. (e, f, g) Fault activity within Tectonostratigraphic Unit 5 in relation to surfaces S5.2, S6 and S7, respectively, SE of the central horst before the Isthmia Graben. (h) Faults FS2, FS3, FS4, FS5, FS6 and FS10 became surface breaching within Tectonostratigraphic Unit 5, while fault FS1 breached the surface after deposition of Tectonostratigraphic Unit 5. (i) How the outcrop looks today. Surface breaching faults are marked with thick black lines, active faults within tectonostratigraphic units are marked with thin black lines, inactive/buried faults are marked with stippled lines and blind faults are marked with a circle at its up-dip tip.

The faults located SE of the central horst show more sporadic activity compared to the faults NW of the central horst. However, these faults generally become surface breaching syn-sedimentary growth faults at different times during the time period between ca. 530 ka and ca. 420 ka (within Tectonostratigraphic Unit 5) (Fig. 7.3e, f, g). Faults that show activity within this time period are faults FS2, FS3, FS4, FS5, FS6 and FS10. Most of these faults become buried and inactive before or at ca. 420 ka and only fault FS10 shows certain signs of activity after 420 ka.

The central horst as one sees it today started developing at ca. 420 ka, when the SE horst-bounding fault breached the free surface and became a syn-sedimentary growth fault (Fig. 7.3h, i). Faults FS10, FN1 and FN4 were also surface breaching growth faults around 420 ka. Since most of the faults within the study area cut through the entire canal stratigraphy renewed activity must have occurred sometime after 420 ka.

If the faults exposed in the canal section had the same timing and activity as the faults located offshore in the Gulf of Corinth, one would expect the S-dipping faults to accommodate deformation before 620 ka with a transition period between 620 ka to 340 ka where both S- and N-dipping faults were active (Nixon et al., 2016). Around 340 ka one would see localization onto N-dipping faults. The canal section mainly exposes deposits in the 620 to 340 ka time period and the fact that both S- and N-dipping faults are active within this time period is consistent with observations from the Corinth Gulf. The S-dipping faults that displace deposits older than 620 ka do not show signs of

activity before 620 ka. However, since the faults are interpreted to propagate upwards from deep-seated faults, the S-dipping faults might have been active at an earlier stage. The timing of the N-dipping faults are consistent with deformation in the offshore regions since most of the N-dipping faults breached the free surface and became growth faults at or close to the 620 ka boundary (surface S4). Whether the faults within the Corinth Canal are characterized by localization onto N-dipping faults around 340 ka is unknown. This is due to erosion of the canal surface, which has resulted in the 340 ka surface to represent the youngest throw measurements for the N-dipping faults.

7.2.2 Regional significance

The observed increase in activity from ca. 620 ka for the faults within the study area contributed to the uplift of the Corinth Isthmus. Turner et al. (2010) calculated a maximum net uplift of 60 m based on the displacements of all the faults located within the Corinth Canal, which do not coincide with the ca. 80 m elevation of the central horst. Thus, they interpreted the uplift of the Isthmus to be related to isostatic uplift. Uplifted marine terraces are situated west of the Corinth Canal and towards the north (Keraudren & Sorel, 1987, Armijo et al., 1996, Roberts et al., 2009). The uplift of these terraces are interpreted to be related to footwall uplift by the Xylokastro and Vrachati faults located offshore in the Corinth and Lechaion Gulfs, respectively (Fig. 3.3) (Charalampakis et al., 2014). Hence, the uplift history of the Corinth Isthmus is probably complex and related to a combination of uplift from faults and regional isostatic uplift.

Several thickening trends are observed within the study area. Tectonostratigraphic Unit 3, which is older than 620 ka, is thickening towards NW (Fig. 7.3i). This might also be the case for Tectonostratigraphic Units 1 and 2, but this cannot be determined as their lower boundaries are not exposed NW of the central horst. The northwards thickening is consistent with observations from the eastern parts of the Corinth Gulf and the Lechaion Gulf, where the rift geometry from 1.5 Ma to 620 kyr was characterized by numerous north thickening half grabens (Charalampakis et al., 2014, Nixon et al., 2016). The controlling faults in the offshore region in this period were the S-dipping Heraion and Lechaion faults in addition to other buried faults (Fig. 3.3). Thus, these faults might have controlled the thickening trend seen in the canal section. However, the thickening towards NW could also be due to a more local control, where the monocline developing

above fault FN1 created a local depocenter and increased accommodation space (e.g. Gawthorpe & Leeder, 2000).

A SE thickening trend is observed for Tectonostratigraphic Unit 5 and can be explained by N-dipping controlling fault(s) (Fig. 7.3i). Since the thickening trend occurs SE of the central horst, the controlling N-dipping fault(s) must be located further SE of the study area. Few studies are conducted in this area making it impossible to say anything definite. One possibility is that the thickening trend is related to the N-dipping Kenchreai and Klenia faults that bound the Corinth-Nemea basin to the S (Fig. 3.3) (Charalampakis et al., 2014). However, studies from the Corinth Rift show a northward migration of faulting during Pleistocene and these faults were probably not active between 530 ka and 420 ka (e.g. Charalampakis et al., 2014, Nixon et al., 2016). Other possibilities are a N-dipping fault further SE of the study area exposed within the canal section (Collier, 1990, Turner et al., 2010) or N-dipping faults within the Saronic Gulf.

Tectonostratigraphic Unit 6, which is younger than 420 ka, is thickening towards the NW from the central horst (Fig. 7.3i). This thickening trend can be related to a main depocenter located within the Lechaion Gulf that was controlled by the S-dipping Heraion, Vouliagmeni north and south and Loutraki faults at that time (Fig. 3.3) (Charalampakis et al., 2014). It seems that the thickening of the different stratal units within Tectonostratigraphic unit 6 is related to short term lowstand events within the glacio-eustatic highstand events where accelerating rise in relative sea level causes progradation and aggradation of the deposits (e.g. Collier, 1990, Catuneanu et al., 2011).

7.3 Deformation around horst blocks

7.3.1 Corinth Canal

Cumulative plots of fault frequency, throw and heave show how deformation is distributed within the study area (Fig. 6.14). The entire fault population is characterized by moderate heterogeneity indicating that the faults are not equally spaced and that the faults accommodate different amounts of throw and heave (Putz-Perrier & Sanderson, 2008a, 2008b). The moderate heterogeneity is probably related to the fact that the

central horst is characterized by very limited deformation and that the deformation is accommodated in the half grabens on either side of the central horst.

When separating the faults located NW of the central horst from the faults located SE of the central horst, moderate to high heterogeneity values are found from the cumulative heave plots, at least NW of the central horst (Fig. 6.15f). This implies that one fault, the horst-bounding fault, accommodates most of the heave (52% of total heave NW of the central horst). In comparison, the faults SE of the central horst do not show as high heterogeneity and heave is distributed between several larger faults, with the horst-bounding fault accommodating 20% of total heave SE of the central horst (Fig. 6.15e). This is consistent with the observation that fault populations often contain a few large faults where deformation is localized (e.g. Putz-Perrier & Sanderson, 2010, Nixon et al., 2014).

The faults SE of the central horst accommodate 4% extension, while the faults NW of the central horst accommodate 1% extension. Additionally, the S-dipping faults SE of the central horst take up ca. 112 m throw, whereas the N-dipping faults NW of the central horst take up ca. 25 m throw. That the faults SE of the central horst accommodate more extension and throw compared to the faults NW of the central horst is probably related to the fact that the fault blocks SE of the central horst are tilted in a domino fashion (e.g. Nixon et al., 2011). Different styles of faulting are thus observed NW and SE of the central horst. Observation of rotation into S-dipping faults are also observed offshore in the Gulf of Corinth, while the N-dipping faults show little or no rotation (Nixon et al., 2016). Additionally, from 620 ka to present, the eastern part of the Corinth Gulf was characterized by numerous horst blocks due to increased activity of the Perachora Fault (Fig. 3.3). The timing of horst formation in the canal and the eastern Corinth Gulf is thus occurring more or less at the same time.

7.3.2 Implications of the study

Subsurface reservoirs are studied with the aid from seismic reflection data, well logs and cores. There is a significant gap in scale between seismic data (vertical and horizontal resolution >10 m) and well data (vertical resolution <10 m and horizontal resolution <10 cm) (e.g. Enge et al., 2007, Rarity et al., 2014). Outcrop data covers both these scale

ranges and closes the gap in scale between seismic data and well data. Thus, outcrop data are often utilized as analogues for subsurface reservoirs. This study provides an analogue to rift intrabasinal highs, horst blocks and half grabens with rotated fault blocks. Such structural features are observed in rift basins all over the world and are important hydrocarbon-bearing provinces. Numerous fields in the North Sea are producing hydrocarbons from horst blocks (e.g. the Brage field in the Norwegian sector and the Penguins Cluster in the British sector) and rotated fault blocks (e.g. the Gullfaks field in the Norwegian sector) (e.g. Fossen & Hesthammer, 1998, Lien et al., 1998, Domínguez, 2007). It must be emphasized that the structures and bounding faults of the aforementioned fields are much larger than the ones observed within the study area. Most of the faults within the canal section have throw values of <10 m and would represent subseismic faults that are not visible on seismic reflection data (e.g. Enge et al., 2007, Rarity et al., 2014). However, the horst-bounding faults and faults FS3 and FS8 have throw values between ca. 16 m and ca. 23 m and could be visible on seismic, depending on the burial depth and resolution of the seismic reflection data. Hence, if the canal section was a subsurface reservoir studied by seismic reflection data the structural style would be less complex than observed and probably characterized by a horst block with two rotated faults blocks located SE of the horst.

Fault sealing represents one of the key factors that controls trapping of hydrocarbons within reservoirs (e.g. Knipe et al., 1997). Fault seals form due to juxtaposition of reservoir rocks against non-reservoir rocks or by the existence of a low permeable membrane seal (i.e. smear, cementation or cataclasis) (e.g. Færseth, 2006). Since the faults within the canal section do not have very large throws, self-juxtaposition, where potential reservoir rocks are partially juxtaposed against themselves across the faults, commonly occurs (Farseth et al., 2007). Thus, to prevent leakage a membrane seal must be in place. This would probably also be the case in subsurface reservoirs bound by faults with relatively low throws. An exception to this is where reservoir units are very thin and thus represents self-separated reservoirs.

Factors such as fault zone architecture, continuity and geometry of faults and the presence of subseismic faults are crucial factors in understanding fluid flow and sealing capacity of faults in the subsurface (e.g. Caine et al., 1996, Hesthammer & Fossen, 2000).

The faults exposed in the canal section provide examples of e.g. contractional overlaps, hard linked structures and lenses (Fig. 6.4b and 6.6). These structures would not be recognizable on seismic and could represent places with increased across-fault connectivity. Lenses may also impede across-fault connectivity, which is determined by their composition. Permeable host rock lenses may enhance connectivity across faults, whereas fault rock lenses with low permeability might impede connectivity across faults (e.g. Childs et al., 1997, Knipe, 1997). As already mentioned, most of the studied faults would represent subseismic faults. Thus, the deformation occurring in the half grabens on either side of the central horst would be underestimated in seismic reflection data. Additionally, these faults could represent barriers or baffles to fluid flow, which might result in compartmentalization and complex reservoirs (e.g. Damsleth et al., 1998).

The distribution of sediments around horst blocks often show thinning and pinchout towards or on the horst and thickening within the grabens or half grabens surrounding the horst (e.g. Domínguez, 2007). Such a sediment distribution is also observed in the canal section. However, the detailed stratigraphic framework presented in this study would not be visible with the same resolution on seismic reflection data. This could result in underestimation of the lateral and vertical extent of possible reservoir units, which would have implications for volume estimates.

8 Conclusions and further work

8.1 Conclusions

By combining traditional field data with LiDAR-based digital outcrop data this study has described and characterized the geometry, fault zones and structural evolution of the normal fault population exposed within the Corinth Canal in central Greece. The fault population comprises N- and S-dipping faults that are predominantly located NW and SE of the central horst, respectively. The faults show variability in their geometry and surrounding damage zones. With the aid from cumulative plots, the distribution of faults, throw and heave within the canal section was investigated. The main conclusions related to fault geometry, fault zone architecture and distribution of deformation within the Corinth Canal are the following:

- The faults have planar, listric or vertically and laterally segmented fault geometries. Faults that are vertically segmented have a range of different geometries, which include contractional overlaps, contractional and extensional bends, hard linked structures and lenses.

- Damage zones are generally narrow and the main structural elements that constitute the damage zones are splay faults and smaller scale faults. Additionally, local folding and lenses occur in a few places.

- The entire fault population accommodates 3% extension and the distribution of faults, throw and heave is moderately heterogeneous.

- Faults located SE of the central horst accommodate 4% extension, whereas faults located NW of the central horst accommodate 1% extension. Hence, strain is localized to the half graben SE of the central horst.

- Both NW and SE of the central horst the horst-bounding faults represent the fault that accommodates most of the heave, ca. 52% and ca. 20%, respectively, indicating localization of strain onto these faults.

The growth history of the studied faults was examined with the aid from throw-depth plots and expansion indices. Their relative timing was described based on a proposed age model where the key stratal surfaces that bound the marine tectonostratigraphic units represent transgressive surfaces formed prior to glacio-eustatic highstands

occurring approximately every 100 kyr. The following conclusions can be drawn in relation to the relative timing and growth history of the studied faults:

- Throw profiles of the faults show no signs of dip linkage, thus their vertical growth is not characterized by linking of individual fault segments.

- The faults are interpreted to have nucleated at depth and propagated as blind faults before breaching the surface and becoming syn-sedimentary growth faults.

- Several faults have also become buried and inactive after a growth period and some faults show signs of polycyclic growth.

- The faults generally grew by blind fault propagation before 620 ka. Most of the N-dipping faults breached the free surface and became syn-sedimentary growth faults around 620 ka.

- More sporadic activity characterizes the S-dipping faults, but they generally became syn-sedimentary growth faults during the time period between ca. 530 ka and ca. 420 ka.

- The development of the central horst as it's seen today started at ca. 420 ka, when the SE horst-bounding fault breached the free surface and became a syn-sedimentary growth fault.

This study provides new insight into the structural evolution of the Corinth Canal and the Corinth Isthmus, where limited amounts of studies are conducted. Based on the proposed age model this study has shown that the normal fault population exposed within the Corinth Canal seems to have the same timing and activity as faults located offshore in the Corinth Gulf, thus linking the structural evolution of the Corinth Canal sector with the structural evolution of the Corinth Rift. Furthermore, the study represents an analogue to rift intrabasinal highs, horst blocks and half grabens with rotated fault blocks. The study emphasizes that structural and stratigraphic detail observed in the field and in the digital outcrop model would not be visible on seismic reflection data, which could result in underestimation of deformation occurring around horst blocks and the lateral and vertical extent of possible reservoir units.

8.2 Further work

Seismic studies that focus on normal fault growth usually utilize expansion indices and thickness maps (i.e. isopach or isochron maps) to reveal the growth history of faults (e.g. Jackson & Rotevatn, 2013, Tvedt et al., 2013). In this study only expansion indices are utilized and the creation of isopach maps would strengthen the quantification and interpretations related to growth intervals and large scale thickening trends observed within the Corinth Canal.

Digital outcrop datasets can be integrated into reservoir modelling software (e.g. RMS by Roxar Software Solutions or Petrel by Schlumberger) to generate three-dimensional geocellular models (e.g. Rotevatn et al., 2009, Rarity et al., 2014). Such models represent the standard method for investigating subsurface reservoirs and provide a framework to simulate fluid flow within reservoirs and to develop production strategies (e.g. Flint & Bryant, 1993). The basic workflow for constructing reservoir models involve creating a structural model composed of faults and stratal surfaces, generate a three-dimensional grid, populate the grid with facies and petrophysical properties (e.g. porosity and permeability) and simulate fluid flow (e.g. Rotevatn et al., 2009). The input to the structural model is provided in this study. Additionally, the different facies exposed within the canal section are described by Meling (2016). However, the petrophysical properties of the rocks are not studied and analogues from e.g. the Norwegian Continental Shelf or further field work is necessary to simulate fluid flow scenarios within the Corinth Canal.

Due to the limited amount of dates available from the Corinth Canal and the Corinth Isthmus region the timing of fault activity is uncertain. Thus, a study focusing on producing a robust chronostratigraphic model for this area would be highly useful. Furthermore, since the faults within the canal section are interpreted to represent the up-dip tips of deep-seated faults, this study only considers the more recent growth history of the faults. It would be very interesting to study more of the growth history of these faults, which might be achieved by sampling seismic reflection data through the Corinth Canal. A seismic study conducted in the Saronic Gulf could also shed light to the evolution of the Corinth Canal and the Corinth Isthmus region.

9 Reference list

Armijo, R., Meyer, B., Hubert, A., Barka, A. 1999. Westward propagation of the North Anatolian fault into the northern Aegean: Timing and kinematics. Geology 27, 267-270.

Armijo, R., Meyer, B., King, G. C. P., Rigo, A., Papanastassiou, D. 1996. Quaternary evolution of the Corinth Rift and its implications for the Late Cenozoic evolution of the Aegean. Geophysical Journal International 126, 11-53.

Avallone, A., Briole, P., Agatza-Balodimou, A. M., Billiris, H., Charade, O., Mitsakaki, C., Nercessian, A., Papazissi, K., Paradissis, D., Veis, G. 2004. Analysis of eleven years of deformation measured by GPS in the Corinth Rift Laboratory area. Comptes Rendus Geoscience 336, 301-311.

Barnett, J. A. M., Mortimer, J., Rippon, J. H., Walsh, J. J., Watterson, J. 1987. Displacement geometry in the volume containing a single normal fault. AAPG Bulletin 71, 925-937.

Bastesen, E., Braathen, A. 2010. Extensional faults in fine grained carbonates – analysis of fault core lithology and thickness–displacement relationships. Journal of Structural Geology 32, 1609-1628.

Baudon, C. 2007. Propagation and early growth of normal faults. Unpublished PhD thesis, Cardiff University.

Baudon, C., Cartwright, J. 2008a. Early stage evolution of growth faults: 3D seismic insights from the Levant Basin, Eastern Mediterranean. Journal of Structural Geology 30, 888-898.

Baudon, C., Cartwright, J. 2008b. The kinematics of reactivation of normal faults using high resolution throw mapping. Journal of Structural Geology 30, 1072-1084.

Baudon, C., Cartwright, J. A. 2008c. 3D seismic characterisation of an array of blind normal faults in the Levant Basin, Eastern Mediterranean. Journal of Structural Geology 30, 746-760.

Bell, R. E., McNeill, L. C., Bull, J. M., Henstock, T. J. 2008. Evolution of the offshore western Gulf of Corinth. Geological Society of America Bulletin 120, 156-178.

Bell, R. E., McNeill, L. C., Bull, J. M., Henstock, T. J., Collier, R. E. L., Leeder, M. R. 2009. Fault architecture, basin structure and evolution of the Gulf of Corinth Rift, central Greece. Basin Research 21, 824-855.

Bellian, J. A., Kerans, C., Jennette, D. C. 2005. Digital Outcrop Models: Applications of Terrestrial Scanning Lidar Technology in Stratigraphic Modeling. Journal of Sedimentary Research 75, 166-176.

Bernard, P., Lyon-Caen, H., Briole, P., Deschamps, A., Boudin, F., Makropoulos, K., Papadimitriou, P., Lemeille, F., Patau, G., Billiris, H., Paradissis, D., Papazissi, K.,

Castarède, H., Charade, O., Nercessian, A., Avallone, A., Pacchiani, F., Zahradnik, J., Sacks, S., Linde, A. 2006. Seismicity, deformation and seismic hazard in the western rift of Corinth: New insights from the Corinth Rift Laboratory (CRL). Tectonophysics 426, 7-30.

Biddle, K. T., Christie-Blick, N. 1985. *Strike-Slip Deformation, Basin Formation, and Sedimentation.* The Society of Economic Paleontologists and Mineralogists. 375-386

Buckley, S. J., Enge, H. D., Carlsson, C., Howell, J. A. 2010. Terrestrial laser scanning for use in virtual outcrop geology. The Photogrammetric Record 25, 225-239.

Buckley, S. J., Howell, J. A., Enge, H. D., Kurz, T. H. 2008. Terrestrial laser scanning in geology: data acquisition, processing and accuracy considerations. Journal of the Geological Society 165, 625-638.

Caine, J. S., Evans, J. P., Forster, C. B. 1996. Fault zone architecture and permeability structure. Geology 24, 1025-1028.

Cartwright, J., Bouroullec, R., James, D., Johnson, H. 1998. Polycyclic motion history of some Gulf Coast growth faults from high-resolution displacement analysis. Geology 26, 819-822.

Cartwright, J. A., Trudgill, B. D., Mansfield, C. S. 1995. Fault growth by segment linkage: an explanation for scatter in maximum displacement and trace length data from the Canyonlands Grabens of SE Utah. Journal of Structural Geology 17, 1319-1326.

Catuneanu, O., Galloway, W. E., Kendall, C. G. S. C., Miall, A. D., Posamentier, H. W., Strasser, A., Tucker, M. E. 2011. Sequence stratigraphy: methodology and nomenclature. Newsletters on stratigraphy 44, 173-245.

Charalampakis, M., Lykousis, V., Sakellariou, D., Papatheodorou, G., Ferentinos, G. 2014. The tectono-sedimentary evolution of the Lechaion Gulf, the south eastern branch of the Corinth graben, Greece. Marine Geology 351, 58-75.

Chester, F. M., Logan, J. M. 1987. Composite planar fabric of gouge from the Punchbowl Fault, California. Journal of Structural Geology 9, 621-634.

Childs, C., Manzocchi, T., Walsh, J. J., Bonson, C. G., Nicol, A., Schöpfer, M. P. J. 2009. A geometric model of fault zone and fault rock thickness variations. Journal of Structural Geology 31, 117-127.

Childs, C., Nicol, A., Walsh, J. J., Watterson, J. 1996. Growth of vertically segmented normal faults. Journal of Structural Geology 18, 1389-1397.

Childs, C., Nicol, A., Walsh, J. J., Watterson, J. 2003. The growth and propagation of synsedimentary faults. Journal of Structural Geology 25, 633-648.

Childs, C., Walsh, J. J., Watterson, J. 1997. Complexity in fault zone structure and implications for fault seal prediction. Norwegian Petroleum Society Special Publications 7, 61-72.

Childs, C., Watterson, J., Walsh, J. J. 1995. Fault overlap zones within developing normal fault systems. Journal of the Geological Society 152, 535-549.

Clarke, P. J., Davies, R. R., England, P. C., Parsons, B. E., Billiris, H., Paradissis, D., Veis, G., Denys, P. H., Cross, P. A., Ashkenazi, V., Bingley, R. 1997. Geodetic estimate of seismic hazard in the Gulf of Korinthos. Geophysical Research Letters 24, 1303-1306.

Collier, R. E. L. 1990. Eustatic and tectonic controls upon Quaternary coastal sedimentation in the Corinth Basin, Greece. Journal of the Geological Society 147, 301-314.

Collier, R. E. L., Dart, C. J. 1991. Neogene to Quaternary rifting, sedimentation and uplift in the Corinth Basin,Greece. Journal of the Geological Society 148, 1049-1065.

Collier, R. E. L., Leeder, M. R., Rowe, P. J., Atkinson, T. C. 1992. Rates of tectonic uplift in the Corinth and Megara Basins, central Greece. Tectonics 11, 1159-1167.

Collier, R. E. L., Thompson, J. 1991. Transverse and linear dunes in an Upper Pleistocene marine sequence, Corinth Basin, Greece. Sedimentology 38, 1021-1040.

Cowie, P. A. 1998. A healing–reloading feedback control on the growth rate of seismogenic faults. Journal of Structural Geology 20, 1075-1087.

Cowie, P. A., Gupta, S., Dawers, N. H. 2000. Implications of fault array evolution for synrift depocentre development: insights from a numerical fault growth model. Basin Research 12, 241-261.

Cowie, P. A., Scholz, C. H. 1992. Physical explanation for the displacement-length relationship of faults using a post-yield fracture mechanics model. Journal of Structural Geology 14, 1133-1148.

Cowie, P. A., Shipton, Z. K. 1998. Fault tip displacement gradients and process zone dimensions. Journal of Structural Geology 20, 983-997.

Crowell, J. C. 1974. *Origin of Late Cenozoic basins in southern California*. The Society of Economic Paleontologists and Mineralogists.190-204

Damsleth, E., Sangolt, V., Aamodt, G. 1998. Sub-seismic Faults Can Seriously Affect Fluid Flow in the Njord Field off Western Norway - A Stochastic Fault Modeling Case Study. Society of Petroleum Engineers, 295-304.

Davatzes, N. C., Aydin, A. 2003. The formation of conjugate normal fault systems in folded sandstone by sequential jointing and shearing, Waterpocket monocline, Utah. Journal of Geophysical Research: Solid Earth 108, 2478.

Dawers, N. H., Anders, M. H. 1995. Displacement-length scaling and fault linkage. Journal of Structural Geology 17, 607-614.

Dawers, N. H., Anders, M. H., Scholz, C. H. 1993. Growth of normal faults: Displacement-length scaling. Geology 21, 1107-1110.

Dewey, J. F., Sengor, A. M. C. 1979. Aegean and surrounding regions: Complex multiplate and continuum tectonics in a convergent zone. Geological Society of America Bulletin 90, 84-92.

Domínguez, R. 2007. Structural evolution of the Penguins Cluster, UK northern North Sea. Geological Society, London, Special Publications 292, 25-48.

Duffy, O. B., Brocklehurst, S. H., Gawthorpe, R. L., Leeder, M. R., Finch, E. 2015. Controls on landscape and drainage evolution in regions of distributed normal faulting: Perachora Peninsula, Corinth Rift, Central Greece. Basin Research 27, 473-494.

Enge, H. D., Buckley, S. J., Rotevatn, A., Howell, J. A. 2007. From outcrop to reservoir simulation model: Workflow and procedures. Geosphere 3, 469-490.

Færseth, R. B. 2006. Shale smear along large faults: continuity of smear and the fault seal capacity. Journal of the Geological Society 163, 741-751.

Farseth, R. B., Johnsen, E., Sperrevik, S. 2007. Methodology for risking fault seal capacity: Implications of fault zone architecture. AAPG bulletin 91, 1231-1246.

Faulkner, D. R., Jackson, C. A. L., Lunn, R. J., Schlische, R. W., Shipton, Z. K., Wibberley, C. A. J., Withjack, M. O. 2010. A review of recent developments concerning the structure, mechanics and fluid flow properties of fault zones. Journal of Structural Geology 32, 1557-1575.

Ferrill, D. A., Morris, A. P. 2008. Fault zone deformation controlled by carbonate mechanical stratigraphy, Balcones fault system, Texas. AAPG Bulletin 92, 359-380.

Flint, S. S., Bryant, I. D. 1993. *The geological modelling of hydrocarbon reservoirs and outcrop analogues.* Blackwell Scientific Publications, Special Publication of the International Association of Sedimentologists.249

Ford, M., Rohais, S., Williams, E. A., Bourlange, S., Jousselin, D., Backert, N., Malartre, F. 2013. Tectono-sedimentary evolution of the western Corinth rift (Central Greece). Basin Research 25, 3-25.

Fossen, H., Hesthammer, J. 1998. Structural geology of the Gullfaks field, northern North Sea. Geological Society, London, Special Publications 127, 231-261.

Gawthorpe, R. L., Leeder, M. R. 2000. Tectono-sedimentary evolution of active extensional basins. Basin Research 12, 195-218.

Gawthorpe, R. L., Sharp, I., Underhill, J. R., Gupta, S. 1997. Linked sequence stratigraphic and structural evolution of propagating normal faults. Geology 25, 795-798.

Giba, M., Walsh, J. J., Nicol, A. 2012. Segmentation and growth of an obliquely reactivated normal fault. Journal of Structural Geology 39, 253-267.

Goldsworthy, M., Jackson, J. 2001. Migration of activity within normal fault systems: examples from the Quaternary of mainland Greece. Journal of Structural Geology 23, 489-506.

Granier, T. 1985. Origin, damping, and pattern of development of faults in granite. Tectonics 4, 721-737.

Hesthammer, J., Fossen, H. 2000. Uncertainties associated with fault sealing analysis. Petroleum Geoscience 6, 37-45.

Hodgetts, D. 2009. LiDAR in the Environmental Sciences: Geological Applications. In: *Laser Scanning for the Environmental Sciences*. Wiley-Blackwell, 165-179.

Hongxing, G., Anderson, J. K. 2007. Fault throw profile and kinematics of Normal fault: conceptual models and geologic examples. Geological Journal of China Universities 13, 75-88.

Jackson, C. A.-L., Rotevatn, A. 2013. 3D seismic analysis of the structure and evolution of a salt-influenced normal fault zone: a test of competing fault growth models. Journal of Structural Geology 54, 215-234.

Jackson, J. A., Gagnepain, J., Houseman, G., King, G. C. P., Papadimitriou, P., Soufleris, C., Virieux, J. 1982. Seismicity, normal faulting, and the geomorphological development of the Gulf of Corinth (Greece): the Corinth earthquakes of February and March 1981. Earth and Planetary Science Letters 57, 377-397.

Jolivet, L. 2001. A comparison of geodetic and finite strain pattern in the Aegean, geodynamic implications. Earth and Planetary Science Letters 187, 95-104.

Jolivet, L., Daniel, J. M., Truffert, C., Goffé, B. 1994. Tectonics, metamorphism and magmatism in island arcs Exhumation of deep crustal metamorphic rocks and crustal extension in arc and back-arc regions. Lithos 33, 3-30.

Jolivet, L., Faccenna, C., Huet, B., Labrousse, L., Le Pourhiet, L., Lacombe, O., Lecomte, E., Burov, E., Denèle, Y., Brun, J.-P., Philippon, M., Paul, A., Salaün, G., Karabulut, H., Piromallo, C., Monié, P., Gueydan, F., Okay, A. I., Oberhänsli, R., Pourteau, A., Augier, R., Gadenne, L., Driussi, O. 2013. Aegean tectonics: Strain localisation, slab tearing and trench retreat. Tectonophysics 597–598, 1-33.

Keraudren, B., Sorel, D. 1987. The terraces of Corinth (Gerrce) — A detailed record of eustatic sea-level variations during the last 500,000 years. Marine Geology 77, 99-107.

Kim, Y.-S., Peacock, D. C. P., Sanderson, D. J. 2003. Mesoscale strike-slip faults and damage zones at Marsalforn, Gozo Island, Malta. Journal of Structural Geology 25, 793-812.

Kim, Y.-S., Peacock, D. C. P., Sanderson, D. J. 2004. Fault damage zones. Journal of Structural Geology 26, 503-517.

Knipe, R. 1997. Juxtaposition and seal diagrams to help analyze fault seals in hydrocarbon reservoirs. AAPG bulletin 81, 187-195.

Knipe, R. J., Fisher, Q. J., Jones, G., Clennell, M. R., Farmer, A. B., Harrison, A., Kidd, B., McAllister, E., Porter, J. R., White, E. A. 1997. Fault seal analysis: successful methodologies, application and future directions. Norwegian Petroleum Society Special Publications 7, 15-38.

Kranis, H., Skourtsos, E., Gawthorpe, R. L., Leeder, M., Stamatakis, M. 2015. Pre-rift basement structure and syn-rift faulting at the eastern onshore Gulf of Corinth Rift In: *EGU General Assembly* **17**, Vienna, Austria.

Larsen, P.-H. 1988. Relay structures in a Lower Permian basement-involved extension system, East Greenland. Journal of Structural Geology 10, 3-8.

Le Pichon, X., Angelier, J. 1979. The Hellenic arc and trench system: a key to the neotectonic evolution of the eastern Mediterranean area. Tectonophysics 60, 1-42.

Le Pourhiet, L., Burov, E., Moretti, I. 2003. Initial crustal thickness geometry controls on the extension in a back arc domain: Case of the Gulf of Corinth. Tectonics 22, 1032.

Leeder, M. R., Mack, G. H., Brasier, A. T., Parrish, R. R., McIntosh, W. C., Andrews, J. E., Duermeijer, C. E. 2008. Late-Pliocene timing of Corinth (Greece) rift-margin fault migration. Earth and Planetary Science Letters 274, 132-141.

Leeder, M. R., McNeill, L. C., Ll Collier, R. E., Portman, C., Rowe, P. J., Andrews, J. E., Gawthorpe, R. L. 2003. Corinth rift margin uplift: New evidence from Late Quaternary marine shorelines. Geophysical Research Letters 30, 1611.

Lien, S. C., Lie, S. E., Fjellbirkeland, H., Larsen, S. V. 1998. Brage Field, Lessons Learned After 5 Years of Production. Society of Petroleum Engineers, 103-120.

Mansfield, C. S., Cartwright, J. A. 1996. High resolution fault displacement mapping from three-dimensional seismic data: evidence for dip linkage during fault growth. Journal of Structural Geology 18, 249-263.

McCaffrey, K. J. W., Jones, R. R., Holdsworth, R. E., Wilson, R. W., Clegg, P., Imber, J., Holliman, N., Trinks, I. 2005. Unlocking the spatial dimension: digital technologies and the future of geoscience fieldwork. Journal of the Geological Society 162, 927-938.

McClusky, S., Balassanian, S., Barka, A., Demir, C., Ergintav, S., Georgiev, I., Gurkan, O., Hamburger, M., Hurst, K., Kahle, H., Kastens, K., Kekelidze, G., King, R., Kotzev, V., Lenk, O., Mahmoud, S., Mishin, A., Nadariya, M., Ouzounis, A., Paradissis, D., Peter, Y., Prilepin, M., Reilinger, R., Sanli, I., Seeger, H., Tealeb, A., Toksöz, M. N., Veis, G. 2000. Global Positioning System constraints on plate kinematics and dynamics in

the eastern Mediterranean and Caucasus. Journal of Geophysical Research: Solid Earth 105, 5695-5719.

McGrath, A. G., Davison, I. 1995. Damage zone geometry around fault tips. Journal of Structural Geology 17, 1011-1024.

McKenzie, D. 1972. Active Tectonics of the Mediterranean Region. Geophysical Journal International 30, 109-185.

McKenzie, D. 1978. Active tectonics of the Alpine—Himalayan belt: the Aegean Sea and surrounding regions. Geophysical Journal International 55, 217-254.

McKenzie, D. P. 1970. Plate Tectonics of the Mediterranean Region. Nature 226, 239-243.

Meling, S. V. 2016. Sedimentology and sequence stratigraphy of the Corinth Canal, central Greece. Unpublished Master thesis, University of Bergen

Nicol, A., Walsh, J. J., Watterson, J., Bretan, P. G. 1995. Three-dimensional geometry and growth of conjugate normal faults. Journal of Structural Geology 17, 847-862.

Nixon, C. W., Bull, J. M., Sanderson, D. J. 2014. Localized vs distributed deformation associated with the linkage history of an active normal fault, Whakatane Graben, New Zealand. Journal of Structural Geology 69, Part A, 266-280.

Nixon, C. W., McNeill, L. C., Bull, J. M., Bell, R. E., Gawthorpe, R. L., Henstock, T. J., Christodoulou, D., Ford, M., Taylor, B., Sakellariou, D., Ferentinos, G., Papatheodorou, G., Leeder, M. R., Collier, R. E. L. I., Goodliffe, A. M., Sachpazi, M., Kranis, H. 2016. Rapid spatiotemporal variations in rift structure during development of the Corinth Rift, central Greece. Tectonics 35, 1225-1248.

Nixon, C. W., Sanderson, D. J., Bull, J. M. 2011. Deformation within a strike-slip fault network at Westward Ho!, Devon U.K.: Domino vs conjugate faulting. Journal of Structural Geology 33, 833-843.

Nomikou, P., Papanikolaou, D., Alexandri, M., Sakellariou, D., Rousakis, G. 2013. Submarine volcanoes along the Aegean volcanic arc. Tectonophysics 597–598, 123-146.

Ori, G. G. 1989. Geologic history of the extensional basin of the Gulf of Corinth (?Miocene-Pleistocene), Greece. Geology 17, 918-921.

Osagiede, E. E., Duffy, O. B., Jackson, C. A. L., Wrona, T. 2014. Quantifying the growth history of seismically imaged normal faults. Journal of Structural Geology 66, 382-399.

Papanikolaou, D., Lykousis, V., Chronis, G., Pavlakis, P. 1988. A comparative study of neotectonic basins across the Hellenic arc: the Messiniakos, Argolikos, Saronikos and Southern Evoikos Gulfs. Basin Research 1, 167-176.

Peacock, D. C. P., Knipe, R. J., Sanderson, D. J. 2000. Glossary of normal faults. Journal of Structural Geology 22, 291-305.

Peacock, D. C. P., Sanderson, D. J. 1991. Displacements, segment linkage and relay ramps in normal fault zones. Journal of Structural Geology 13, 721-733.

Peacock, D. C. P., Sanderson, D. J. 1994. Geometry and development of relay ramps in normal fault systems. AAPG Bulletin 78, 147-165.

Peacock, D. C. P., Xing, Z. 1994. Tectonic Processes of the Eastern Mediterranean and Analogous Region Field examples and numerical modelling of oversteps and bends along normal faults in cross-section. Tectonophysics 234, 147-167.

Perrin, C., Manighetti, I., Gaudemer, Y. 2015. Off-fault tip splay networks: A genetic and generic property of faults indicative of their long-term propagation. Comptes Rendus Geoscience 348, 52-60.

Putz-Perrier, M. W., Sanderson, D. J. 2008a. The distribution of faults and fractures and their importance in accommodating extensional strain at Kimmeridge Bay, Dorset, UK. Geological Society, London, Special Publications 299, 97-111.

Putz-Perrier, M. W., Sanderson, D. J. 2008b. Spatial distribution of brittle strain in layered sequences. Journal of Structural Geology 30, 50-64.

Putz-Perrier, M. W., Sanderson, D. J. 2010. Distribution of faults and extensional strain in fractured carbonates of the North Malta Graben. AAPG Bulletin 94, 435-456.

Rarity, F., Van Lanen, X., Hodgetts, D., Gawthorpe, R., Wilson, P., Fabuel-Perez, I., Redfern, J. 2014. LiDAR-based digital outcrops for sedimentological analysis: workflows and techniques. Geological Society, London, Special Publications 387, 153-183.

Roberts, G. P., Houghton, S. L., Underwood, C., Papanikolaou, I., Cowie, P. A., van Calsteren, P., Wigley, T., Cooper, F. J., McArthur, J. M. 2009. Localization of Quaternary slip rates in an active rift in 105 years: An example from central Greece constrained by 234U-230Th coral dates from uplifted paleoshorelines. Journal of Geophysical Research: Solid Earth 114, 406.

Roberts, S., Jackson, J. 1991. Active normal faulting in central Greece: an overview. Geological Society, London, Special Publications 56, 125-142.

Rohais, S., Eschard, R., Ford, M., Guillocheau, F., Moretti, I. 2007. Stratigraphic architecture of the Plio-Pleistocene infill of the Corinth Rift: Implications for its structural evolution. Tectonophysics 440, 5-28.

Rotevatn, A., Bastesen, E. 2014. Fault linkage and damage zone architecture in tight carbonate rocks in the Suez Rift (Egypt): implications for permeability structure along segmented normal faults. Geological Society, London, Special Publications 374, 79-95.

Rotevatn, A., Buckley, S. J., Howell, J. A., Fossen, H. 2009. Overlapping faults and their effect on fluid flow in different reservoir types: A LIDAR-based outcrop modeling and flow simulation study. AAPG Bulletin 93, 407-427.

Scholz, C. H., Dawers, N. H., Yu, J. Z., Anders, M. H., Cowie, P. A. 1993. Fault growth and fault scaling laws: Preliminary results. Journal of Geophysical Research: Solid Earth 98, 21951-21961.

Siddall, M., Chappell, J., Potter, E.-K. 2007. 7. Eustatic sea level during past interglacials. Developments in Quaternary Sciences 7, 75-92.

Skourtsos, E., Kranis, H. 2009. Structure and evolution of the western Corinth Rift, through new field data from the Northern Peloponnesus. Geological Society, London, Special Publications 321, 119-138.

Taylor, B., Weiss, J. R., Goodliffe, A. M., Sachpazi, M., Laigle, M., Hirn, A. 2011. The structures, stratigraphy and evolution of the Gulf of Corinth rift, Greece. Geophysical Journal International 185, 1189-1219.

Taymaz, T., Jackson, J., McKenzie, D. 1991. Active tectonics of the north and central Aegean Sea. Geophysical Journal International 106, 433-490.

Thorsen, C. E. 1963. Age of growth faulting in southeast Louisiana. Gulf Coast Association of Geological Societies 13, 103-110.

Trudgill, B., Cartwright, J. 1994. Relay-ramp forms and normal-fault linkages, Canyonlands National Park, Utah. Geological Society of America Bulletin 106, 1143-1157.

Turner, J. A., Leeder, M. R., Andrews, J. E., Rowe, P. J., Van Calsteren, P., Thomas, L. 2010. Testing rival tectonic uplift models for the Lechaion Gulf in the Gulf of Corinth rift. Journal of the Geological Society 167, 1237-1250.

Tvedt, A. B. M., Rotevatn, A., Jackson, C. A. L., Fossen, H., Gawthorpe, R. L. 2013. Growth of normal faults in multilayer sequences: A 3D seismic case study from the Egersund Basin, Norwegian North Sea. Journal of Structural Geology 55, 1-20.

Walsh, J. J., Bailey, W. R., Childs, C., Nicol, A., Bonson, C. G. 2003. Formation of segmented normal faults: a 3-D perspective. Journal of Structural Geology 25, 1251-1262.

Walsh, J. J., Nicol, A., Childs, C. 2002. An alternative model for the growth of faults. Journal of Structural Geology 24, 1669-1675.

Walsh, J. J., Watterson, J. 1987. Distributions of cumulative displacement and seismic slip on a single normal fault surface. Journal of Structural Geology 9, 1039-1046.

Walsh, J. J., Watterson, J. 1988. Analysis of the relationship between displacements and dimensions of faults. Journal of Structural Geology 10, 239-247.

Walsh, J. J., Watterson, J. 1991. Geometric and kinematic coherence and scale effects in normal fault systems. Geological Society, London, Special Publications 56, 193-203.

Walsh, J. J., Watterson, J., Bailey, W. R., Childs, C. 1999. Fault relays, bends and branch-lines. Journal of Structural Geology 21, 1019-1026.

Watterson, J. 1986. Fault dimensions, displacements and growth. pure and applied geophysics 124, 365-373.

Willemse, E. J. M., Pollard, D. D. 1998. On the orientation and patterns of wing cracks and solution surfaces at the tips of a sliding flaw or fault. Journal of Geophysical Research: Solid Earth 103, 2427-2438.

Wilson, P., Hodgetts, D., Rarity, F., Gawthorpe, R. L., Sharp, I. R. 2009. Structural geology and 4D evolution of a half-graben: New digital outcrop modelling techniques applied to the Nukhul half-graben, Suez rift, Egypt. Journal of Structural Geology 31, 328-345.

Zygouri, V., Verroios, S., Kokkalas, S., Xypolias, P., Koukouvelas, I. K. 2008. Scaling properties within the Gulf of Corinth, Greece; comparison between offshore and onshore active faults. Tectonophysics 453, 193-210.

Webpage

ΑΝΩΝΥΜΟΣ ΕΤΑΙΡΕΙΑ ΔΙΩΡΥΓΟΣ ΚΟΡΙΝΘΟΥ (Α. Ε. ΔΙ. Κ). 2009. The characteristics of the Canal. Available from: http://www.aedik.gr/frontend/index.php [Accessed: 20.01.2016].

Appendix I

Photo panel interpretations – NW of central horst
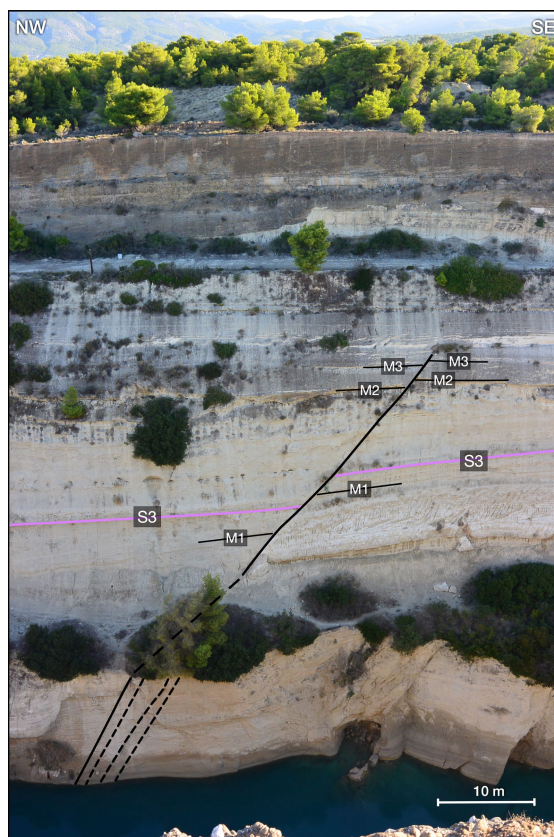
Figure AI.1 – Photo panel interpretation of fault FN1.1 exposed on the eastern canal wall. Note planar fault geometry and footwall deformation.
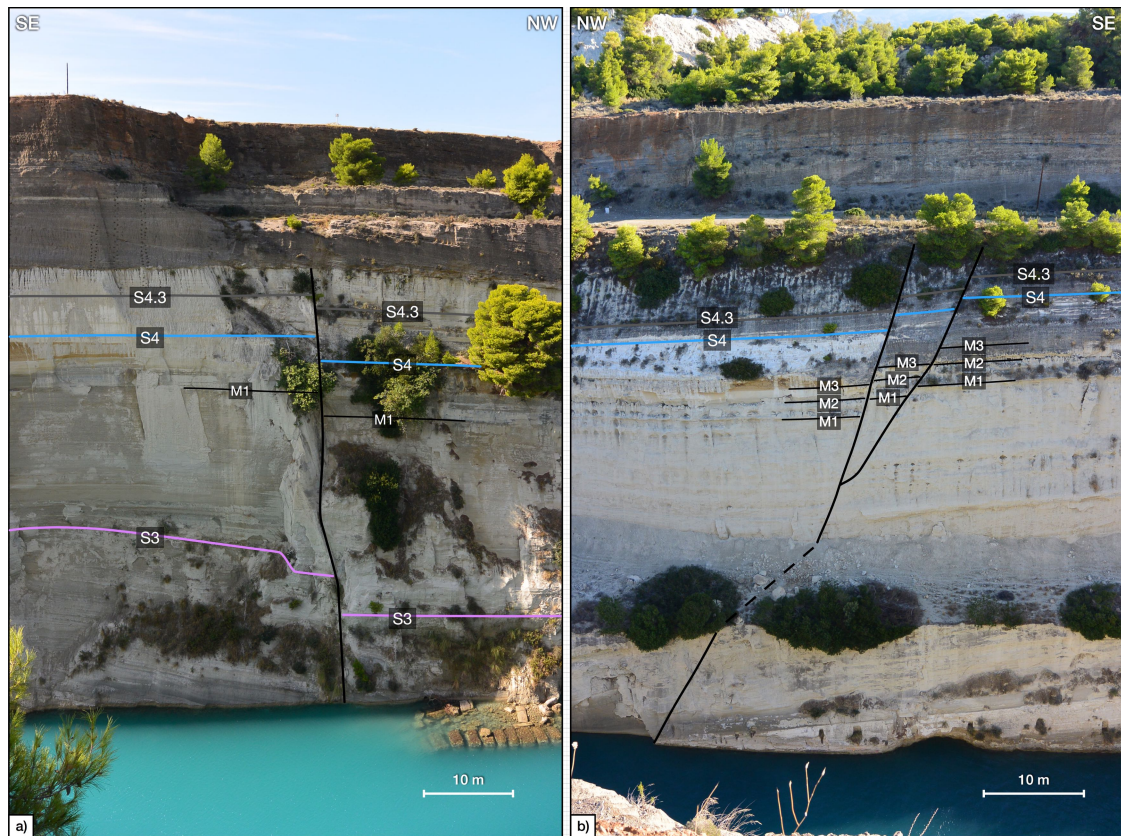
Figure AI.2 – Photo panel interpretations of fault FN1.2 on both the (a) western and (b) eastern canal walls indicating fault geometry and footwall deformation.
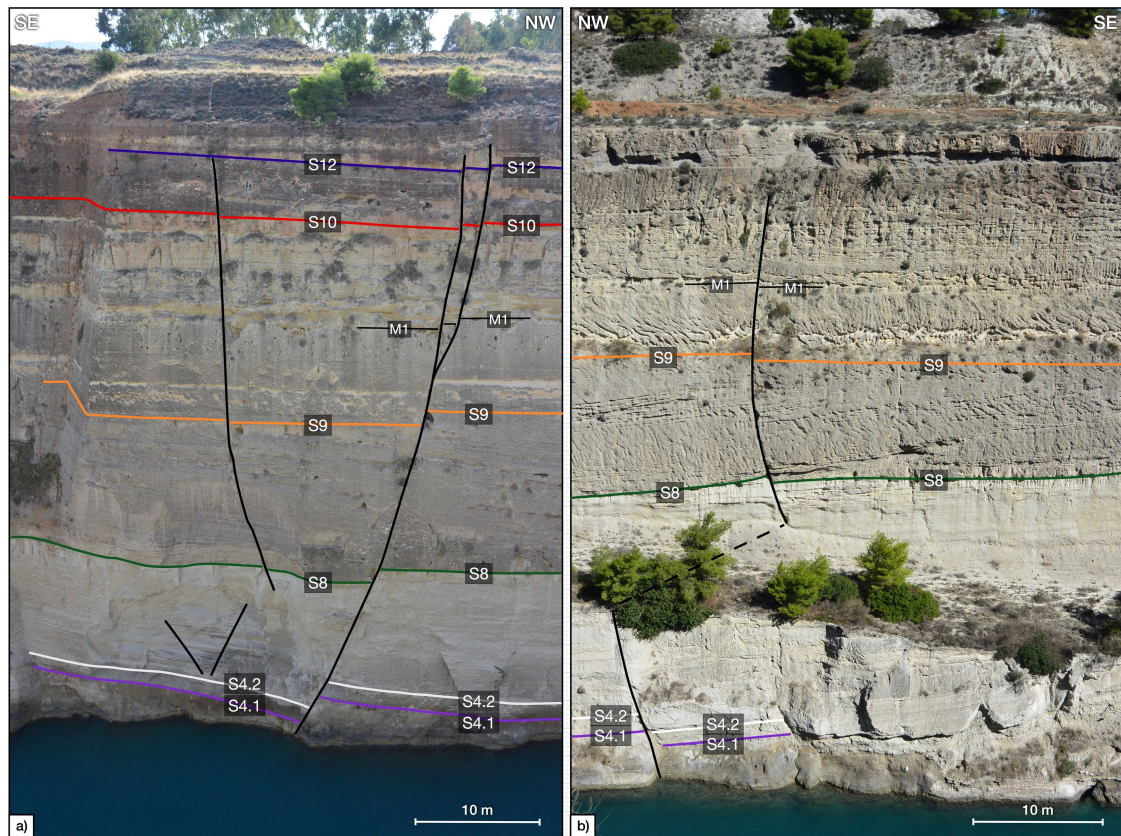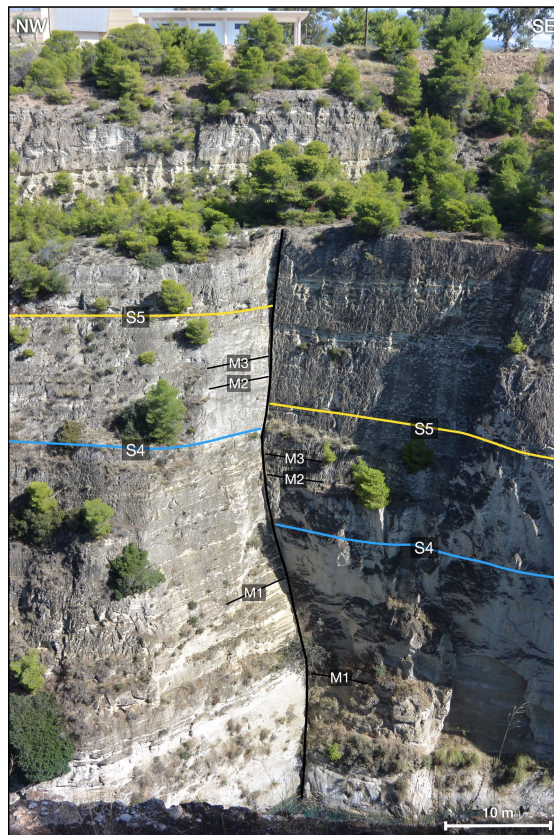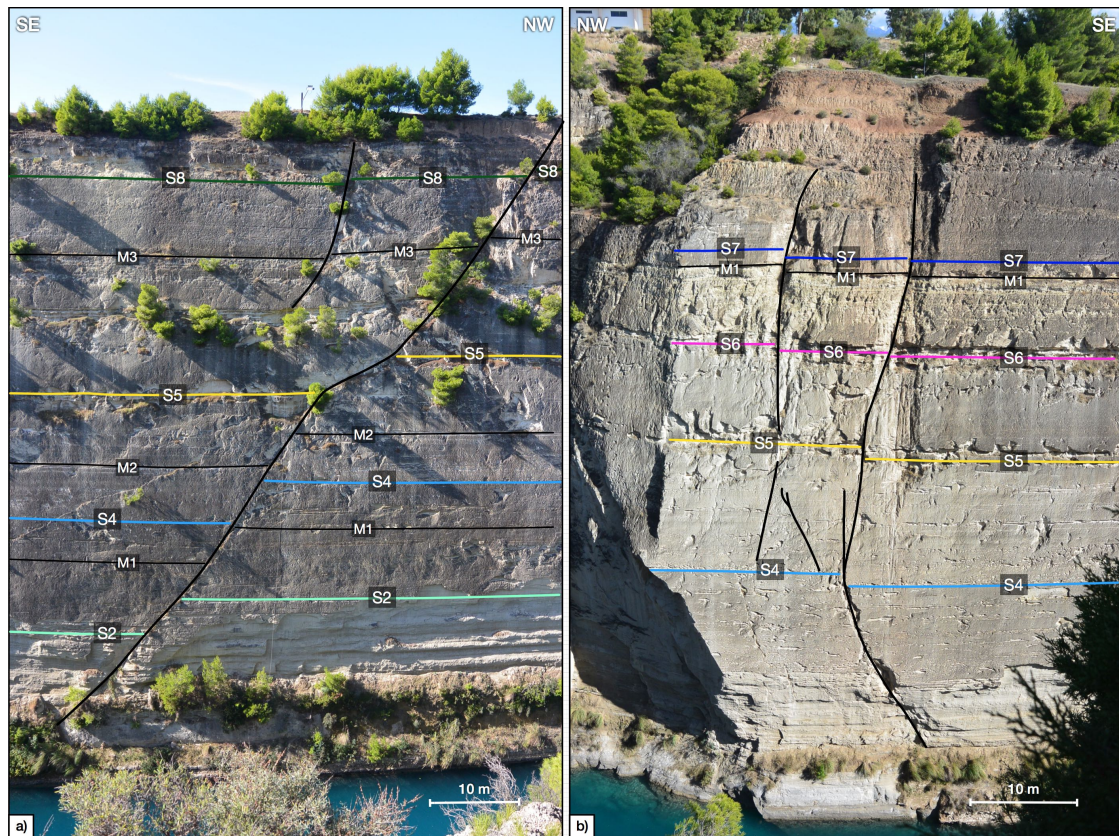

Figure AI.3 – Photo panel interpretations of fault FN2 on both the (a) western and (b) eastern canal walls indicating fault geometry, hanging wall and footwall deformation.
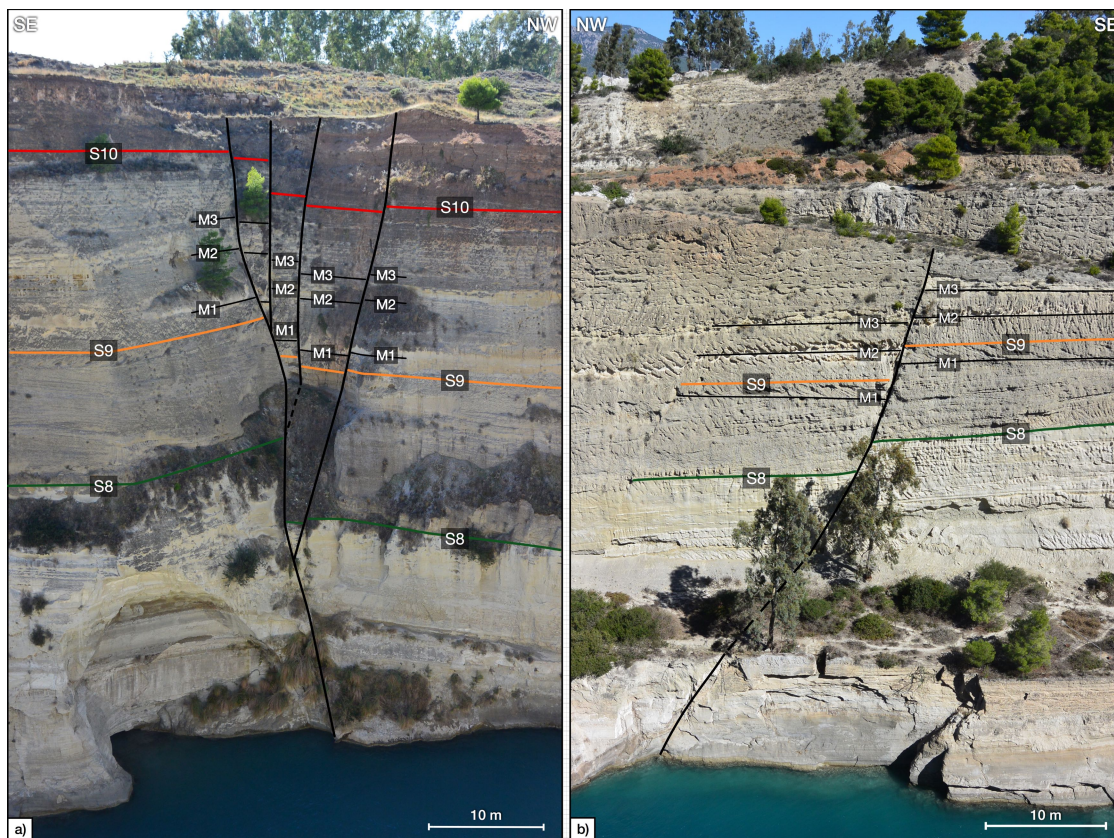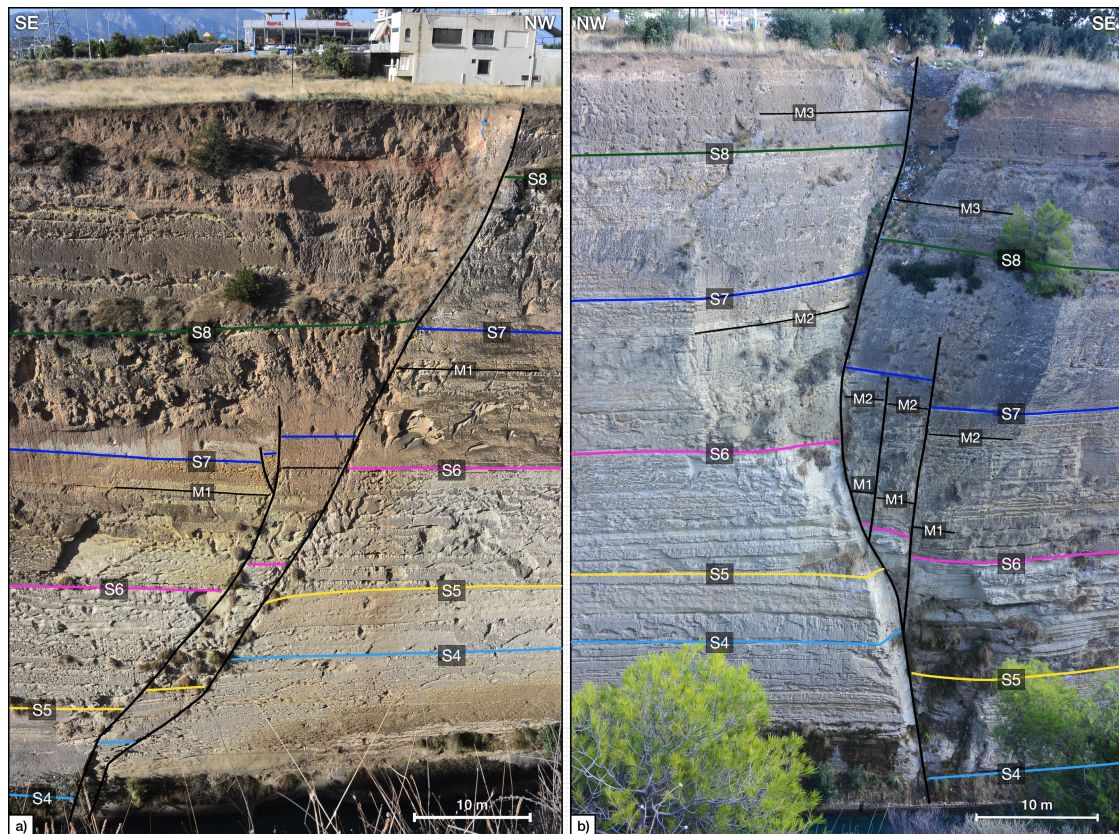
Figure AI.4 – Photo panel interpretations of fault FN5 on both the (a) western and (b) eastern canal walls indicating fault geometry and hanging wall deformation.
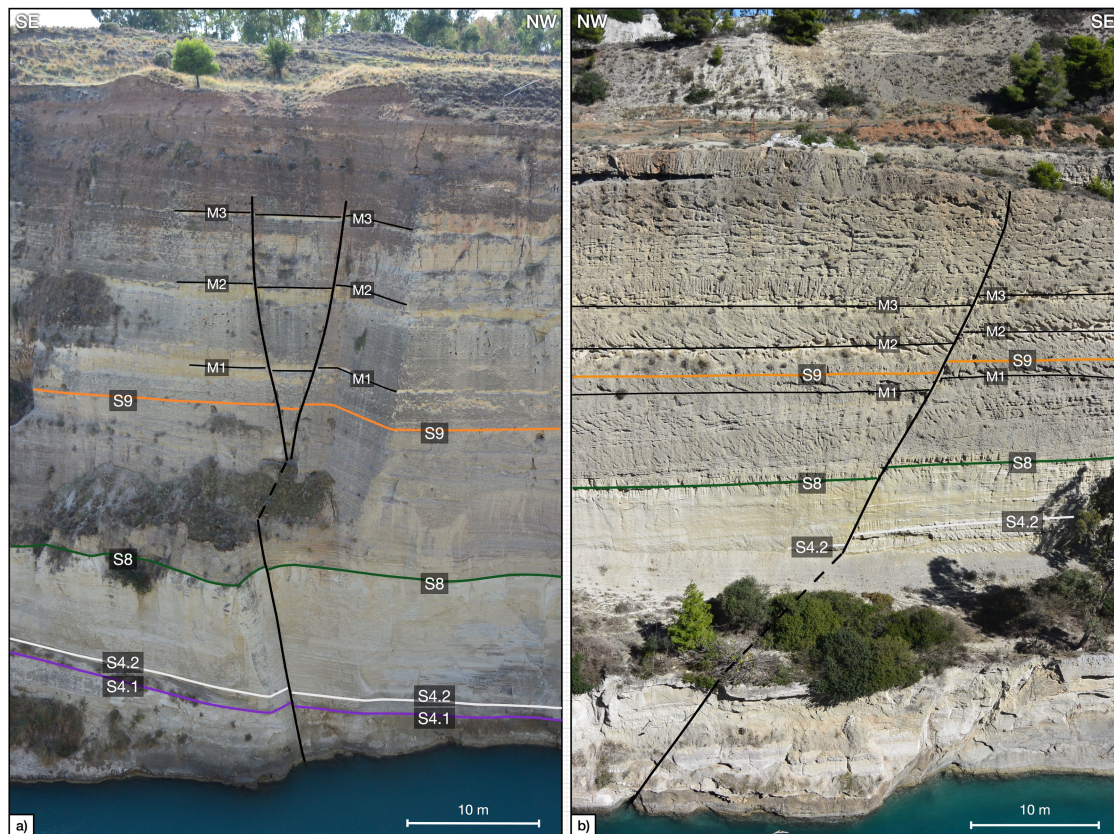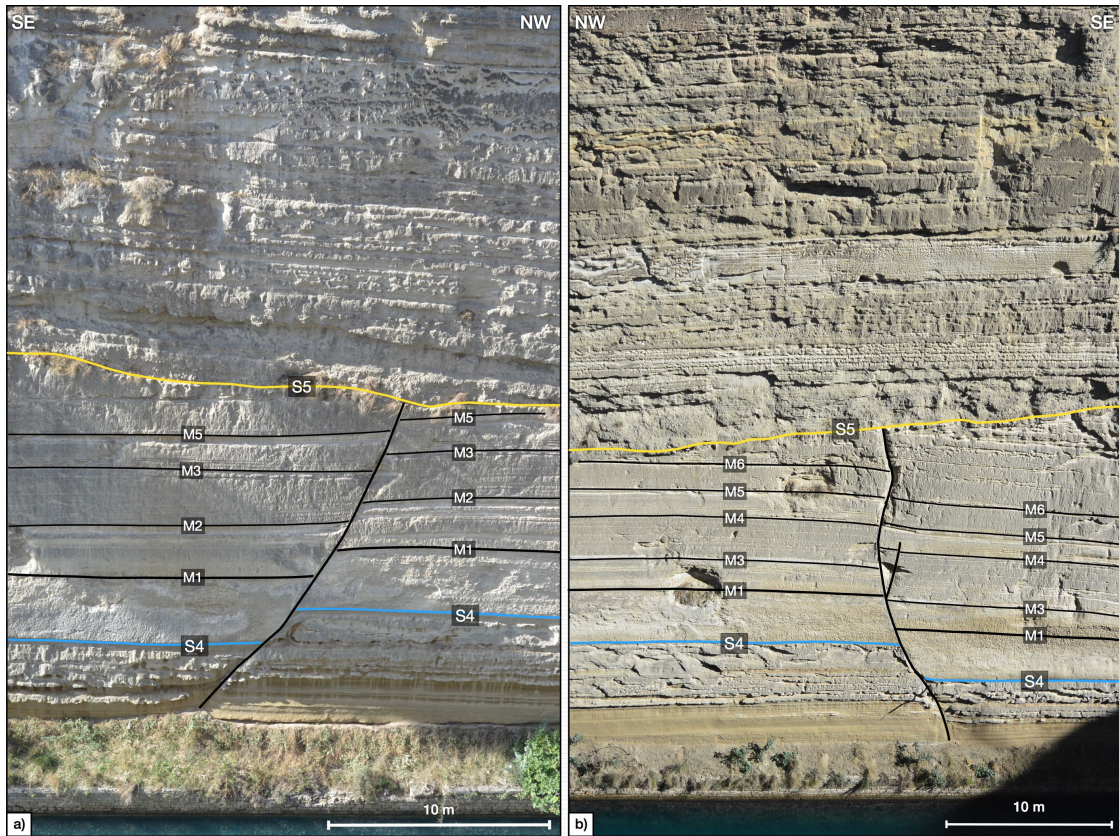

Figure AI.5 – Photo panel interpretations of fault FN5.1 on both the (a) western and (b) eastern canal walls indicating fault geometry and hanging wall deformation.
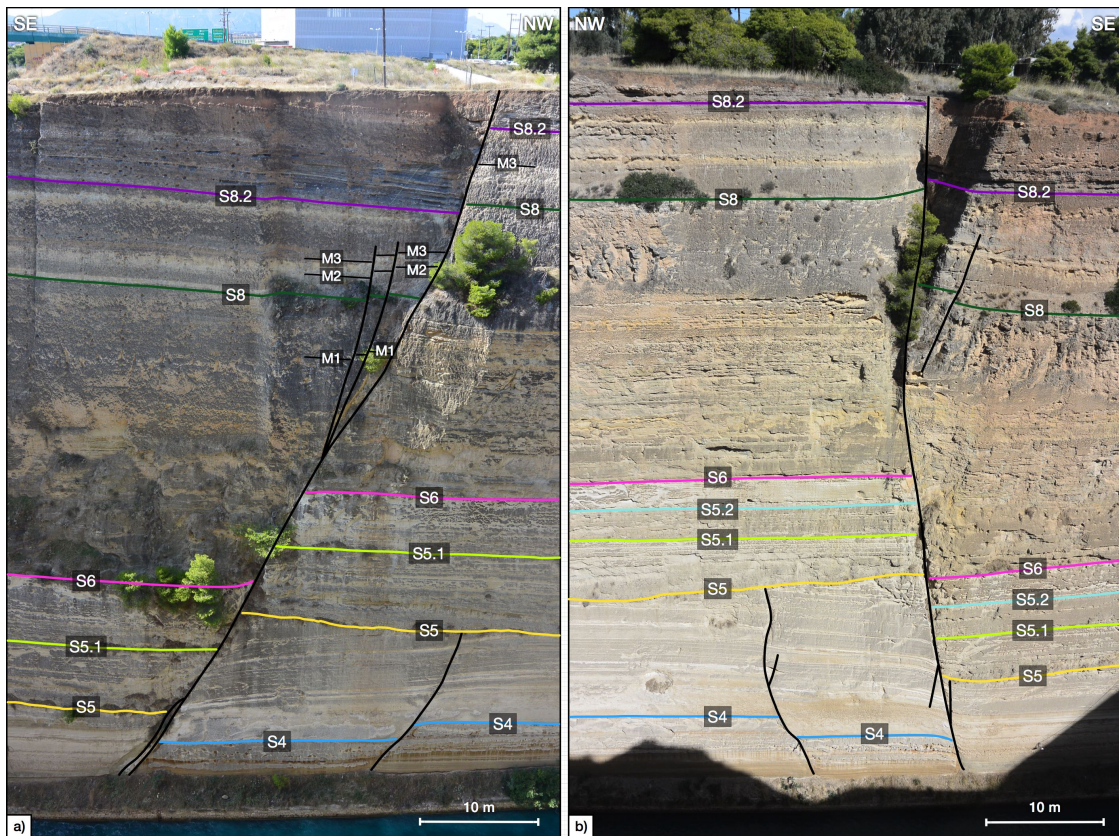
Figure AI.6 – Photo panel interpretations of fault FN6 on both the (a) western and (b) eastern canal walls indicating fault geometry, hanging wall and footwall deformation.

Photo panel interpretations – SE of central horst before the Isthmia Graben

Figure AI.7 – Photo panel interpretation of fault FS1.1 exposed on the eastern canal wall. Note planar fault geometry.

Figure AI.8 – Photo panel interpretations of fault FS2 on both the (a) western and (b) eastern canal walls indicating fault geometry, hanging wall and footwall deformation.
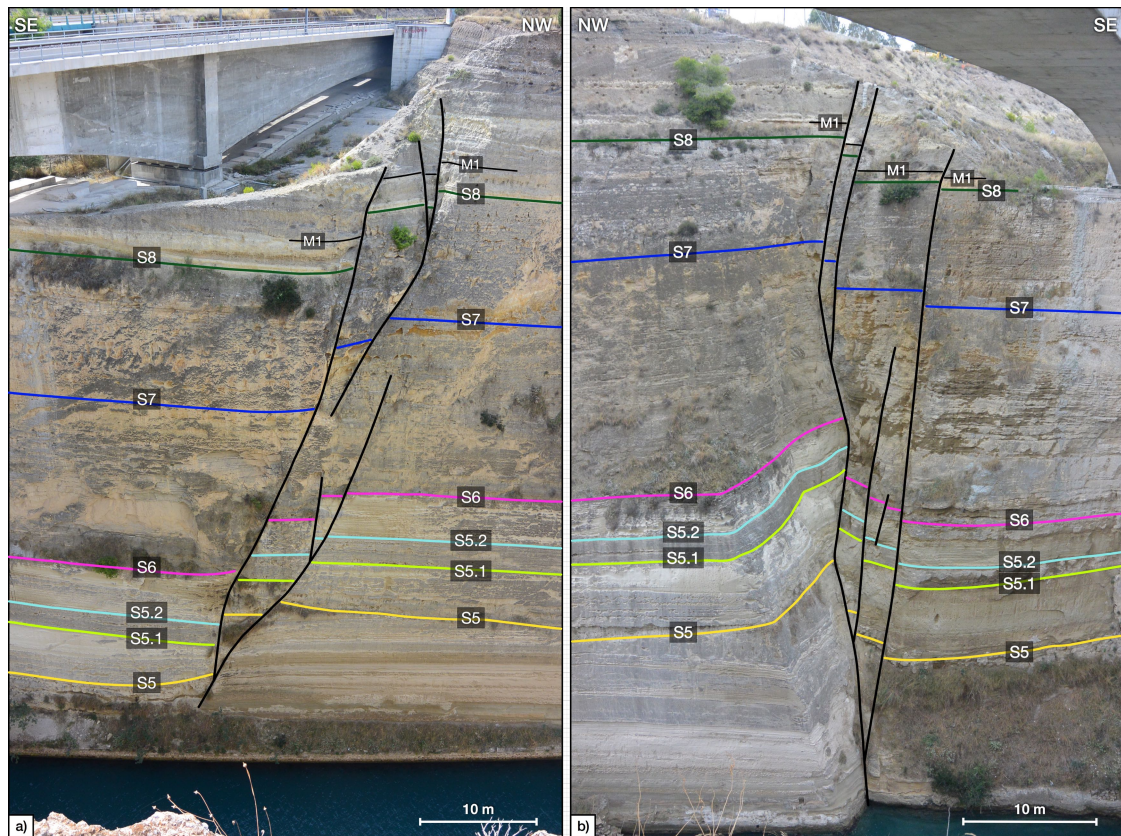

Figure AI.9 – Photo panel interpretations of fault FS4 on both the (a) western and (b) eastern canal walls indicating fault geometry and hanging wall deformation.

Figure AI.10 – Photo panel interpretations of fault FS4.1 on both the (a) western and (b) eastern canal walls indicating fault geometry and hanging wall deformation.

Figure AI.11 – Photo panel interpretations of fault FS5 on both the (a) western and (b) eastern canal walls indicating fault geometry, hanging wall and footwall deformation.

Figure AI.12 – Photo panel interpretations of fault FS6 on both the (a) western and (b) eastern canal walls indicating fault geometry, hanging wall and footwall deformation.

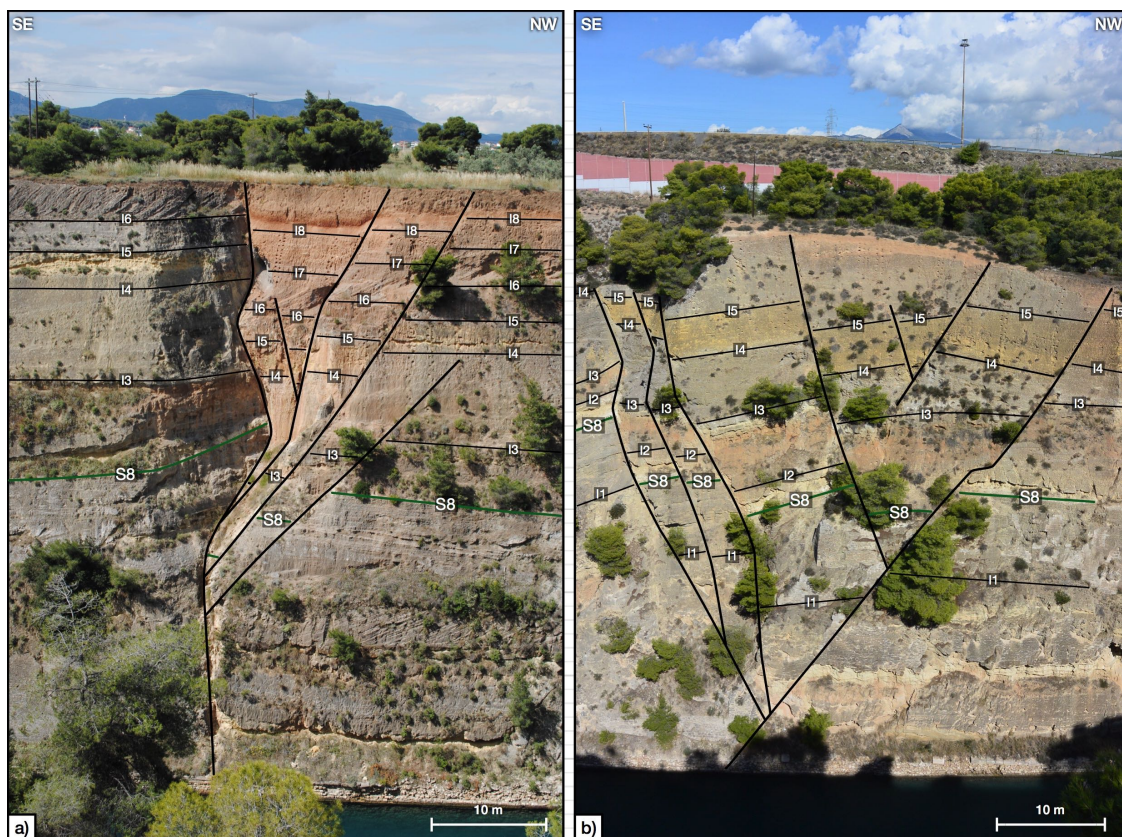Photo panel interpretations – Isthmia Graben

Figure AI.13 – Photo panel interpretations of fault FS10 on both the (a) western and (b) eastern canal walls indicating fault geometry and hanging wall deformation.

Appendix II

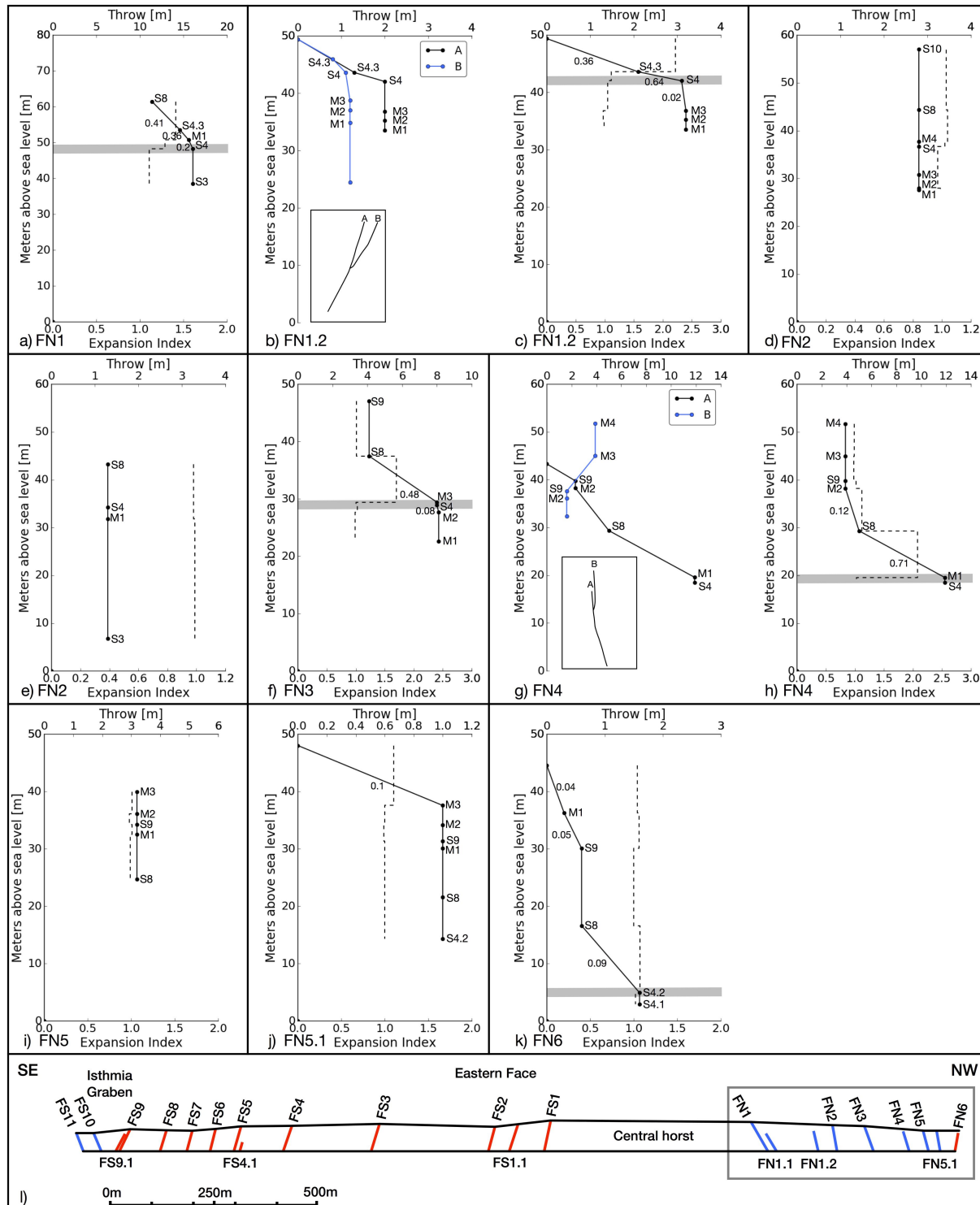## T-z plots and expansion indices – NW of central horst

Figure AII.1 – Throw-depth (T-z) plots with throw gradients and expansion indices of faults NW of the central horst. Expansion indices are marked by dashed lines. Gray line indicates where the faults were surface breaching. The legends and figure in b and g indicate the main fault (A) and its splay (B). (m) Cross-section of study area indicating the location of the faults (gray box).

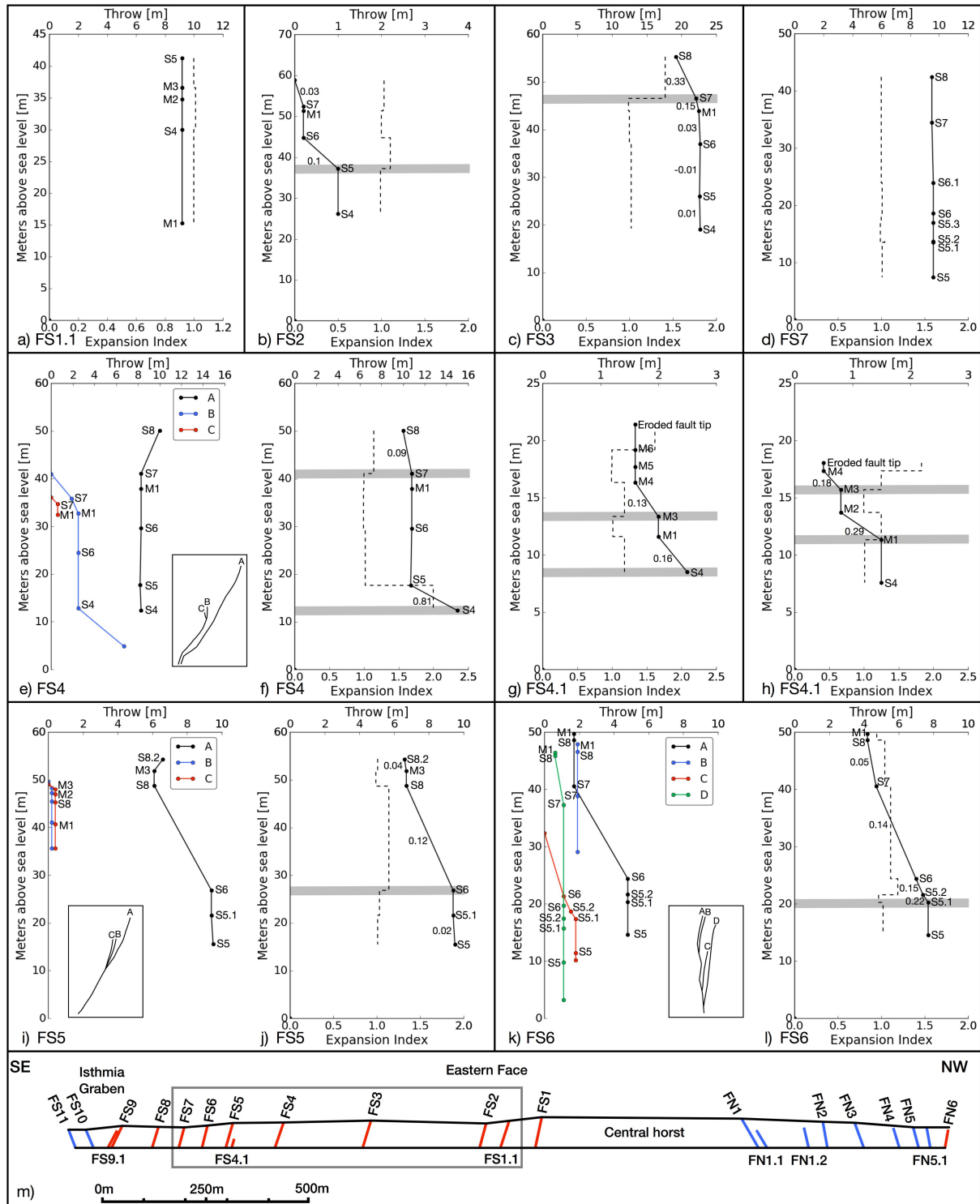# T-z plots and expansion indices – SE of central horst before the Isthmia Graben

Figure AII.2 – Throw-depth (T-z) plots with throw gradients and expansion indices of faults SE of the central horst before the Isthmia Graben. Expansion indices are marked by dashed lines. Gray line indicates where the faults were surface breaching. The legends and figures in e, i and k indicate the main fault (A) and splays or hanging wall fault (B, C and D). (m) Cross-section of study area indicating the location of the faults (gray box).
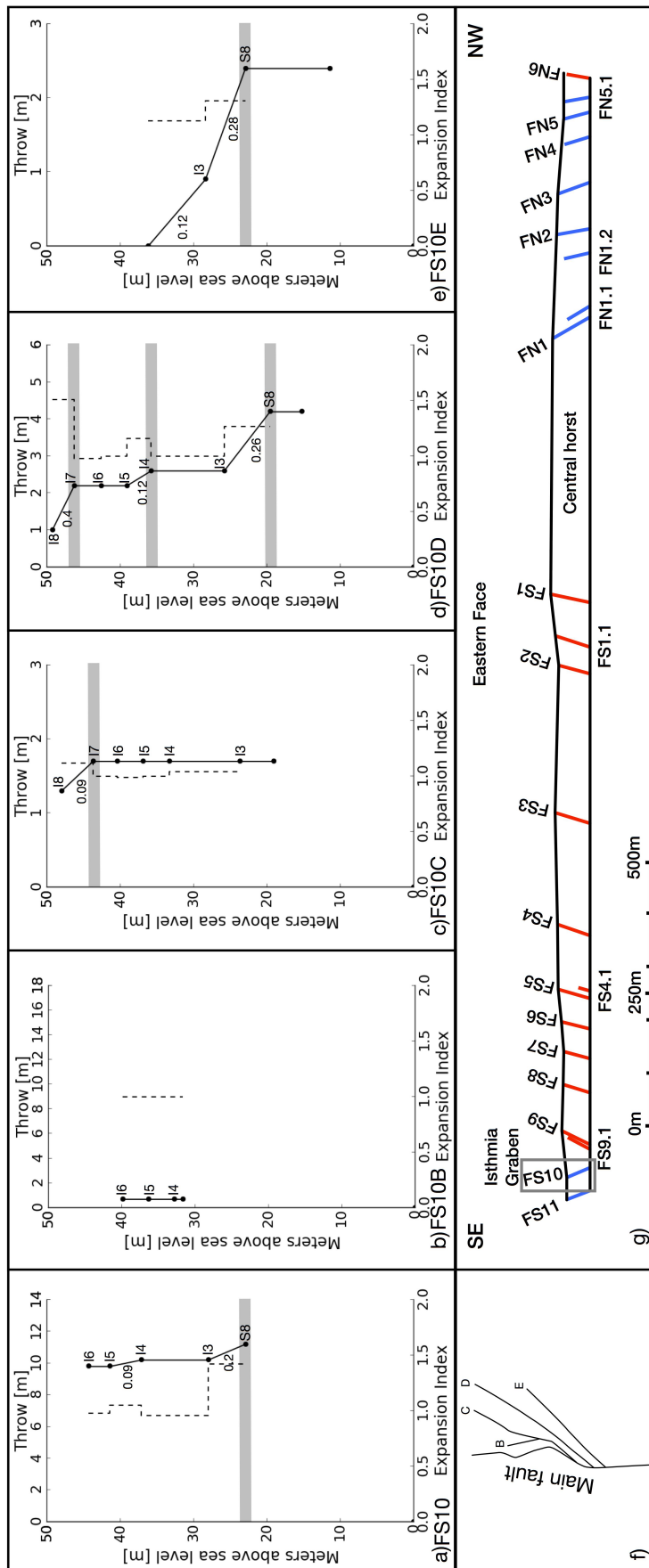
T-z plots and expansion indices – Isthmia Graben

Figure AII.3 – (a–e) Throw-depth (T-z) plots with throw gradients and expansion indices of fault FS10 and its hanging wall splays located within the Isthmia Graben. Expansion indices are marked by dashed lines. Gray line indicates where the main fault and the splays were surface breaching. (f) Fault geometry of fault FS10. (g) Cross-section of study area indicating the location of fault FS10 (gray box).